UCLouvain

epl

École polytechnique de Louvain

Towards a scanning thermal microscope for measurements below 20K

Author: **Valentin Fonck**
Supervisors: **Pascal Gehring, Benoît Hackens**
Readers: **Bernard Nysten, Sébastien Faniel**
Academic year 2021–2022
Master [120] in Physical Engineering

Abstract

Scanning thermal microscopy (SThM) allows the local temperature imaging at the nanometer scale with an excellent sensitivity. So far its applications were limited over 20K as no suited probe had been developed. The local thermometry of nanometer scale systems at very low temperatures thus remain a widely unknown research field. Indeed, thermal aspects of known quantum effects such as the quantum Hall effect remain to be investigated [1]. The cross-coupling of the thermal conductivity with other quantities, such as the magnetic field, could reveal new quantum phenomena and new ways to control nanosystems. The manipulation of these systems can also be directly performed using a hot tip. For instance, the manipulation of encapsulated van der Waals heterostructures is a major issue that could be overcome with cryogenic scanning thermal microscopy [2].

This work aims at the realisation of a SThM set-up for temperature measurement below 20K. To achieve this, an Akiyama probe with on its tip a resistive element suited for thermal measurements below 20K was designed. This probe was simulated using finite elements. Its resonance frequency, spring constant and different calibration parameters could be obtained. Major advances towards the microfabrication of such probes were realised. Among them, the fabrication of two stages sharp AFM tips with TMAH was demonstrated. The deposition of metals on their apex using a single partial spin-coating opens new paths to their batch production without EBL or photolithography. A vacuum compatible AFM set-up with a self-sensing amplitude-based feedback was successful implemented. These realisations pave the way to the implementation of a fully operational cryogenic SThM set-up.

Contents

Chapter 1

Introduction

Scanning thermal microscopy (SThM) is currently the only tool capable of probing the temperature and heat exchanges at the nanometer scale. As such, it has been employed both for fundamental research and applications, such as the identification of hotspots on MOS devices [3, 4]. For example, defects in graphene could be correlated with local variations of the thermal conductivity in [5]. The continuous downscaling of electronic devices together with the growing need of a fundamental understanding of nanoscale heat transport have made SThM a vital tool for solid state research.

So far, SThM systems have been limited over 20K due to the absence of working probes at lower temperatures. Local nanoscale heat exchanges below 20K thus remains a widely unexplored research field. Many quantum phenomena, such as the quantum Hall effect, require low temperatures to appear and their thermal counterparts remain to be investigated [1]. Macroscopic models used for thermal conductivity fail at cryogenic temperatures and nanometer scale. The quantisation of the thermal conductance is one of these examples. So far imaged in graphene, it could also appear in other materials at lower temperatures. [6] Another fundamental question is the violation of the Wiedemann-Franz law in quantum devices [7–10]. These violations were reported to happen below 20K and thus require a cryogenic SThM probe to image them.

This work aims at the development of a SThM set-up able to perform measurements below 20K. The main challenge of this research concerns the probe as it is at the core of the microscope and has never been realised. Two probe design bottlenecks for cryogenic SThM were identified: the laser feedback and the material of the temperature sensing element. To measure the sample-probe interaction, a self-sensing tuning fork was chosen combined with the Akiyama probe design which allows quasi-contact mode imaging with improved self-sensing performances, both essential for SThM at low temperature. [11] For the temperature sensing elements, new materials suitable at temperatures below 20K were considered: Zirconium nitride, amorphous carbon and platinum. To implement these new features, three main tasks were identified: simulation of an Akiyama SThM probe using finite element analysis, microfabrication of this probe and, finally, the fabrication of a

self-sensing AFM set-up. More precisely, the following different objectives were defined within these three tasks:

- Draw design guidelines and fix the probe's dimensions using simulations of the mechanical and thermal behaviours of an Akiyama SThM probe.
- Estimate the calibration parameters to be used to extract a temperature or heat flux from a nominal signal.
- Illustrate different practical aspects that can deter the performances of a SThM probe using simulation.
- Fabricate AFM tips using TMAH etching.
- Investigate the deposition methods and performances for cryogenic thermometry of these materials: zirconium nitride, amorphous carbon and platinum.
- Define cantilevers and pads for an Akiyama probe in silicon using the Bosch process.
- Define electrical contacts on an AFM tip using photolithography.
- Build an AFM set-up using a self-sensing tuning fork for its feedback.

In the following chapters, a state of the art of the SThM technique is provided. Then, the finite element simulations are detailed. The results of the different microfabrication steps are reported. Finally, the implementation of the tabletop AFM set-up is summarised and some preliminary scan images are presented. All together, the results presented in this work provide the building blocks of a low temperature SThM and clear the way to realising the first mK SThM experiment at UCLouvain.

Chapter 2

State of the art

2.1 Atomic force microscopy (AFM)

Following the rapid development of the scanning tunnel microscopy (STM), relying on the tunnel current between a surface and a sharp tip, the first realisation of an atomic force microscope was presented by G. Binnig *et al.* in [12]. In this technique, a sharp tip, with a radius of around tens of nm, is brought into contact, or extreme proximity, with a surface. The interaction with the surface will modify the behaviour of the tip and this change is monitored. A feedback mechanism is used to adapt the vertical position of the tip through the extension of a piezoelectric transducer.

2.1.1 AFM modes

As illustrated in Figure 2.1.1, there exists three distinct contact regimes between an AFM tip and a surface. The influence of the interaction on the resonant frequency the cantilever with respect to the vertical position of the equilibrium is schematically illustrated. Similar curves can be traced with respect to the phase or the amplitude of the oscillation which allow these three types of feedback to be used.

Contact modes A wide range of modes can be used to image surfaces. The most simple are the constant force and constant height modes. They were the first modes historically introduced. They are illustrated in Figure 2.1.2. In the constant height mode, the deflection is simply recorded and no feedback loop is implemented. This technique has the advantage to allow the fast scanning of a surface but must be reserved for flat surfaces as high aspect ratio features will likely break the tip. The constant force mode, first introduced in [12], uses a feedback loop on the deflection to maintain a constant force applied on the surface. These modes are said to be contact modes. Other contact modes exist such as the lateral forces mode. They are generally non-resonant modes, thus the static deflection of the cantilever is monitored, although, as it will be illustrated in subsection 2.2.4, it is theoretically also possible to use resonant modes in contact with the sample.

Non-contact modes In non-contact modes, a tip is brought extremely close, in the order of tens of Angstroms, to a surface. The cantilever is vibrating near its resonance frequency and any change in its amplitude of vibration can be related to an interaction with the surface. They are thus resonant modes. Using different types of probes and cantilevers, different long distance interactions can be imaged such as the magnetic or Van der Waals forces. [13–15]

Intermittent contact mode (Tapping mode) In intermittent contact, or tapping, mode the tip only touches periodically the surface. Using different types of feedbacks, some will be detailed at subsection 2.1.2, a setpoint can be chosen based on the amplitude, frequency or phase of the vibration. Via its phase detection, this mode allows to map multiphasic materials based on their stiffness. A plane multiphasic material will yield no contrast in the topographic image while its phase image will highlight these different regions.

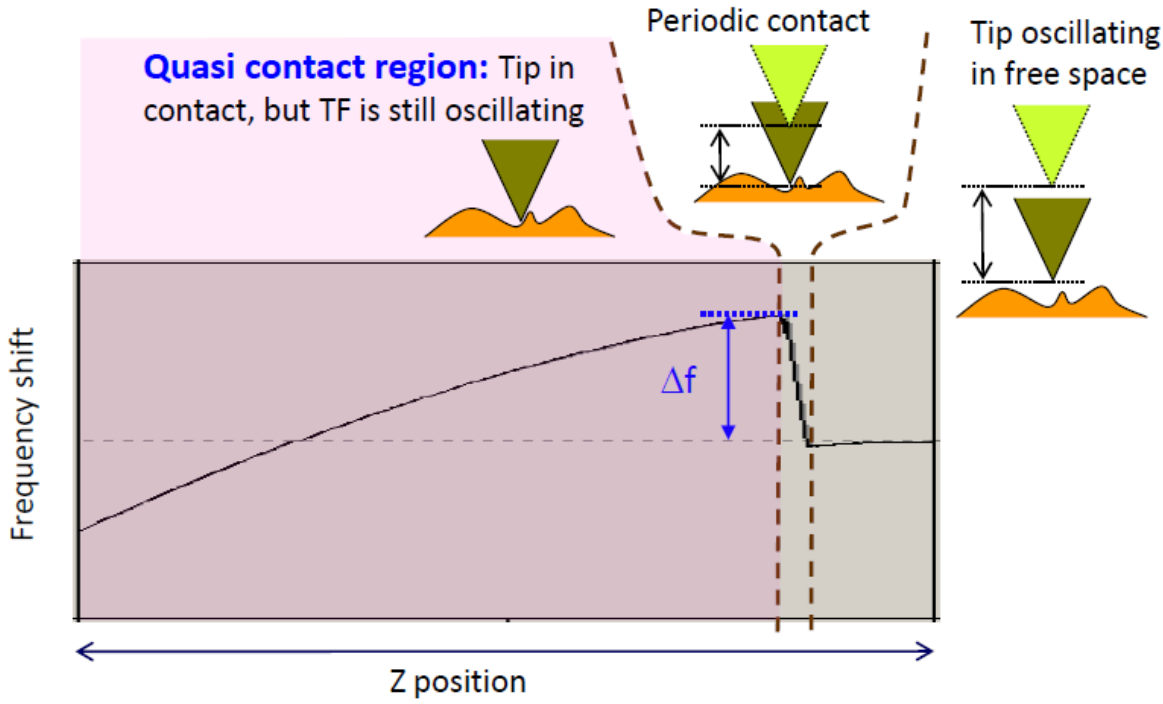

Figure 2.1.1: Illustration of the different contact regimes for frequency-modulated AFM. Schematic representations of the positions of the tip with respect to the surfaces are presented above. [16]

Harmonic oscillator model for resonant modes Resonant modes rely on the vibration of the cantilever. The tip oscillates near its resonance frequency. The interaction with the surface can be seen as a damping and treated as such in the classical oscillator equation.

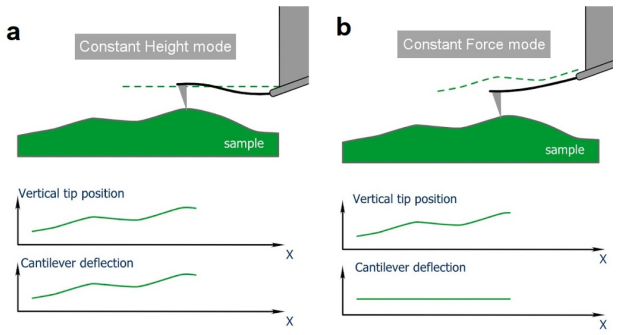

Figure 2.1.2: Illustration of the working principles of the **a** constant height mode and **b** constant force modes. The vertical position and cantilever deflection (which measures the force acting on the tip) with respect to the position on the sample are also provided. [17]

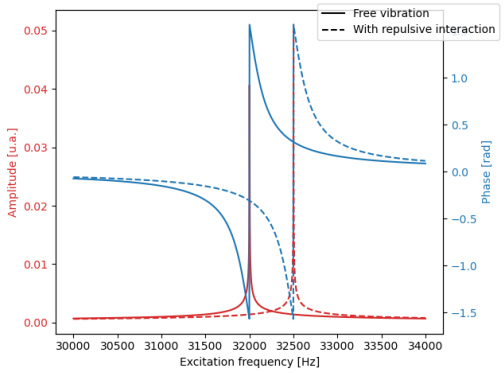

Figure 2.1.3: Amplitude and phase for a free and under repulsive interaction oscillator, obtained from the analytical expressions Equation 2.1.2 and 2.1.3.

$$\ddot{z} + \gamma\dot{z} + \omega_0^2 z \;=\; \frac{f}{m} cos(\omega t) \tag{2.1.1}$$

where z is the vertical position of the tip, γ is a complex number representing the damping of the system, thus the interaction with the surface, f is the amplitude of the driving force, ω_0 is the resonance frequency of the system and m is the mass of the oscillator, thus the cantilevers and tip here. ω is the frequency of the driving force, it is thus not necessarily equal to the resonance frequency. The driving force, in practice, the vibration of the cantilever and its frequency is fixed by the excitation signal.

Solving this equation leads to expressions for the amplitude and phase shift of the system, presented without derivation at Equations 2.1.2 and 2.1.3. These expressions can be found in [18] and one example of full derivation can be found in [19].

$$A(\omega) \;=\; \frac{f/m}{|(\omega_0^2 - \omega^2)^2 + \gamma^2\omega^2|^{1/2}} \tag{2.1.2}$$

$$\phi(\omega) \;=\; \arctan\left(\frac{\gamma\omega}{\omega^2 - \omega_0^2}\right) \tag{2.1.3}$$

The modification of the amplitude $A(\omega)$ and phase $\phi(\omega)$ of this vibration can be related to the topography and mechanical properties of the material. The feedback loop will adjust the sample vertical position to stay at its setpoint, corresponding to a constant amplitude, phase or frequency. The output of the feedback loop is stored and after image treatment, represents the characteristics of the surface. The graphs of the amplitude and phase of a $32kHz$ free and under repulsive interaction oscillator are presented in Figure 2.1.3.

In comparison with non-resonant, or static modes, resonant modes limit drastically the damaging lateral forces associated with contact modes. This allows to work with sensitive materials. In addition, the use of a resonant mode is required for a self-sensing scheme as will be explained in section 2.3.

The impact of the quality factor Equation 2.1.2 can be used to extract the value of its full width at half maximum. The maximum amplitude frequency ω_m[1] can be computed. The associated maximum amplitude of the distribution is thus obtained as well. The assumption of an underdamped system is made, thus $\omega_0^2 >> \gamma^2$.

$$\omega_m = \sqrt{\omega_0^2 - \frac{\gamma^2}{2}}$$

$$A(\omega_m) = \frac{f/m}{\gamma\sqrt{\omega_0^2 - \gamma^2/4}} \approx \frac{f/m}{\gamma\omega_0}$$

Using the same approximation and imposing that the amplitude is half of this value, one can find the FWHM of the amplitude spectrum.

$$\omega_F = \omega_0\sqrt{1 \pm \frac{\gamma}{\omega_0}} \overset{\text{Taylor}}{\approx} \omega_0 \pm \frac{\gamma}{2} \implies \text{FWHM} \approx \gamma$$

Thus the quality factor, defined as $\omega_0/FWHM$, can be directly related to the width of the amplitude distribution presented Figure 2.1.3. Thus, in an amplitude-modulated set-up, the same interaction will induce a greater change in amplitude with a system with a greater quality factor. This greater change in amplitude allows to reach a higher sensitivity with the same feedback parameters.

2.1.2 Feedback types

There exists different ways to measure the tip-sample interaction. Here, three popular methods are presented.

Laser reflection feedback A laser is focused on a reflective surface, a metal generally, placed on the cantilever. The laser beam is placed at a constant incident angle with respect to the surface's normal. The deflection of the cantilever will modify the position of the reflected beam on a 4-quadrant photodiode which allows to monitor the vertical position and lateral bending of the cantilever. It was the first historically introduced feedback method[2] and it is still widely used in commercial set-ups nowadays.

[1] ω_m is the frequency at the centre of the distribution and is different from the resonance frequency of the system ω_0.

[2] G. Binnig *et al.* used a completely different set-up with a second STM tip used to measure the deflection of the cantilever [12] but then the laser feedback became rapidly very popular until nowadays.

Laser interferometry feedback In this mode, a laser is also focused on a reflective surface over the tip's position. This time, oppositely to the precedent feedback presented, the laser, generally via an optical fiber, is brought close and vertically to the reflective surface. A Fabry-Pérot cavity is thus formed between the end of the optical fiber and the surface of the cantilever. A variation of its length will thus impact the intensity of the reflected light depending on the resonance of the laser's frequency with this new length [20]. The intensity of the reflected light can be isolated from the incident one with a $\lambda/4$ plate and a polarised beamsplitter for example [21]. A schematic illustration of this kind of set-up can be found in Figure A.0.1. The optical fiber is not present on this illustration, it would be placed between the $\lambda/4$ plate and the tip.

Self-sensing tuning fork A third option is to monitor the interaction with the surface through the behaviour of the tuning fork. A tuning fork is a device made of a U-shaped piezoelectric material, generally quartz. A difference of potential applied between them will translate into an electric field that will in turn generate a strain in the crystal. When this signal is oscillating, so will the movement of the tuning fork. These modes can be excited by choosing the corresponding frequency for the excitation signal. These are called the resonance frequencies of a tuning fork.

The electrodes in the tuning fork act electrically as a capacitance. The value of this capacitance can be linked to the geometrical dimensions of the tuning fork and thus to its strain. Therefore, monitoring the capacitance of the tuning fork allows to control the vibration of its free ends and thus its interaction with the surface via the AFM tip that is fixated on it. This scheme of measurement is called self-sensing as the excitation signal is also used to extract the feedback signal. The feedback can be based on the amplitude, frequency or phase of the vibration. The feedback response extracted is then used to adjust the vertical position using a piezoelectric transducer.

This feedback mode offers non-negligible advantages. First, it is compact as it does not imply any optical element. It does not imply any parasite heating from the laser which is particularly interesting for cryogenic experiments where the cooling power is limited. As with interferometry feedback, it does not allow directly the visualisation of lateral forces. This feedback mode does not allow static measurement as it relies on capacitive sensing [19].

Another considerable advantage of this feedback is that its vibration is dominated by the tuning fork[3]. this allows to take advantage of teh very high quality factor of tuning fork (over 70 000 in a vacuum shell for commercial probes [23]) compared to the ones of AFM probes (around 35 000 in ultra high vacuum [24]). As already stressed in subsection 2.1.1, this is desirable for the feedback loop.

[3]The resonance frequency is fixed by the tuning fork and not the probe. [22]

2.2 Scanning thermal microscopy (SThM)

Scanning thermal microscopy aims at measuring the thermal properties of a sample along with its topography. This is achieved by the implementation of a thermometer on the AFM tip. Using one of the usual AFM feedbacks, the tip scans the surface and the thermal signal is recorded simultaneously with the topography. This thermal imaging strategy presents important advantages compared to other methods. Compared to far-field optical methods, such as Raman thermal imaging used in [25–27], it is not limited by the diffraction limit and thus allows a better resolution [28] although it implies a more complex calibration and data interpretation due to the complexity of the direct thermal contact as will be detailed in chapter 3.

The near-field optical scanning thermometry (NFOT), a derivative of the near-field optical scanning microscopy (NSOM or SNOM), relies on the analysis of the evanescent fields of a surface. By interpreting the evolution of temperature dependent characteristics of the sample, its temperature is indirectly extracted. This technique is not limited by the diffraction limit and a lateral resolution of 50 nm was reported in [29]. Although presenting a lot of advantages, this approach requires a pre-existent knowledge of the characteristics of the sample to image. This proves to be a problem for exotic materials at cryogenic temperatures. This technique was used at 1.8K in [30].

SThM requires little or no sample preparation which is an important practical feature compared to the direct lithographic implementation of heaters and thermometers, as presented in for example in [31, 32]. Lateral resolutions for the topography below 10nm were obtained with this technique [33]. The temperature resolution is defined as the noise equivalent temperature difference that a system features. Ultra-high vacuum SThM set-ups can reach 15mK as reported in [34].

2.2.1 Imaging modes

Passive mode In the passive imaging mode, the sample is generally an active device that can be heated. The probe temperature is monitored as the tip scans the sample. The temperature measurement is done by a sensing element, generally a resistive device or a thermocouple in which a negligible current is fed, to avoid parasitic Joule heating.

Active mode In the active mode, the sensor also acts as a heater. The resistance of the heating element is monitored and depends on the temperature. The generated heat will flow partly into the sample. Assuming a proper calibration and modelling, the thermal conductivity of the local region in contact with the probe can thus be estimated. Different active modes exist depending, among others, on the parameter chosen for the set point. The heat flux or the temperature of the heater can be kept constant for example [35].

The active SThM mode will be the main focus in the rest of this work since it also allows local manipulations of nanosystems, for example the manipulation of magnetic nanostructures which are areas of research of the host laboratory [36].

2.2.2 Types of probes

Wollaston wire The Wollaston wire probe was the first SThM probe. It was introduced by Pylkki *et al.* in 1994 in [37, 38]. SEM images of this kind of probes is presented in Figure A.0.2. The temperature sensing element is a $5\mu m$ diameter Pt_{90}/Rd_{10} cable, protected by a $75\mu m$ diameter silver shell that is locally etched to expose its core where the sensing takes place. The cantilever is here the whole structure. An optical feedback was used thanks to a mirror placed on the supporting structure, as highlighted in Figure A.0.2. The temperature or thermal conductivity sensing is made through the monitoring of the probe's resistance.

This type of probe showed a relatively small response time along with a high temperature coefficient. It has been extensively used to characterise the thermal responses of a variety of inorganic materials [39–41] and microsystem diagnosis [42–44]. Unfortunately, its large active area limits its use for probing the thermal exchanges at the sub-micrometer scale. In addition, the reproductibility over time was limited due to wearing and bending of the Wollaston wire [35]. It was progressively replaced by the microfabricated probes that did not suffer these limitations.

Thermocouple probes In thermocouple probes, the temperature sensing is performed through the passive measurement of the thermovoltage across a thermocouple junction. These probes are microfabricated and generally consists of superposed layers of different metals that are isolated by Si_3N_4 except in the active region where they overlap and thus make the thermoelectric junction. One popular pair of materials for these junctions are Cr and Au as they have a good mutual adherence, present a relatively high difference of Seebeck coefficients and are readily available in cleanrooms for other purposes [34, 45]. SEM images of a Cr/Au probe are presented in Figure A.0.3.

The miniaturisation of the tip and sensing element lowered the response times and improved the spatial resolution. This holds true for all the microfabricated probes presented in the following paragraphs.

Doped Si probes Doped Si probes were first fabricated by *IBM* for high-speed nanoscale lithography [35]. These probes have two high doped Si cantilevers which are joined by a

weakly doped region that supports the tip. This high resistivity region acts as the sensing element of the probe. These probes are only operated in active mode. They offer overall comparable performances to the other microfabricated probes with especially sharp tips with radii around $10nm$ [35]. A review of their applications can be found in [46]. A SEM image of a realisation of this type of probe can be found in Figure A.0.4.

Microfabricated probes with metallic thin film resistors This type of microfabricated probes uses a metallic thin film as a thermistor. This film is deposited as near as possible to the tip apex. These probes can be used in passive and active modes depending on the intensity of current used for the temperature sensing. A wide variety of materials can be used depending on the temperature range considered. Due to their metallic resistance, it could be expected for these probes not to behave well in high magnetic field due to their high magnetoresistance but no work studying explicitly this could be found. An analysis of their potential for quantitative analysis can be found at [47] and examples of designs for such probes are presented at [48, 49].

2.2.3 Low-temperature SThM : potential materials

The operation of SThM probe at cryogenic temperatures allows to study new phenomena. For example, in [50], the impact of ballistic transport at the edges of a graphene flake was imaged down to 150K. Another example can be found in single molecule experiment. The set-ups used can be brought to cryogenic temperatures. SThM was used in [51] to locally probe the temperature of the junction supporting the molecule, down to 50K. The Seebeck coefficient of a material also depends on the temperature. In [52], the local Peltier coefficient of graphene constrictions was obtained locally using a SThM probe. Overall, cryogenic local thermometry is a challenging field where only a few works can be found in litterature. It is likely that lowering the limit temperature of SThM operation would open new pathways for fundamental research and applications.

As widely shown [53–56], the Seebeck coefficient of most materials falls to nearly 0 below 50K. This prevents the use of thermoelelectric probes below this temperature. The doped Si probes will yield a very high resistance once they reach their ionisation regimes where the dopants are only partly ionised. Metallic resistance probes obviously do not suffer from this limitation but there still exists some limitations to this approach. First, below 25K, as the impact of phonons on the resistivity becomes negligible in metal resistances, the impact of defects and the sample's size come into play. This results in a flattening of the resistivity curve which does not allow a probe-to-probe reproducible measurement. Thus, a cryogenic thermistor probe requires specifically designed materials that keep their reproducibility down to temperature below 25K. In addition, since modern solid state experiments often imply high magnetic field, this thermometer should ideally

present a low magnetoresistance coefficient.

Zirconium nitride (ZrN_x) Zirconium nitride thin films were first investigated as cryogenic thermometers by T. Yotsuya *et al.* in [57]. As illustrated in Figure 2.2.1a and 2.2.1b, the ZrN_x amorphous thin films present a negative temperature resistance coeffcient (TCR) down to 1K. These thermometer showed a satisfying reproductibility after an important number of heating cycles. [57]. Their sensitivity although lower than modern Cernox sensors [58] is still suitable for cryogenic thermometry and they show a comparable response time. ZrN_x thin films also exhibit a weak magnetoresistance as illustrated in Figure 2.2.1c.

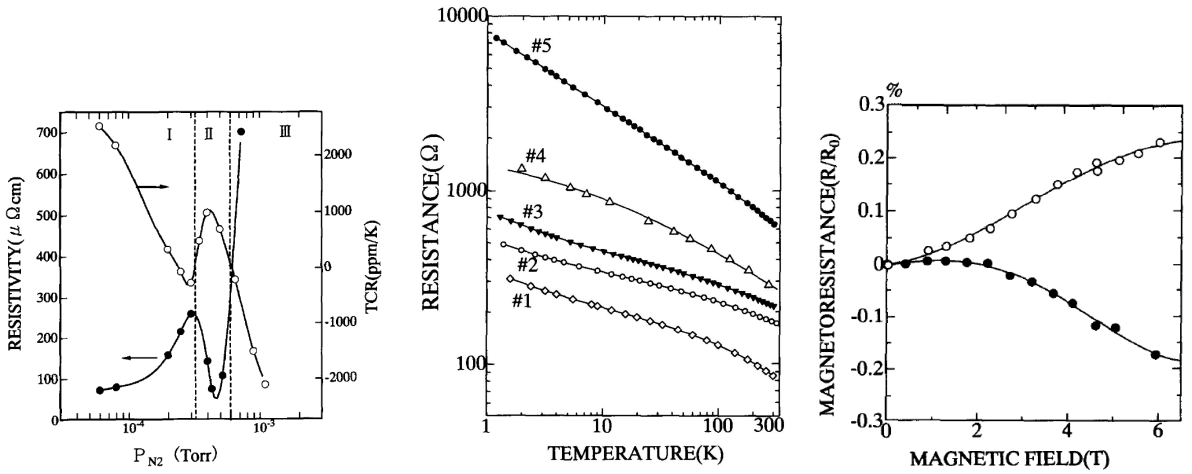

(a) Resistivity (○) and temperature resistance coefficient (●) at ambient temperature with respect to the N_2 pressures. Three distinct regions are delimited which corresponds respectively to metallic Zr, stoichiometric ZrN films and disordered amorphous ZrN_x.

(b) Resistance change with temperature, the different numbers correspond to decreasing pressures of N_2.

(c) Relative change of resistance with increasing magnetic fields in ZrN_x thin film samples at $4.2K$. ○ corresponds to a sample deposited at $200°C$ and ● to a deposition in the same conditions but at $400°C$. [57].

Figure 2.2.1: Resistivity measurement on ZrN_x thin films deposited with different N_2 pressures, all above the $1mTorr$ limit presented in Figure 2.2.1a, excerpted from [57].

C and Pt thin films Other materials classically used for low-temperature thermometry were investigated in this work since they can be locally deposited, as will be illustrated at subsection 4.7.2. Pt and C are used in commercially available low-temperature thermometers, as shown in [59, 60]. The carbon-based allows to reach temperatures down to 2K while the platinum-based are limited to 77K [61].

The sensitivities of C and Pt based thermometers can be found respectively in Figure 2.2.2 and 2.2.4 although they use two different definitions of sensitivity. Overall both thermometers allow satisfying sensitivities in their respective temperature ranges.

The relative magnetoresistances of C and Pt based thermometers at cryogenic temperatures can be found respectively in Figure 2.2.3 and 2.2.5. Again, they use different definitions of the magnetoresistance, as precised in the captions.

C-Pt alloy thin films In [62], C-Pt nanowires were formed by focused ion beam induced deposition and used for cryogenic resistive thermometry. They allowed reliable temperature measurements between 8mK and 8K.

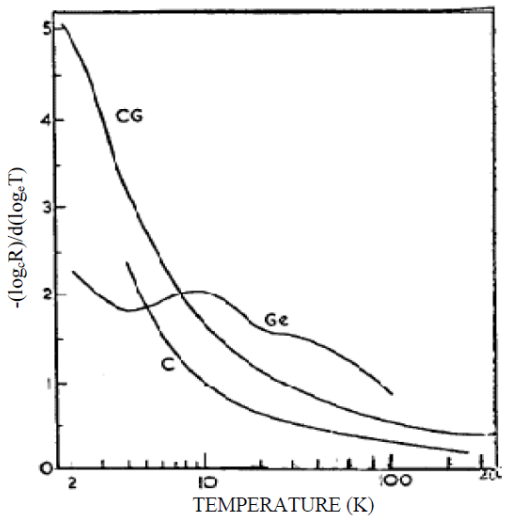

Figure 2.2.2: Sensitivity of different types of resistance thermometers with respect to temperature. Ge stands for germanium, CG for carbon-glass and C for carbon. [61]

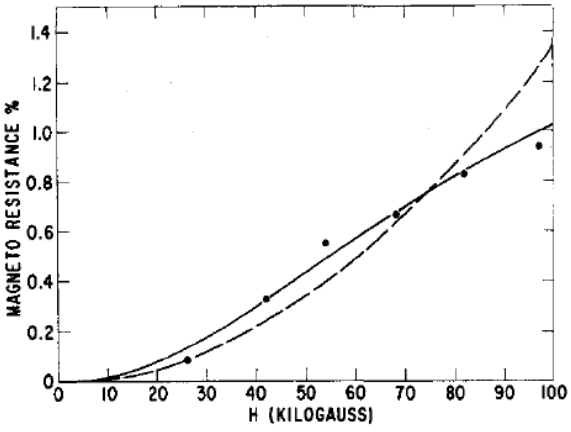

Figure 2.2.3: Magnetoresistance of a Allen-Bradley carbon resistance thermometer. The experimental data are indicated in dashed points. The magnetoresistance coefficient is defined as $MR = (R(H) - R(0))/R(0)$. The dashed line correspond to a semi-empirical model that can be found in [60] while the solid line corresponds to an empirical model from [63] from which the image is also excerpted.

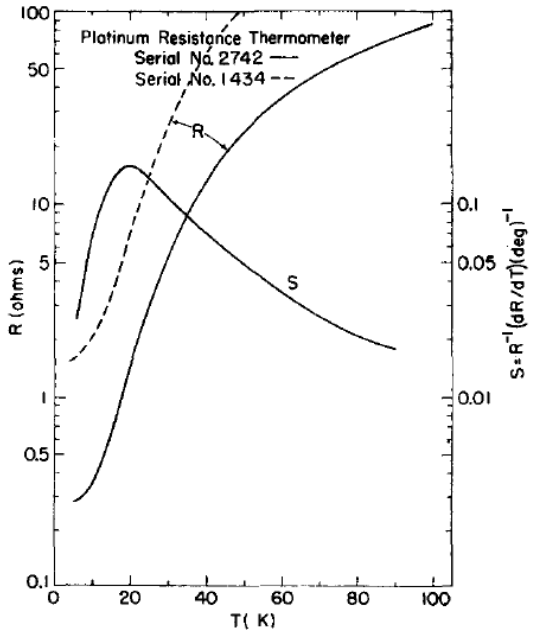

Figure 2.2.4: Sensitivity and resistance of two different Pt resistance thermometers with respect to the temperature. The vertical axis on the left corresponds to the resistance and the right to sensitivity. [64]

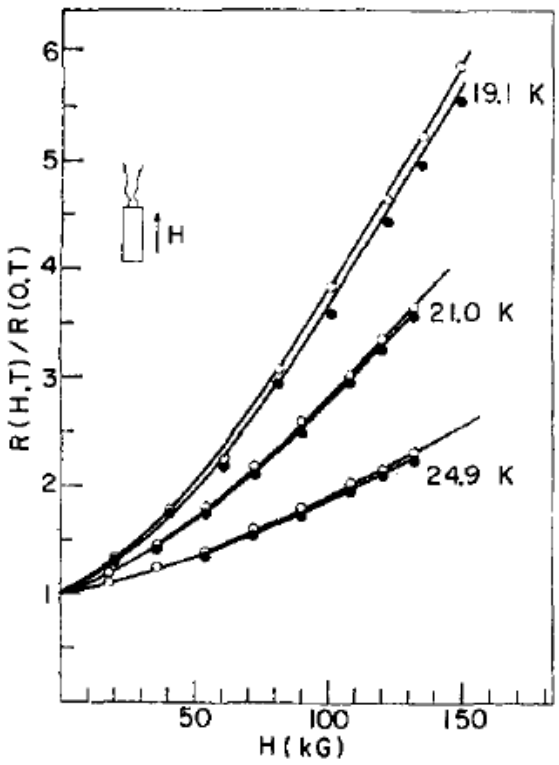

Figure 2.2.5: Relative magnetoresistance of a Pt thermometer at three different temperatures. The magnetoresistance coefficient is defined as : $MR = \frac{R(H)}{R(0)}$. [65]

2.2.4 Quasi-contact mode for SThM measurements

Usually, when performing AM-AFM, one aims at reaching the "periodic contact" region indicated on Figure 2.1.1. This corresponds to an intermittent contact between the tip and the surface also called "tapping mode". In SThM, the tip needs to stay in contact to avoid transient regime effects on temperature measurements. A solution to this problem lies in the quasi-contact region. In this regime, the tip stays in contact with the surface while the cantilevers keep vibrating. Using a soft cantilever would allow to image the topography while staying in contact with the surface.

As with any signal measurement, a steeper curve yields a better sensitivity. This sensitivity will help the feedback loop to adjust to small modifications of the topography. As illustrated in Figure 2.1.1, the quasi-contact mode shows a lower sensitivity compared to intermittent contact but it should still allow to scan a surface, theoretically.

So far, no work did feature a topography obtained with this imaging mode. Achieving topography measurement in this contact regime would allow to perform SThM measurements with a self-sensing scheme using the Akiyama design that will be introduced in section 2.3. Eliminating the parasitic heating induced by the laser feedback would improve

greatly the precision of the temperature measurement. This new type of SThM probe would also simplify calibration and improve the lateral resolution of the technique.

2.3 Akiyama probe

As stressed in subsection 2.2.3, parasitic heating must be reduced as much as possible to improve the reliability of the measurement and the radial resolution in cryogenic SThM. In order to get rid of the heating generated by the laser in a classical AFM set-up, one needs to find another way to measure the deflection of the tip. Self-sensing schemes rely directly on the measurement of the capacitance of the tuning fork, as explained in subsection 2.1.2. The interaction with the surface through the cantilevers will modify this vibration which in turn corresponds to a change in capacitance which can be reliably measured through the monitoring of the RF current used for excitation. The use of specifically designed cantilevers allow to increase the mechanical response of the tuning fork.

To achieve this, the Akiyama design replaces the single beam used in classical AFM tip by parallel beams connected to a transverse small beam supporting the tip. The beams are connected to both respective ends of the tuning fork, as illustrated in Figure 2.3.1. The vertical movement of the tip is obtained through the relief by transverse bending of internal stresses generated by the tuning fork's vibration [11, 22, 66, 67]. A finite element simulation of this behaviour can be found in Figure 3.5.1. The topography is then obtained through a dynamic measurement of the tuning fork capacitance in the particular quasi-contact mode that was described in subsection 2.2.4. This mode will allow to perform the temperature measurement in a contact mode while benefiting from the advantages of amplitude modulated topography measurements.

This geometry for scanning probe cantilevers allow a better sensitivity when using a self-sensing probe. In addition, as it does not rely on an external shaker, it allows to decouple the resonance frequency from the cantilever's spring constant. The tuning fork also offers an excellent vibration stability. [66]

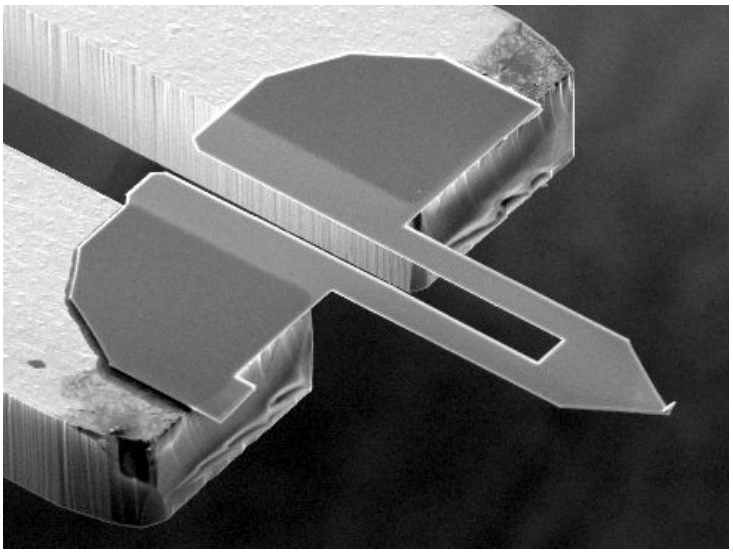

Figure 2.3.1: SEM image of an Akiyama probe from *Nanosensors*. The supporting structure is a commercial tuning fork. [67]

Chapter 3

Simulation of a scanning thermal microscopy probe

In the following sections, a short discussion on the advantages and limitations of finite element analysis in the context of nanometer scale cryogenic thermometry is provided. A simplified 1D thermal model of a SThM is presented to highlight the parameters requiring calibration and/or modelling to interpret a nominal SThM signal. The design degrees of freedom and objectives from the mechanical behaviour of the probe are then presented. Then, finite elements analysis (FEA) simulations are used to fix these design parameters. Based on these final dimensions, the calibration parameters for the 1D model are estimated. Finally a study on the impact of other parameters on the thermal performances of the SThM probe is reported.

3.1 Interests and limitations of FEA modelling

First, as for a lot of engineering applications, FEA offers valuable insights about the behaviour of the device, both mechanical and thermal. This tool allows to fix design parameters reliably and to simplify greatly the prototyping process. In addition, in the particular context of SThM, FEA simulations can help to estimate part of calibration parameters to help the interpretation of experimental data. Namely, the cantilevers and tip's thermal resistances and the effective heat loss coefficient in air were estimated from the simulations.

The thermal expansion of materials was not considered in this work. *Comsol* can simulate the thermal expansion and its impact on the mechanical behaviour of a device. Thus, further studies could produce tables of the resonance frequency or spring constant with respect to temperature.

Of course, since FEA is based on continuous equations, it fails to represent accurately the phenomena taking place at the nanoscale such as the quantisation of conductance

or, more importantly in this context, the phonon mismatch thermal resistance. In the diffuse mismatch model, first proposed by Swartz and Pohl in [68], the boundary thermal resistance is defined by the phonon transmission probability across the junction. This probability can be determined by estimating the overlap between the density of phonon states in both materials. Usually the material is considered isotropic and the usual phonon dispersion can be used. However, when the size of the object becomes comparable to the phonon wavevector, the phonon dispersion is strongly modified and an additional thermal resistance will arise due to the limited possible states for the phonons.

The phonon mean free path in silicon, a common material in MEMS, can be easily estimated in the context of the kinetic theory of gas. The Debye expression of the lattice thermal conductivity is recalled at Equation 3.1.1.

$$\kappa_L \;=\; \frac{1}{3} C_V v_s \bar{l} \tag{3.1.1}$$

where C_V, v_s and $\bar{l}$ are the heat capacity at constant volume in J $K^{-1}m^{-3}$, speed of sound and the phonon mean free path in silicon respectively.

The lattice thermal conductivity of silicon at ambient temperature was estimated by M. Park *et al.* to be 4.1W m−1 K^{-1} at ambient temperature [69]. The speed of sound can be obtained from the density ρ and the Young's modulus. Since silicon is an anisotropic material, the highest value of $144GPa$ was arbitrarily chosen. Its density is 2330 kg m^{-3}

$$v_s \;=\; \sqrt{\frac{Y}{\rho}}$$

where Y and ρ is the Young's modulus and density of silicon.

The lattice specific heat can be estimated using the Debye expression. Since the Debye temperature of silicon is 645K [69], one can use the low temperature simplification[1] and compute the lattice specific heat as follows.

$$C_V \;=\; 324 \frac{N}{V} k_B \frac{T^3}{T_D^3}$$

where k_B is the Boltzmann's constant, N/V the number of atoms per unit volume. The latter can be extracted from the Debye temperature definition knowing the speed of sound.

$$T_D \;=\; \frac{\hbar v_s}{k_B} \left(6\pi^2 \frac{N}{V} \right)^{1/3}$$

Thus the phonon mean free path in silicon at ambient temperature lies around $200nm$. This mean free path is comparable to the radius of the tip's apex. At this scale, the mentioned additional thermal resistance must be taken into account. It is accounted for in the

[1] A proper integration of the density of state function would be required in this context but this approach will allow a rough estimation.

Kapitza interfacial thermal resistance that will be introduced in section 3.2. This thermal resistance represents the main limitation of the FEA approach in the context of this project.

3.2 1D Analytical approach

The sample, tip and cantilever along with the environment constitute the whole thermal circuit. The thermal network is modelled as a 1D system with homogeneous temperatures in the different regions, as shown in Figure 3.2.1. 6 different temperatures are thus defined : $T_H, T_{t,c}, T_{s,c}, T_S, T_{ca}$ and T_{env} which corresponds respectively to the temperature of the heating element, which is also the one measured, the temperature of the tip at the contact point, of the sample at this same point, of the bulk sample, of the anchoring point of the cantilevers and the temperature of the environment.

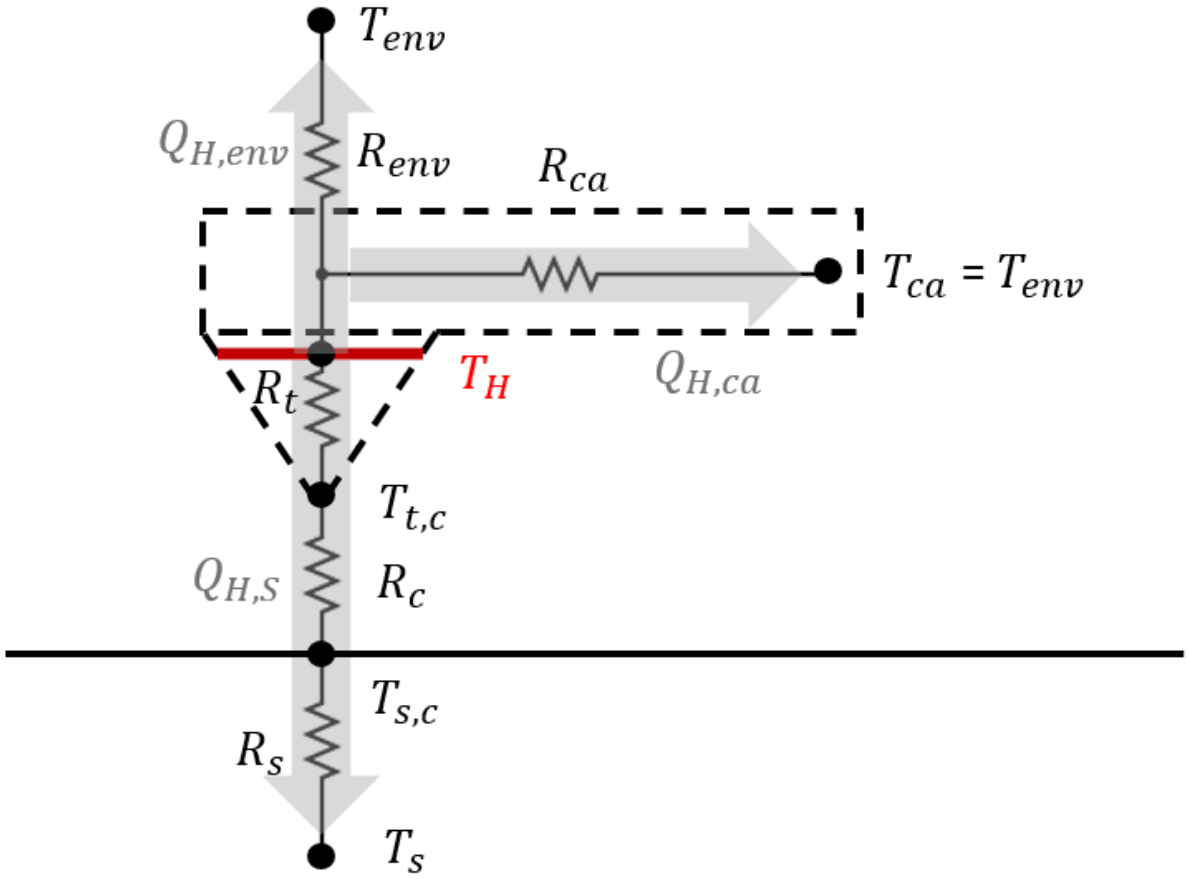

Figure 3.2.1: Thermal resistance network for a SThM probe in active mode. The heating element is represented in red. The cantilever and tip are presented in dashed line. The tip was represented out of contact for the sake of clarity but the SThM mode used in this work is a contact mode.

To simplify the problem, the direct heat flux from the sample's surface to the cantilever,

through radiation and convection, was omitted. The tip was also considered isolated from the environment. This last hypothesis can lead to inexact results at ambient pressure since the heat losses of the tip play an important role, as will be illustrated in section 3.6.

First, the sum of the three heat fluxes illustrated in Figure 3.2.1 must be equal to the DC electrical power injected in the heater, denoted $P = R_H I^2$.

$$P = Q_{H,env} + Q_{H,ca} + Q_{H,S} \tag{3.2.1}$$

The temperature of the heater T_H is supposed known, that means that the characteristics of the heater are well known or that it has been characterised otherwise. As already stressed, the temperature measured on the heater can be very different from the one of the sample. In the context of SThM performed in active mode, the parameter of interest is R_S. To link it with the thermal conductivity of the sample, one has to make a geometrical hypothesis. Considering an homogeneous and semi-infinite sample with a heated region that is hemispherical and homogeneous in temperature, R_S can be written as Equation 3.2.2. This expression is analytically derived in [70].

$$R_S = \frac{1}{4\kappa_S b} \tag{3.2.2}$$

where b is the effective contact radius and κ_s is the sample's thermal conductivity. In practice, it depends on the tip shape, depth of indentation or sample's roughness but also on the presence of a water meniscus [35]. It is also important to mention that b depends on the sample's thermal conductivity, as was shown by S. Lefèvre *et al.* in [71]. This parameter varies from one tip to another and depends on experimental conditions, it must thus be calibrated experimentally.

In addition to the b parameter describing the contact, the effective contact thermal resistance R_c takes into account the probe-sample thermal interaction on a disc of effective radius b. For example, the thermal contact resistance associated with the mismatch of phonon wavevectors, that was introduced in section 3.1, is comprised in these phenomena. This resistance requires experimental data and cannot be estimated from FEA simulations as already stressed.

As illustrated in Figure 3.2.1, one can write the heat flux from the heater to the sample $Q_{H,S}$ as the product of a temperature gradient and of three thermal resistances in series. This is done at Equation 3.2.3. Among these three resistances, R_c must be estimated from experimental data, R_S is the variable to be found and R_t will be estimated in this work using FEA simulations. The temperature of the heater is measured and the sample is assumed to be a satisfying heat sink far enough from the contact point and thus $T_S \approx T_{env}$.

$$Q_{H,S} = \frac{T_H - T_S}{R_t + R_c + R_S} \tag{3.2.3}$$

The thermal resistance of the cantilevers can again be estimated using Comsol, see section 3.7. The heat flux from the cantilevers to the environment through the gas conduction can be written as Equation 3.2.4 where h is an effective heat conduction coefficient. Its units are thus $W/(Km^2)$. A is the total contact surface between the cantilevers and the ambient air, it can be computed with Comsol.

$$Q_{H,env} = Ah(T_H - T_{env}) \tag{3.2.4}$$

This approach is highly idealised compared to reality and only valid in the context of this simplified model.

3.3 Parameters of interest and constraints

First the objectives of the design were defined based on the particular requirements of the SThM technique. The characteristics of commercial Akiyama AFM probes sold by Nanosensors [72] were also taken into account.

Cantilever stiffness For contact mode AFM, a soft cantilever is generally desired to limit damages on the surface [73, 74]. A soft cantilever is defined as a cantilever whose stiffness lies below 10N/m [75]. This stiffness must be adapted to the sample, with softer cantilevers for sensitive materials. For example, in biological applications, stiffnesses around 0.1 N/m are desired [74].

In this work, any spring constant over 1N/m, to be able to study crystalline materials, and below 10N/m to have a soft cantilever suited for contact mode will be considered satisfying. The technical guide of commercial Akiyama probes produced by Nanosensors gives tha value of 5Nm^{-1}. [72] This is where the interest of homemade tips is highlighted. The design parameters can be modified to obtain specific tips for particular applications.

Cantilever resonance frequency In an Akiyama self-sensing scheme the tuning fork must be resonant with the probe to achieve the best vibration amplitude. The desired frequency will thus be taken as 32.768 kHz, as this is the standard resonance frequency of mass-produced quartz tuning forks. The commercial guide provided by Nanosensors for their probes [72] indicates a resonance frequency of 50kHz.

SThM probe thermal resistance In the active mode, the measurement of the heat flux to the sample is based on the change of the resistance of the heater with temperature. For reasons explained in Appendix A, in the section about the electronic reading a SthM signal, the tip's thermal resistance must be reduced to the minimum to improve the signal over noise ratio (SNR). The cantilever thermal resistance must be maximised to increase the heat flux to the sample.

Design parameters and constraints The material choice is constrained by fabrication. The thickness, length and width of the cantilevers can be freely fixed. The dimensions of the tip can be chosen but the ratio between its height and with is fixed by the anisotropic etching described in section 4.5. More details can be found in [76]. The position of the heater can also be varied. The depth of indentation of the tip into the sample is not properly said a parameter since it is extremely complicated to characterise and control during an experiment, but its impact will also be studied since its modelling is required to interpret SThM experimental data [77].

3.4 Decoupling the mechanical and thermal problems

The first goal of the simulations was to assess the interplay between the parameters defining the thermal and mechanical behaviours of the probe. To reach this goal, the thermal resistance of the whole probe was computed for different cantilevers' dimensions. This was done by assuming a small pyramidal surface as the heat source at the end of the tip. This assumption was used to avoid complex calculations on the tip's region but does not represent a realistic distribution of heat since there should be no contact between the heater and the sample's surface in the final design. The anchors were considered thermalised. The thermal resistance was thus computed with Equation 3.4.1. Air diffusion was neglected.

$$R(x) = \frac{T_{\text{tip}} - T(x)}{Q} \tag{3.4.1}$$

where $R(x)$ stands for the thermal resistance of the section of the device comprised between the end of the tip, at $x_0 = 400\mu$m and x. Q is the heating power used. T_{tip} is the volume average of the temperature on the heating pyramidal shape used, so in approximation a point at the top of the tip. $T(x)$ is the temperature at the position x along the parametric line of Figure 3.4.2a.

The thermal resistance profiles obtained for a series of cantilever's thickness are presented in Figure 3.4.2b. The profiles are traced along one virtual line going from the tip's end to one of the two anchors. This parametric line is presented in Figure 3.4.2a. It appears that more than 75% of the device's thermal resistance is located in the tip region. In other words, the temperature profile is almost flat from the tip's base to the

anchors. This will allow us to model only the tip in further simulations and to apply a boundary condition of fixed temperature to the tip's base thus reducing the required computational power. It also appears that this hypothesis is less coherent as the thickness of the cantilevers diminishes.

Studies with varying lengths were also performed and led to the same conclusion. This is also apparent in Figure 3.4.2b since only for the thinnest cantilever does its length plays a role.

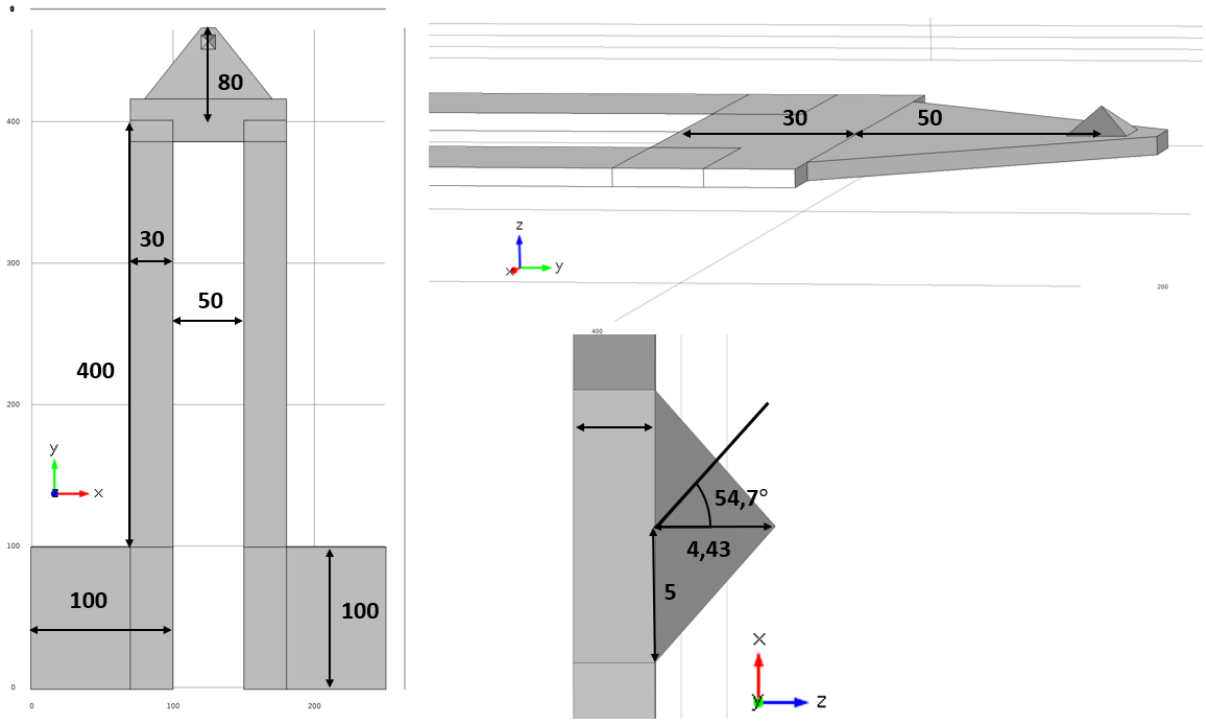

Figure 3.4.1: 3D model of an Akiyama probe with its dimensions as annotations. All dimensions are indicated in μm.

3.5 Mechanical behaviour

Akiyama's resonance mode As developed in section 2.3, the Akiyama probes rely on the relaxation of internal stresses through the transverse bending of the beam supporting the tip. This behaviour was successfully simulated when imposing a vibration along $\vec{x}$ and forbidding displacement along the two other axes to the pads. The corresponding simulated displacement fields are represented in Figure 3.5.1. This mode corresponds to the 1st resonance mode, as expected from litterature [78].

Resonance frequency The resonance frequency of the device was also computed using COMSOL. The frequency of the first resonance mode, illustrated in Figure 3.5.1,

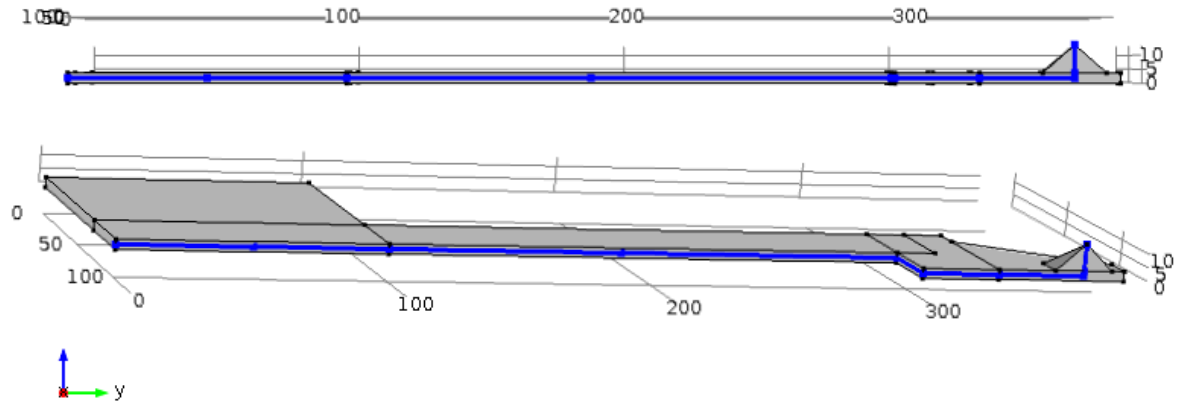

(a) Parametric line along which the thermal resistance is computed. The 3D model was cut in half to show the line.

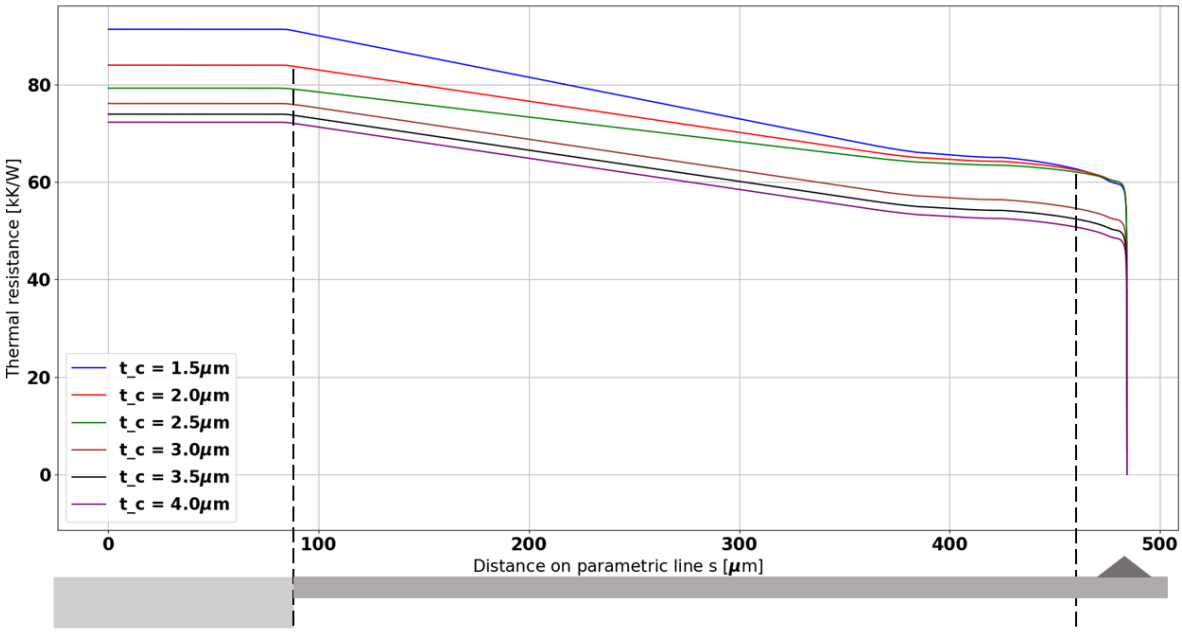

(b) Thermal resistance profile of an Akiyama SThM probe for cantilever thicknesses between 1.5 and 4 μm. The negative thermal resistance is an artefact due to the averaging of the temperature over the apex for the computations.

Figure 3.4.2: Thermal resistance mapping of a SThM Akiyama probe. The left extremity corresponds to contact pads with the tuning fork, and the right extremity corresponds to the tip.

is given for different lengths and thicknesses in Table 3.1. It can be seen that for the dimensions length = 400 μm and thickness = 3.0 μm, the resonance frequency of 30.2 kHz is close to the aimed value of 32.768kHz. The corresponding value is highlighted in red in the table, they will thus be the one chosen for the rest of the simulations. The Akiyama probes from *Nanosensors* have a reported resonance frequency of 50 kHz for a cantilever's length of 310μm and a thickness of 3.7μm. The predicted resonance

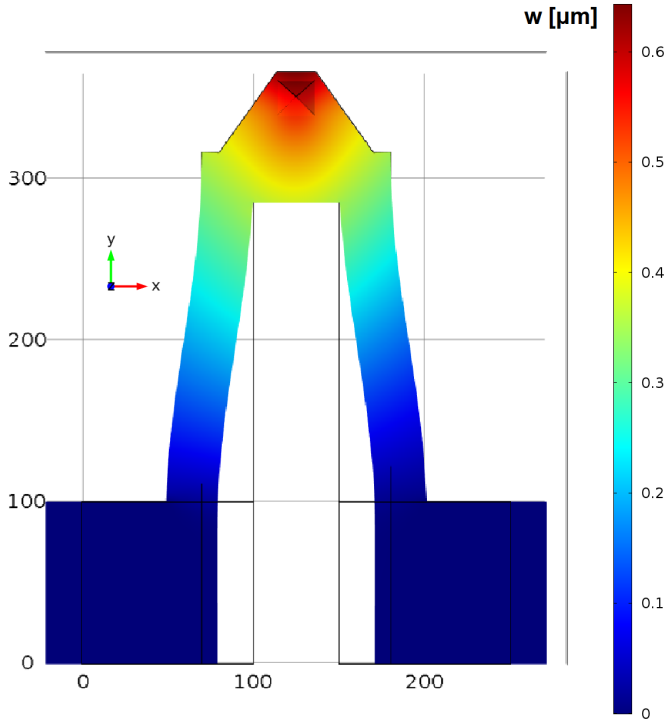

Figure 3.5.1: Deformation of an Akiyama probe under a strain along $\vec{x}$ of its pads. The displacement field along the $\vec{z}$ axis, denoted w, is represented with a colour scale. The deformation along the $\vec{x}$ and $\vec{y}$ directions are represented by the deformation of the device's volume. Its initial shape is indicated by solid black lines.

frequencies predicted for these dimensions in this work are close as can be seen at Table 3.1.

	$L_c = 250\mu$m	300	350	400	450	500
$t_c = 1.5\mu$m	47.2	30.6	21.51	15.98	12.35	9.84
2.0	63.1	40.87	28.73	21.34	16.49	13.14
2.5	78.91	51.13	35.93	26.69	20.62	16.43
3.0	94.7	61.38	43.12	32.03	24.75	19.72
3.5	104.49	71.6	50.32	37.37	28.87	23.0
4.0	126.25	81.81	57.5	42.69	32.99	26.28

Table 3.1: Frequency (in kHz) of the first resonance mode. Each line corresponds to a fixed beam length (in μm) and each column corresponds to a fixed beam thickness (in μm).

Spring constant The magnitude w of the displacement along $\vec{z}$ of the part supporting the tip was observed using COMSOL under a force of magnitude $F = -1\mu$N applied on the tip in the same direction. Two different parametric sweeps were performed : one sweep on the thickness of the beams (from 1.5 to 4 μm) and one sweep on the length of the beam (from 250 to 500 μm). The corresponding effective spring constant was then plotted on

Figure 3.5.2. By considering the device dimensions that were identified in the last paragraph ($L_c = 400$ μm and $t_c = 3.0$ μm), the simulated effective spring constant was found to be equal to 1.75 N/m, which falls in the window fixed at section 3.3. Parametric studies on the cantilever thickness and length can be found in Figure 3.5.2a and 3.5.2b respectively.

Furthermore, the analytical study of the effective spring constant was performed. As the device is composed of two parallel beams fixed on each pad of a tuning fork, the model of two parallel beams with identical effective spring constants was chosen (Equation 3.5.1).

The effective spring constant of a single beam was determined using the cantilever beam model, recalled at Equation 3.5.1, with E the Young modulus of Si, taken as 202 GPa. w is the width of the beam, t its thickness and L its length. Those different values correspond to the ones suggested on Figure 3.5.2a and 3.5.2b : $L_c = 400$ μm and $t = 3.0$ μm. Finally, the resulting value was found to be equal to 1.28 N/m. This slight discrepancy with the value of 1.75Nm^{-1} could be explained by the transverse beam that reduces the effective lengths of the long beams.

$$
\begin{aligned}
k_{\text{eq}} &= \frac{F}{u} && (3.5.1)\\
&= k_1 + k_2 = 2k_1 && (3.5.2)\\
&= \frac{Ewt^3}{2L^3} && (3.5.3)\\
&= \frac{(202 \times 10^9) \times (30 \times 10^{-6}) \times (3.0 \times 10^{-6})^3}{2 \times (400 \times 10^{-6})^3} && (3.5.4)\\
&= 1.28 \text{ N/m} && (3.5.5)
\end{aligned}
$$

However, this value of effective spring constant is high enough in order to limit the influence of the thermal noise on the displacement of the tip. Indeed, as developed in Equation 3.5.6, the displacement induced by the thermal noise at ambient temperature is an order of magnitude lower than the size of an atom. [19] This noise will indeed be lower at cryogenic temperature, which is an advantage. As the mechanical $1/f$ noise is not dominant in MEMS [19] and since the mechanical thermal noise was estimated to be very low, the conclusion that the noise is not the limiting factor in topographic mapping can be drawn.

$$
x_{\text{rms}} = \sqrt{\frac{k_B T}{k_{\text{eq}}}} = \sqrt{\frac{1.38 \times 10^{-23} \times 298.15}{1.28}} = 0.54\text{Å} \qquad (3.5.6)
$$

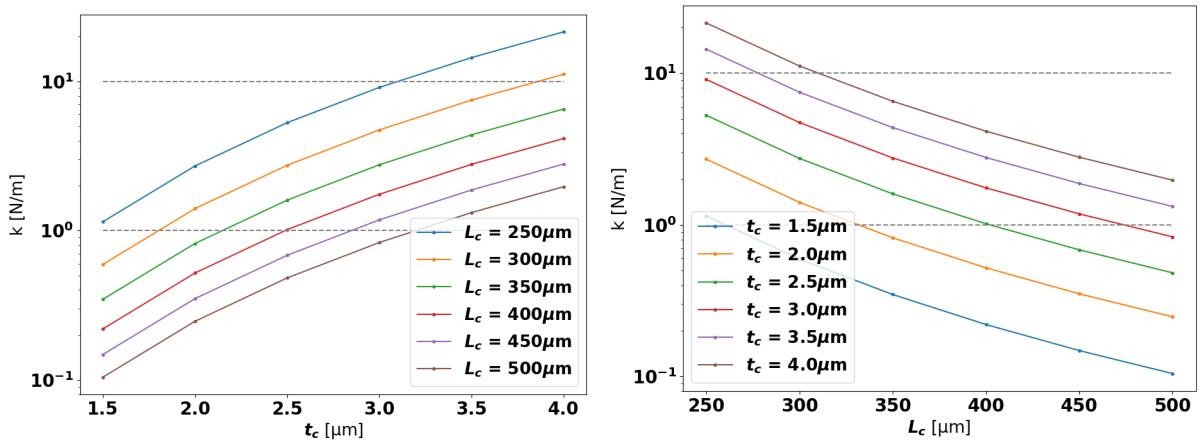

(a) Effective spring constant as a function of the thickness of the beams.

(b) Effective spring constant as a function of the length of the beams L_c.

Figure 3.5.2: Spring constant k of an Akiyama probe obtained by FEA. A force of -1μN was applied on the tip's apex and the vertical displacement was used to extract k. The grey dashed lines represent the boundaries defined in section 3.3.

3.6 Impact of various parameters on the performances

As the assumption of decoupling between the mechanical and thermal behaviour of the probe was shown to be reasonable in section 3.4, the tip can be analysed alone. The performances of the SThM tip were thus investigated under the influence of different design and operating parameters.

Illustrations of the 3D model used for simulations as well as a typical temperature map can be found respectively in Figure 3.6.2a and 3.6.2b. The heating resistance is now simulated in the form of rectangular ring placed around the tip. The sample region is represented by a block subtracted by the tip indentation region. In summary, the boundary conditions are : volume heating on the heater and thermal sinks at the lateral faces of the air cubes, the faces of the sample not contacting the tip and the basis of the tip.

Impact of heater location In a SThM probe, a large portion of the heat generated in the heater will leave the device through the cantilevers and the pads as this path shows a lower thermal resistance, as illustrated at section 3.4. To optimise the heat flux going through the sample, the heater must be placed as close as possible to the sample's surface. In practice, it cannot be in contact although to avoid having an electrical contact. A 3D model of a SThM tip with an annular heater with a horizontal thickness (perpendicular to the tip's surface) of 50nm and a height 200nm. One typical map of temperature obtained with this model is presented in Figure 3.6.1. The heater is positioned at 4μm from the tip base which corresponds to a factor of 0.9. The factor is the ratio of the height of the heater over the total height of the tip, 4.49μm. The ratio between the heat flux through

the basis Q_{base} and the tip Q_{tip} with respect to this factor is presented in Figure 3.6.1 for different indentation depths. By reducing the thermal resistance between the heater and the sample, the heat flux towards the latter is increased.

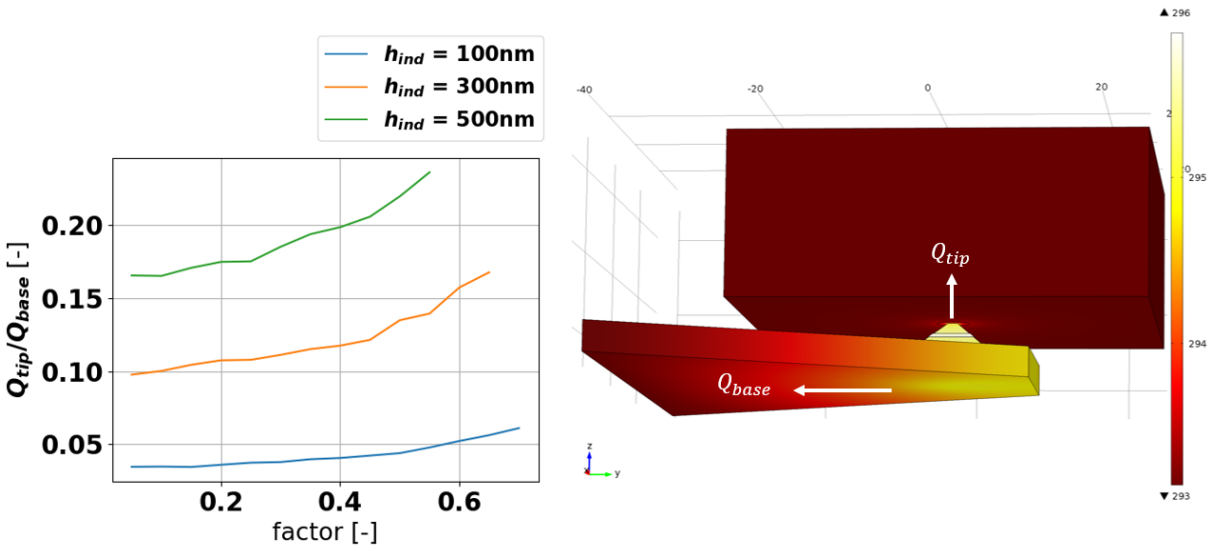

Figure 3.6.1: **Left :** Ratio of the heat fluxes through the apex Q_{tip} and the base $Q - base$ of a SThM probe for different indentation depths. **Right :** Associated thermal map on the 3D model, the heat fluxes Q_{tip} and Q_{base} are represented.

Impact of vacuum Conduction[2] in the ambient gas represent an alternative heat path that reduces the sensitivity of the SThM in addition to lowering its lateral resolution. To assess the impact of air conduction on the system, two different cases were considered : the operation of the probe at ambient pressure (1 bar), and its operation under ultra high vacuum conditions (10^{-10} bar). In the diffusive regime, the thermal conductivity of a gas is independent of its pressure. This is not true anymore in the molecular regime, thus when the mean free path of gas particles becomes comparable to the dimensions of the chamber. In this case, inter-molecular interactions become negligible and thus the kinetic theory of gas is a good approximation of the system. After some algebra, which is further developed in [79], one can obtain :

$$\kappa = \frac{\bar{v} M C_v D p}{3 R T_0} \tag{3.6.1}$$

where $\bar{v}$ is the average particle velocity, D a characteristic chamber length, T_0 the ambient temperature, C_v the heat capacity of air and M its molar mass. R is the perfect gas constant $R = k_B N_A$ and p is the pressure of the chamber.

[2]Convection and radiation are important also heat losses for the system but for the same reasons presented at section 3.7, they won't be discussed here.

The molecular regime was implemented in Comsol by modifying the *piecewise* function associated with the κ of air in the material library. This function was thus dependent on a parameter p representing the pressure.

The volume averaged temperature of the heater and the temperature of a circular region in the sample, near the contact location, were then plotted against the depth of indentation of the tip in a thermally conducting material (gold) and a thermally insulating material (alumina), for the two pressure regimes and with respect to the indentation depth. The results are presented in Figure 3.6.2. The 3D model used and one associated temperature map are presented in Figure 3.6.2a and 3.6.2b respectively.

For the ultra high vacuum regime (Figure 3.6.2, lower subfigure), it can be seen that the temperature of the tip drops quickly after the contact. The same plot was done under ambient pressure conditions (Figure 3.6.2, upper subfigure). It has the same global behaviour as in the previous case, but several differences can be spotted. First, one can see that the temperature of the alumina increases before the indentation of the tip into the sample, as highlighted in Figure 3.6.2. This illustrates that, at ambient pressure, the tip is heating the surface even if not in contact.

A temperature profile was measured radially, from the contact point, as illustrated in the inset image of Figure 3.6.3. The temperature makes a plateau in the silicon tip as it is a much better heat conductor ($\kappa_p = 130$ W m^{-1}K^{-1}) compared to the sample ($\kappa_s = 35$ W m^{-1}K^{-1}). The curves are very close but it can be seen that the distribution of heat is wider at ambient pressure, in the order of the nanometer.

This is why SThM is ideally operated under ultra high vacuum conditions. Indeed, the heat transfer via air increases the size of the probed region on the sample. This induces a loss of lateral resolution. The absence of water meniscus is also a major advantage. [35] In addition to the impact of vacuum, the importance of the indentation depth is made clear. The measured difference of temperature depends linearly on it according to the simulations. Generally, the indentation depth is considered constant through the scanning of a region, which is a good approximation only when considering materials with close Young's moduli. This limitation can only be overcome with analytical models or simulations including the shape of the tip and the mechanical properties of the sample.

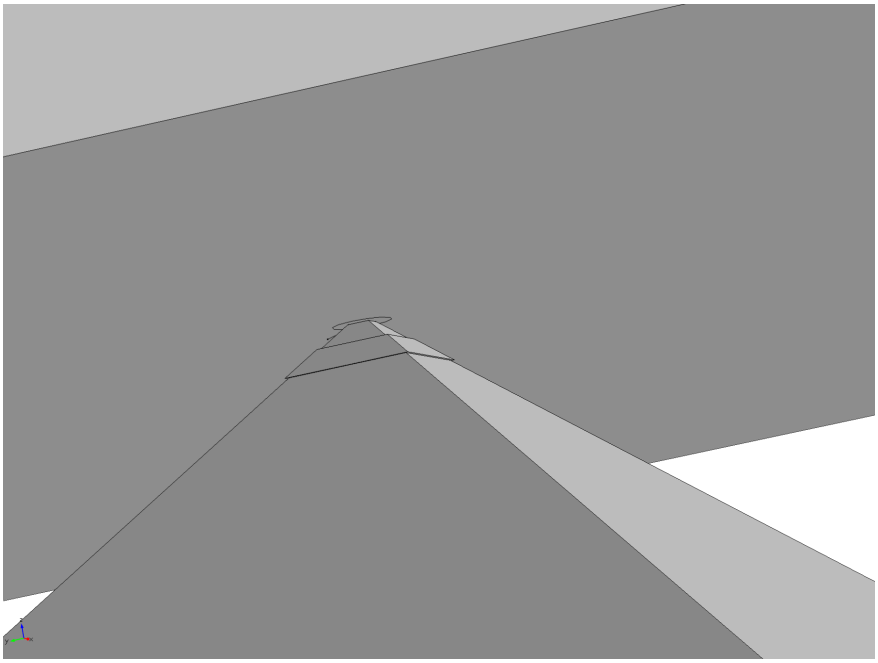

(a) Full 3D model used for the simulations.

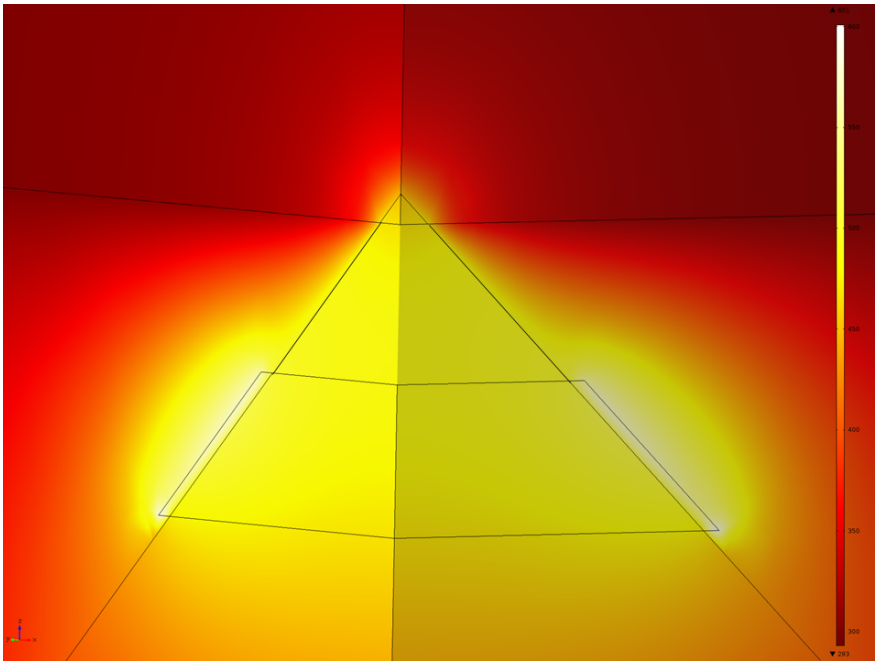

(b) Distribution of temperature over a SThM probe. The block of air is on the left. The two faces presented correspond to the cross-sections in the $x-z$ and $y-z$ planes from the 3D model in Figure 3.6.2a.

Figure 3.6.2: Simulation of the tip of a SThM probe in an ambient air environment with its indentation in a sample surface.

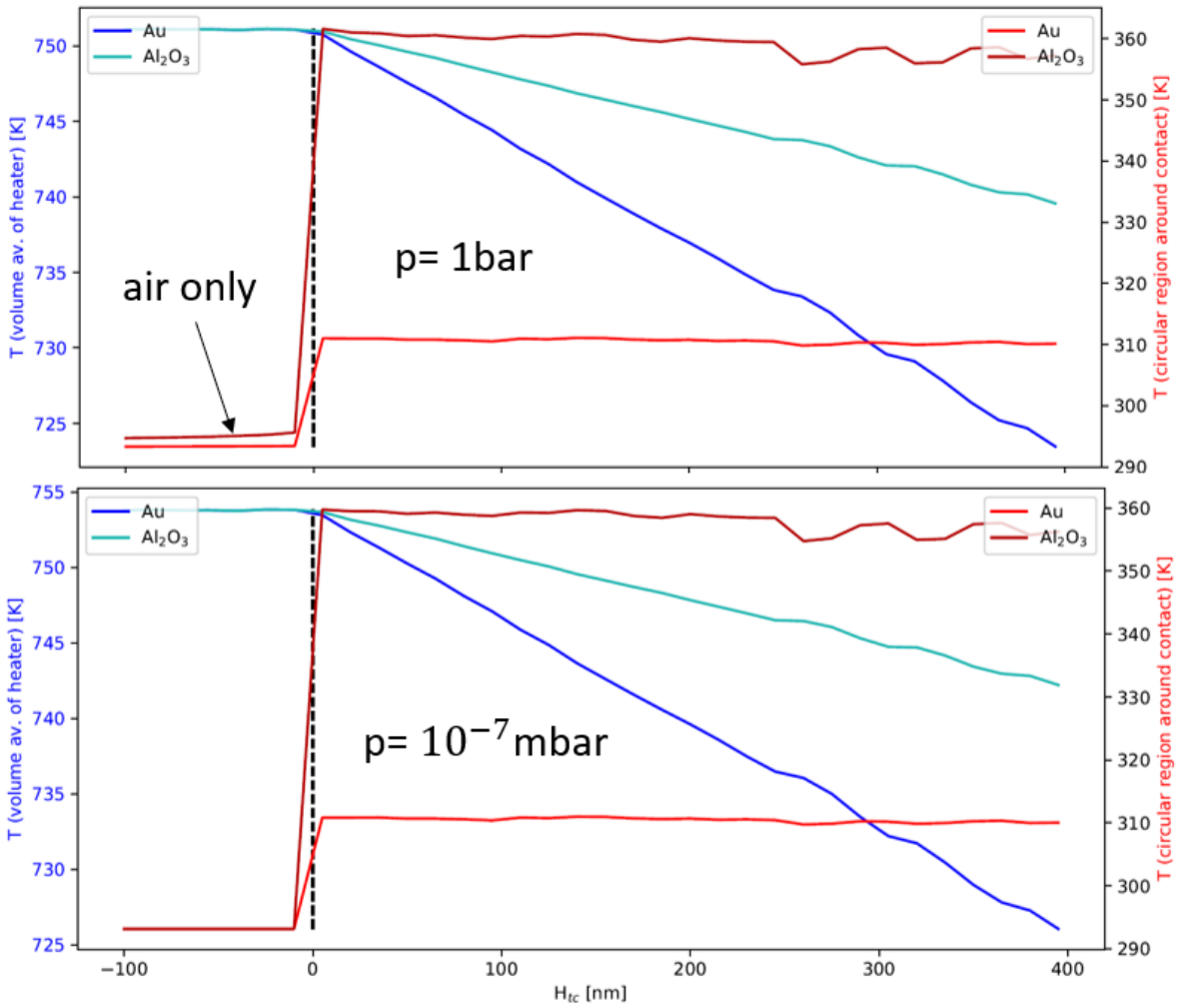

Figure 3.6.2: **Left, blue scale** : Volume average temperature of the heater. **Right, red scale** : Line averaged temperature of a circular region in the sample, around the contact location at ambient pressure. All the curves are plotted as a function of the indentation depth of the tip into the sample. The darker curves correspond to a thermal insulator (Al_2O_3) while the two lighter correspond to a good thermal conductor (Au).

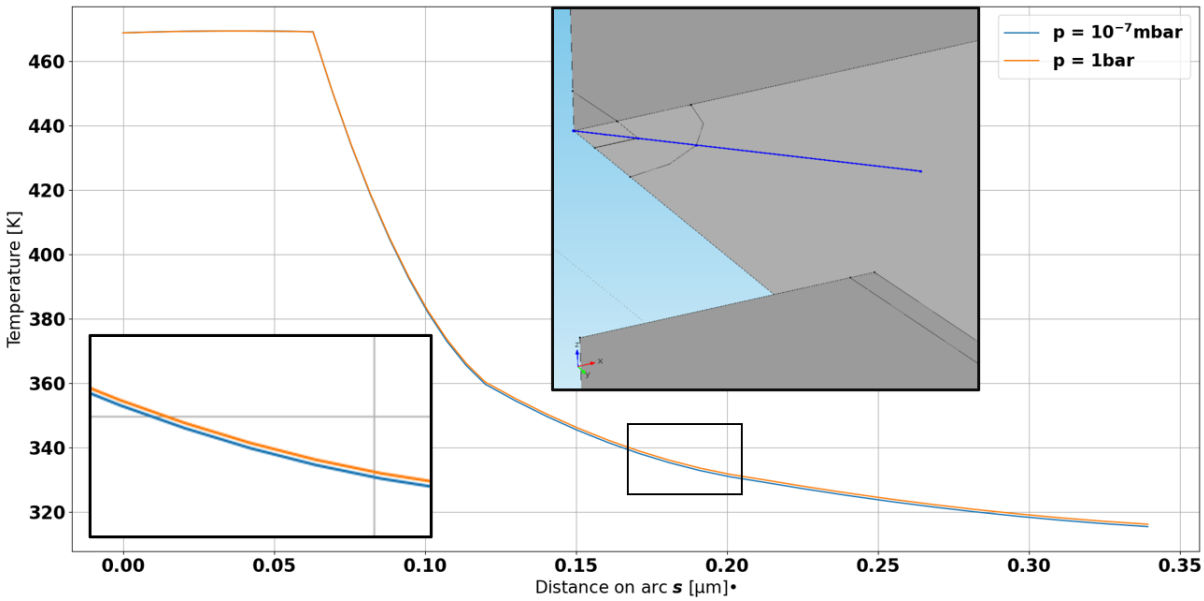

Figure 3.6.3: Temperature profile along a parametric line on the sample surface, illustrated in the inset image, in blue. The sample is a poor heat conductor Al_2O_3

Limitations in sample's thermal conductivity The better the thermal conductivity of the sample, the smaller the thermal resistance one aims at measuring. The general guideline, leaving apart the interface resistance and the geometrical optimisation of the tip, states that the thermal conductivity of the tip must be significantly greater than the one of the studied sample. This is expressed in the following Equation 3.6.2, excerpted from [80]. Simplifying assumptions on the probe's geometry have been made.

$$\frac{\Delta Q}{\Delta T} = \frac{3}{4}\frac{\kappa_p \pi b}{1+\kappa_p/\kappa_s} \quad ; \quad \lim_{\kappa_s >> \kappa_p} \frac{\Delta Q}{\Delta T} = \frac{3}{4}\kappa_p \pi b \quad ; \quad \lim_{\kappa_p >> \kappa_s} \frac{\Delta Q}{\Delta T} = \frac{3}{4}\kappa_s \pi b \tag{3.6.2}$$

where ΔQ is the heat driven in the sample corrected by heat losses, ΔT is the difference in temperature between the tip neighbouring region in the sample and the heater. b is the contact radius, κ_s and κ_p are the sample and probe thermal conductivities.

The analytical expression of Equation 3.6.2 was computed for a series of sample thermal conductivities κ_s and effective contact radii b. The result illustrates what was derived before, the right of the graph corresponds to a situation where the system is only measuring the probe's thermal conductivity. On the left of the graph, the signal measured is insensitive to the probe's thermal conductivity, this is the ideal situation. In practice, as highlighted in [80], one must assume that the SThM's probe thermal conductance has an non-negligible impact on the signal assured.

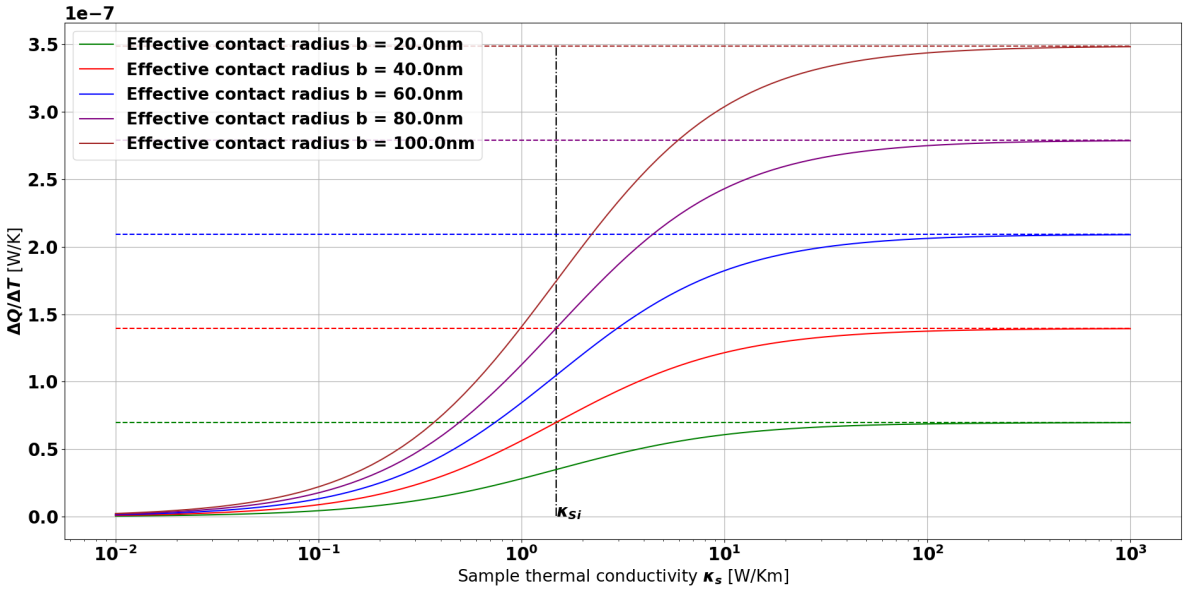

Figure 3.6.4: Measured signal $\Delta Q/\Delta T$ with respect to the probed sample's thermal conductivity. The probe is in silicon, its thermal conductivity is indicated with a vertical dashed line. Each curve correspond to a different indentation depth. The horizontal dashed lines correspond to the convergence when $\kappa_s >> \kappa_p$, as indicated at Equation 3.6.2

3.7 Estimation of the calibration parameters

In this section, the different parameters that need to be estimated to interpret a nominal SThM signal will be computed. These parameters were analytically identified at section 3.2. It is clear that these parameters depend directly on the dimensions of the SThM probe. This section serves as an example of what can be achieved with FEA simulations. In practice the whole process should be done with the precise dimensions of the device, estimated after the fabrication. The following simulations were realised using the dimensions identified at section 3.5.

Cantilevers and tip thermal resistances To avoid the important the computations required to simulate the whole device with an annular heater, an indirect path was chosen to obtain the thermal resistances of the two concurrent heat paths. These heat paths, ignoring air conduction, are "from the heater to the sample" and "from the heater to the pads", as illustrated at Figure 3.2.1.

First, the thermal resistance whole device R_{tot} can be directly estimated from the thermal map that was obtained at section 3.4. In Figure 3.4.2b, the curve makes a plateau once in the pads' region. The value of $83.56kK/W$ can be extracted from the data. This is only true if one considered the heating region at the apex as a point.

$$R_{tot} = \frac{Q}{T_{tip} - T_{env}} = 83.56\text{kK/W} \tag{3.7.1}$$

Then, using a model of the tip only with an annular heater, one can obtain the thermal resistance of the region between the heater and the sample's surface. The 3D model used is the same as the one used to assess the impact of the heater's location at section 3.6 but after removing the air block. By subtracting this resistance from the one obtained for the whole device, one thus obtain the thermal resistance of both competing heat paths. With a factor of 0.9, as defined at section 3.6, the resulting thermal resistances are $R_t = 30.78$ kK W^{-1} and $R_{ca} = 52.76$ kK W^{-1}. These value are coherent considering that the tip region is small but is also the narrower of the structure.

Effective air heat conduction coefficient To estimate the effective air heat conduction coefficient h, the whole SThM probe, shown in Figure 3.4.1, is placed inside an air cube whose dimensions are way over the one of the probe model[3]. A heat flux of 10mW is applied to the apex of the tip. The average temperature of this region, denoted T_{tip} again,

[3]The proper approach would be to use the temperature of a point in the system and to realise a convergence study to be sure that the cube's dimensions are sufficient. In this work, the dimensions of the cube used in [81] were kept as their device is comparable in dimensions.

is computed and equal to 399.24K. The input heat flux is obtained by integrating on the base of the tip and is equal to 4.564mW. The output flux corresponds to the normal heat flux through the connections between both cantilevers and their respective pads. Its value is 3.325mW. The area of the cantilevers and the trapezoidal base of the tip, noted A can be obtained by integration in *Comsol* and its value is 0.4997mm^2. These values allow to obtain the effective air conduction coefficient using Equation 3.7.2. Since the air is considered as a solid block, this value only indicates the losses by conduction. No convection or radiation effect was accounted for in this estimation.

$$h_{ca} = \frac{Q_{in} - Q_{out}}{A(T_{tip} - T_{env})} = 24.71\text{W}/(\text{K}m^2) \tag{3.7.2}$$

This value is comparable to the coefficient for a free air convection. It was reported to lie between 2.5 and 25W/(Km^2) in [82].

It is interesting to note that the difference between the total heat flux 10mW and the heat going through the base pf the tip 4.564mW represents the air conduction over the tip's region. This heat flux represents half of the energy balance. Thus, ignoring air losses over this region is a poor approximation but a more complicated treatment than the one provided at section 3.2 will be required to estimate this heat loss.

Chapter 4

Fabrication of a cryogenic scanning thermal microscopy probe

This chapter is dedicated to the fabrication of a SThM probe suited for thermal conductivity measurements at cryogenic temperatures. As justified in chapter 2, this probe will use in active mode and thus requires a heating element. An Akiyama design was chosen for the cantilevers as it allows improved performances with a self-sensing feedback, as explained at section 2.3. This probe will be fabricated using microfabrication techniques. Due to time limitation, the full device could not be realised but each step was independently developed.

The following sections present the preliminary results obtained. This chapter begins with an overview of the fabrication process as a whole, of the photolithographic mask used and of the cleaning procedures. After that, the sections follow the chronological order of the fabrication. An important number of resources were placed in the appendices, see Appendix A, for the sake of clarity. The supporting information might be helpful for future experiments that aim at reproducing these results.

4.1 Process overview

The fabrication process overview is illustrated in Figure 4.1.1.

As illustrated in litterature [83–85], the anisotropic etching of silicon can be used to define pyramidal AFM tips using an oxide mask defined by photolithography. A silicon on insulator wafer (SOI) is first thermally oxidised in a furnace. A photoresist is spin-coated, exposed using a mask and developed. Then, a buffered HF solution (BHF) is used to print in the oxide the photolithographic mask. This pattern includes 10μm per 10μm squares of oxide that will locally protect the silicon. This layer is used as a mask for a second etching in TMAH that will attack anisotropically the silicon while leaving the oxide mask almost undamaged (selectivity > 1000 [76]). The planes with a normal of the family $< 111 >$ will be etched slower, and will reveal planes inclined at 54.7°. This step defines the tip under

the islands of oxide left after the BHF etching. The caps naturally fall when the different $< 111 >$ planes connect.

A thick negative photoresist is spin-coated over the patterned surface. After exposure and development, its trenches define the future contact lines and pads. Gold is then deposited by physical vapour deposition (PVD) since it is a good electrical conductor and the photoresist is stripped away. It is thus a lift-off technique.

A photoresist (PR) is spin-coated on the surface. Using a photoresist thickness lower than the AFM tips height, their top is not covered by the resin. Zirconium nitride (ZrN_x) is then deposited by reactive magnetron sputtering on the tip and the PR. This material was chosen due to its desired properties for cryogenic thermometry, as illustrated at subsection 2.2.3. The photoresist is then stripped away leaving only the tips covered with ZrN_x.

Finally, the beams are defined on the front side of the SOI wafer by the Bosch process on a thick photoresist mask. The final step is the release of the device using the Bosch process.

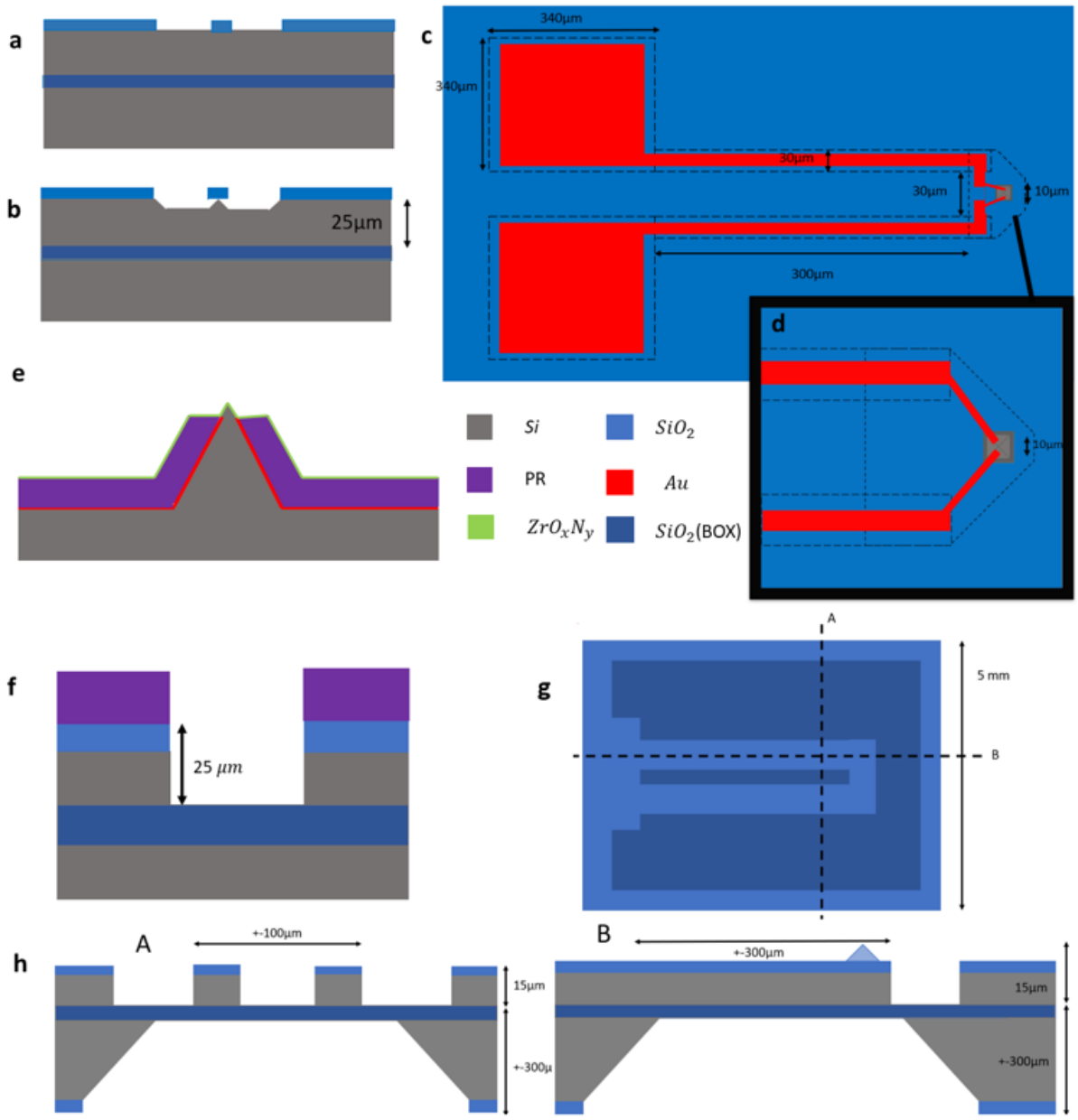

Figure 4.1.1: Illustration of the fabrication process for an Akiyama SThM probe. (**a**) SOI wafer after thermal wet oxidation of the top face. (**b**) Tip definition below the defined oxide mask using TMAH anisotropic wet etching. (**c**) PVD of gold followed by a lift-off. (**d**) Zoom on the tip region. (**e**) Reactive magnetron sputtering of ZrO_xN_y on partially covered spin-coated AFM tip. (**f**) Illustration of the deep dry etching (Bosch process) on the top face of the SOI wafer. (**g**) Top view of the top face after the deep dry etching. Cross-sections are labelled by A and B. (**h**) Cross-sections of **g** after release of the device through back face KOH etching.

4.2 4-quadrants photolithographic mask

The mask consists of 4 quadrants and is thus rotated by 90° between each photolithographic step.

The quadrant labelled 1 contains an array of $10\mu m \times 10\mu m$ squares that are used to define the oxide caps that in turn defines the tips during the TMAH etching as explained at section 4.5. The second quadrant presents the design for the electrical contacts to be deposited on the tips using a negative tone photoresist. The third quadrant is used to define the beams and contact pads in the front side of the SOI wafer. Finally, the fourth quadrant will be used to etch the back face of the wafer for the final release of the design. Alignment sights were placed nearby each quadrants as well as on the cardinal axes with respect to the 90° symmetry.

The different quadrants consist of 5×5 pattern arrays. These arrays contains rows of 5 cantilevers of the same length, from 260μm to 340μm and columns of cantilever with the same widths, from 30μm to 45μm.

A second mask, referred to as the prototyping mask, was used, it features dense arrays of squares with the following sizes : 1 μm, 2.5 μm, 5 μm and 25 μm.

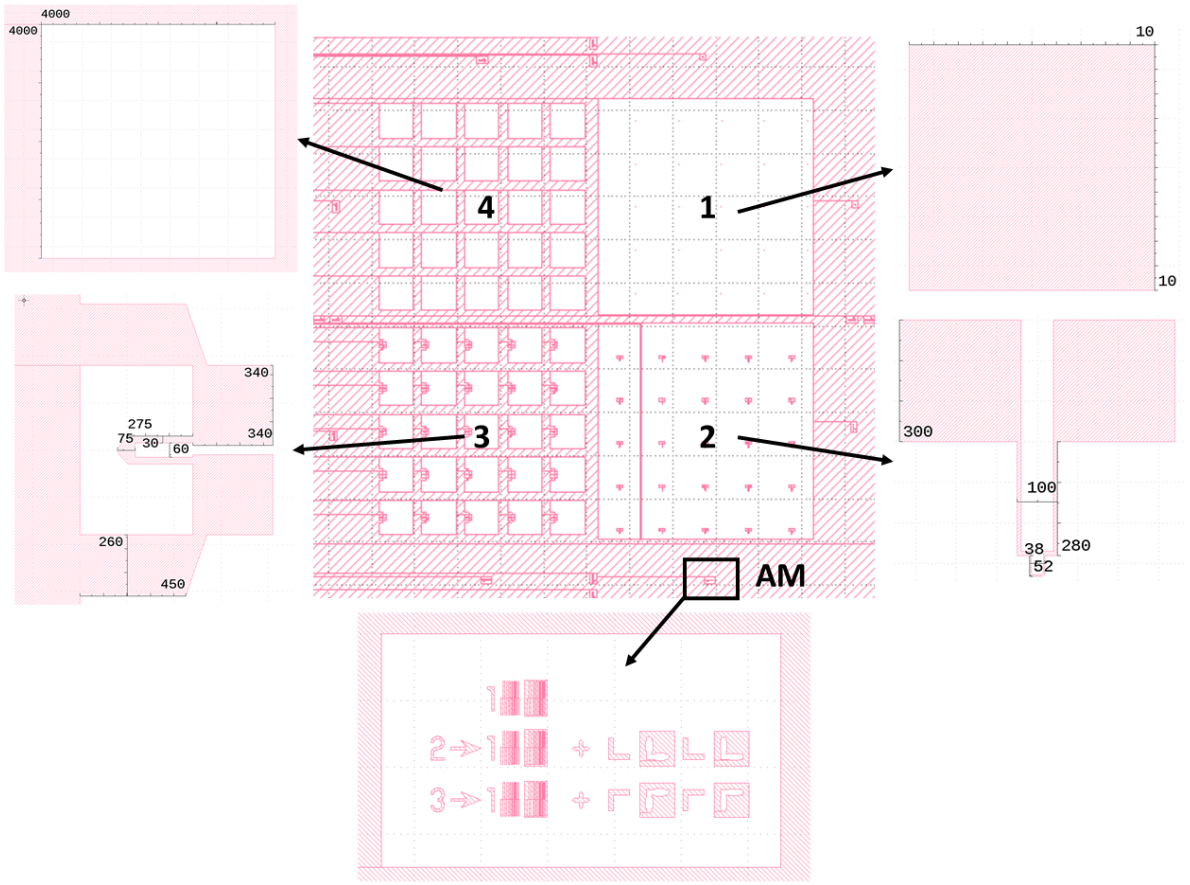

Figure 4.2.1: Overview of the photolithographic mask used. AM stands for alignment marks. The numbers associated with the different quadrants refer to their order in the whole process. Dimensions are indicated in μm.

4.3 Cleaning procedures

Standard cleaning During a standard cleaning the substrates go through a series of 3 baths to remove first all organic compounds from its surface and to etch away the native silicon oxide layer. This first step is achieved by the successive immersion in two baths of piranha solution heated to 120°C for 10 minutes. This solution is made of H_2SO_4:H_2O_2 with a ratio 4:1. The third solution used is a 2% HF solution. The wafers are immersed for 30s to remove the 9Å of natural oxide [86] and replace it with a thermally grown oxide which is more reproducible. The wafers are rinsed between each baths and are finally rinsed in an extra clean bath with continuously flowing water.

This procedure is used on new wafers to prepare them for the thermal oxidation. It is also used to clean wafers from their resist. In particular, it is used after the BHF bath and before the TMAH, as explained at section 4.1. The main reason is that the TMAH solution's etching speed is especially sensitive to organic contaminants [76]. In this context, the HF bath is thus not used.

O_2 plasma A *Tepla 300E* plasma chamber is used to establish an O_2 plasma over the sample. The impact of ions on the surface will detach the organic contaminants that are then pumped away by the system. The working pressure lies around 1mbar. The power is gradually increased in the chamber, from 100W to 500W over a 10 minutes period. The gas exhaust is analysed by the system to allow an estimation of the quantity of organic compounds removed.

This procedure was used after storage time longer than one day as plastifiers and other volatile compounds can degas from the plastic of the storage boxes. These chemicals can then alter the adherence of the photoresists on the substrate's surface.

4.4 Oxide mask definition

Thermal oxidation A thermal oxidation was performed in a furnace *Koyo 1*. Controlled fluxes of H_2O and N_2 are fed into a cylindrical heating chamber. After a pre-heating phase, the wafer is placed for 30min at the temperature of 1000°C. The thickness was checked to be close to 220nm with an ellipsometer.

Dry oxidation was also tested. The *Tempress hydrox 1* was used. Again, a temperature of 1000°C was used with 2L/min of N_2 and 1.5L/min of O_2. The wafers were placed, without pre-heating phase, in the furnace for 4h30. The resulting oxide thicknesses lied around 150nm. Similar results were obtained after BHF etching and since the dry oxidation

time is greater, wet oxidation was preferred.

Oxide mask definition Photolithography on the grown oxide was used to define the mask that will be used during the TMAH attack. First, a degassing in the thermal oven is required. The water that naturally adsorbs and diffuses in the silicon crystal can lower the adherence of the photoresist. A few minutes at 1000°C in the *Tempress* furnace is enough to significantly lower this water concentration. As with any degassing procedure, it follows a decreasing exponential law and it is thus not useful to let the sample longer in the furnace.

The etching of silicon by BHF is isotropic and thus underetches below the photoresist. To avoid the mechanical failure by peeling off of the photoresist's edges, the best adherence possible should be targeted. Thus, an adherence promoter, hexa-methyldisilazane (HMDS), is applied to the surface. N_2 is used as a carrier gas for the HMDS. The mix of gases is fed into a heated chamber (around 100°C) where the wafer is placed, as shown in Figure 4.4.1. The silane groups released, represented in Figure 4.4.1, will react with the oxide surface. the monolayer thus formed will guarantee a better adherence of the photoresist on the surface.

The photoresist (PR), *AZ701*, is then spin-coated onto the wafer at $3000rpm$ for one minute and undergoes a soft bake of $90s$ at $90°C$. This soft bake aims at removing the residual solvent in the film. It is then exposed to UV light, $365nm$, in a *Süss MA6*, a mask aligner. The standard dose of $220mJ/cm^2$ is used. A post-exposure bake is performed at $110°C$ for $90s$. This second bake finalises the photoreaction initiated during exposure by activating catalysts in the film. Finally, the PR is developed in *AZ700MIF* to remove the unpolymerised regions. This is the standard procedure for *AZ701* as described in [87].

The BHF solution's etching speed was calibrated by previous users, it lies around $85nm/min$. The wafer is emerged in the solution to etch away the $220nm$ of thermally grown SiO_2. The oxide thickness is checked with the ellipsometer on large unprotected regions lying on the outer part of the wafer, as can be seen on Figure 4.2.1. Typical values below 1nm were obtained, this corresponds to the limit resolution of the equipment and the etching was thus considered finished. The edges are more exposed to this isotropic etching below the photoresist and will be rounded, as can be seen with optical microscopy in Figure 4.5.2. As TMAH etching is robust against defects in the oxide mask, this won't prove to be a problem for the AFM tips definition.

4.5 AFM tip definition through TMAH etching.

Working principles and experimental parameters Tetramethylammonium hydroxide is a quaternary salt, its cation is constituted of 4 methyl groups on a nitrogen atom.

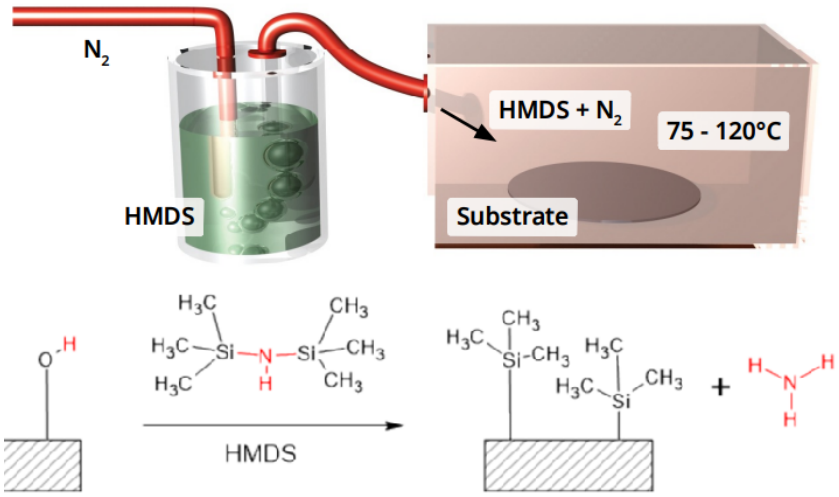

Figure 4.4.1: **Upper part :** Schematic illustration of the equipment required for HMDS deposition. **Lower part :** Surface reaction of HMDS with an oxidised silicon wafer.

Its formula is $N(CH_3)_4^+OH^-$. The chemical mechanism behind the etching of silicon by TMAH relies on the dangling bonds at the interfaces of the silicon crystal. It is thus depending on the crystalline direction of the cut that will define the density of dangling bonds on the corresponding crystalline plane. This results in an highly anisotropic etching. This particularity will be used in this work to reliably define pyramids by protecting local regions from etching.

The main advantage of this methods over more sophisticated approaches, such as the ones used in [83, 88, 89], is that it allows batch processing and that it is protected against minor defects in the mask. In addition, up to certain limits, etching over the oxide cap fall time results in a higher and larger pyramid. As illustrated in the device's description, this dimension is not critical for the design. J. Laconte *et al.* measured selectivities (100)/(111) between 10 and 35, depending on the temperature and concentration [76]. As most reactions, it is activated by higher temperatures but, counter-intuitively, lower concentrations will lead to higher etch rates. Etching with a lower concentrations was shown to lead to lower surface roughness thus a $25wt.\%$ concentration was used as it was the highest available at the host lab and complete data for this concentration in this temperature range were available in [76].

In addition to temperature and concentration, the relative orientation of the oxide cap with respect to the lattice vectors plays a role in the final tip. The effect of misalignment with crystalline direction and of round shapes was studied in this work. The progressive etching starts by complying with the drawing of the cap. As the etching goes on, the faces with the lowest etching rate are favoured and the $< 111 >$ family becomes dominant. The progressive etching of tips with these configurations of caps is presented in Figure 4.5.1.

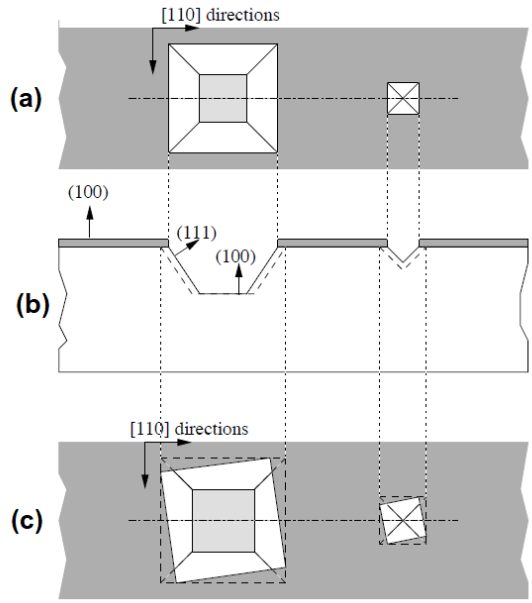

Figure 4.5.1: **(a)** : Etching of Si using a mask aligned with the (111) crystalline family. **(b)** : Cross-section view **(c)** : Etching of Si using a mask misaligned with the (111) crystalline family. Adapted from [76].

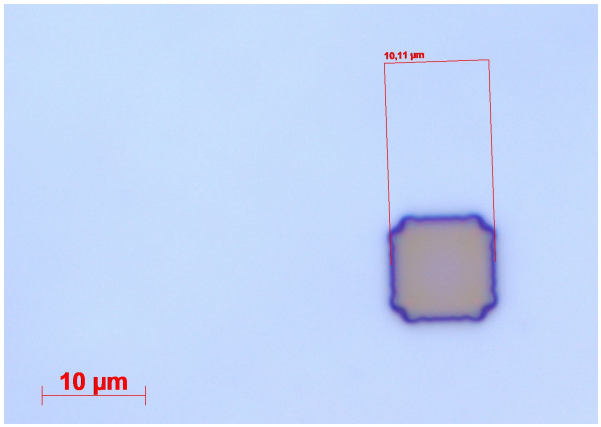

Figure 4.5.2: Oxide cap over a silicon region after the thermal oxidation and the BHF etching.

In the case of a misaligned square cap, this interpretation is easily visible. The square has the normal to its edges in the $< 100 >$ and $< 010 >$ directions, in the horizontal plane. At the beginning, the etching will comply with this orientation. The edges' faces will rapidly break into two directions. The sum of their crystalline vectors yields $< 111 >$ and they merge to form the final shape of the tip, as illustrated in Figure 4.5.1.

Experimental results The anisotropic etching of silicon using TMAH was investigated first using a prototype mask with arrays of different density and sizes of squares. The corresponding dimensions are : $1\mu m$, $2.5\mu m$, $5\mu m$ and $25\mu m$.

The whole etching process of unaligned oxide square caps was imaged using SEM, it can be divided into three distinct periods.

1. Etching along the protected pattern : The etching follows the drawing in the oxide masks. Preferred etching planes progressively distinct themselves and merge. This refers to Figure 4.5.4a. The oxide mask used was made of circles instead of squares to highlight even more this effect but the same phenomenon was observed on unaligned square patterns.

2. Etching independently from the pattern : Once the different low etching rate planes merged into the $< 111 >$ plane. The etching process will proceed independently

from the pattern with all borders at 90° from one another. The oxide cap is still present and the overall shape is thus truncated. The etching progresses below the cap. This step is illustrated in Figure 4.5.4b and Figure 4.5.4c. The clearer regions correspond to the reflection of the electrons on the oxide-silicon interface and thus illustrate the shape of the underlying structure.

3. Etching without the oxide cap : The oxide cap collapsed and fell off the structure. This event could be imaged using SEM and the resulting image is shown in Figure 4.5.5 the etching continues following the same plane family. The final shape is defined as the top becomes sharp. This final step is shown in Figure 4.5.4d. The collapse and detachment of the oxide layer is illustrated step by step in Figure 4.5.6. The same phenomenon was also imaged for AFM tips in Figure 5.3.1. The pattern used is a standard alignment mark with decreasing lateral dimensions and the same etching time.

The etching speed of TMAH was calibrated using a *Veeco Dektak Polyvar* profilometer after different etching times. The results, obtained with series of samples with different etching times and same parameters, are presented in Figure 4.5.3 along with the linear regression used to estimate the etching speed. The results of the thinning step, used at section 4.8 were also included as the same experimental parameters were used. For these samples, since there was no pattern on their surface and since they had a buried oxide layer, ellipsometry was used. The resulting etching rate is 0.256μm min^{-1}.

The samples etched always spent at least a few days exposed to ambient air, it can thus be reasonably assumed a natural oxide layer grew and stabilised around 9Å, as measured in [86]. This layer represents an obstacle to the etching that must first be removed. This could explain the poor fitting of the lowest etching time samples in Figure 4.5.3.

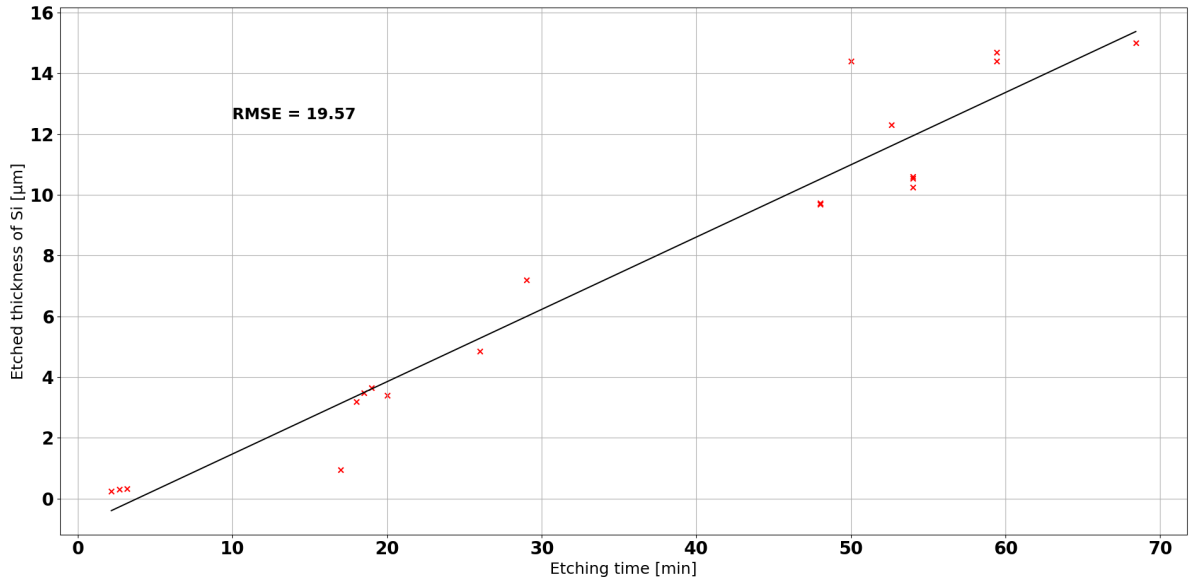

Figure 4.5.3: Different etched thicknesses of Si in TMAH at 25%, 83°C. The linear regression allows to estimate the etching speed to 0.256$\mu m/min$.

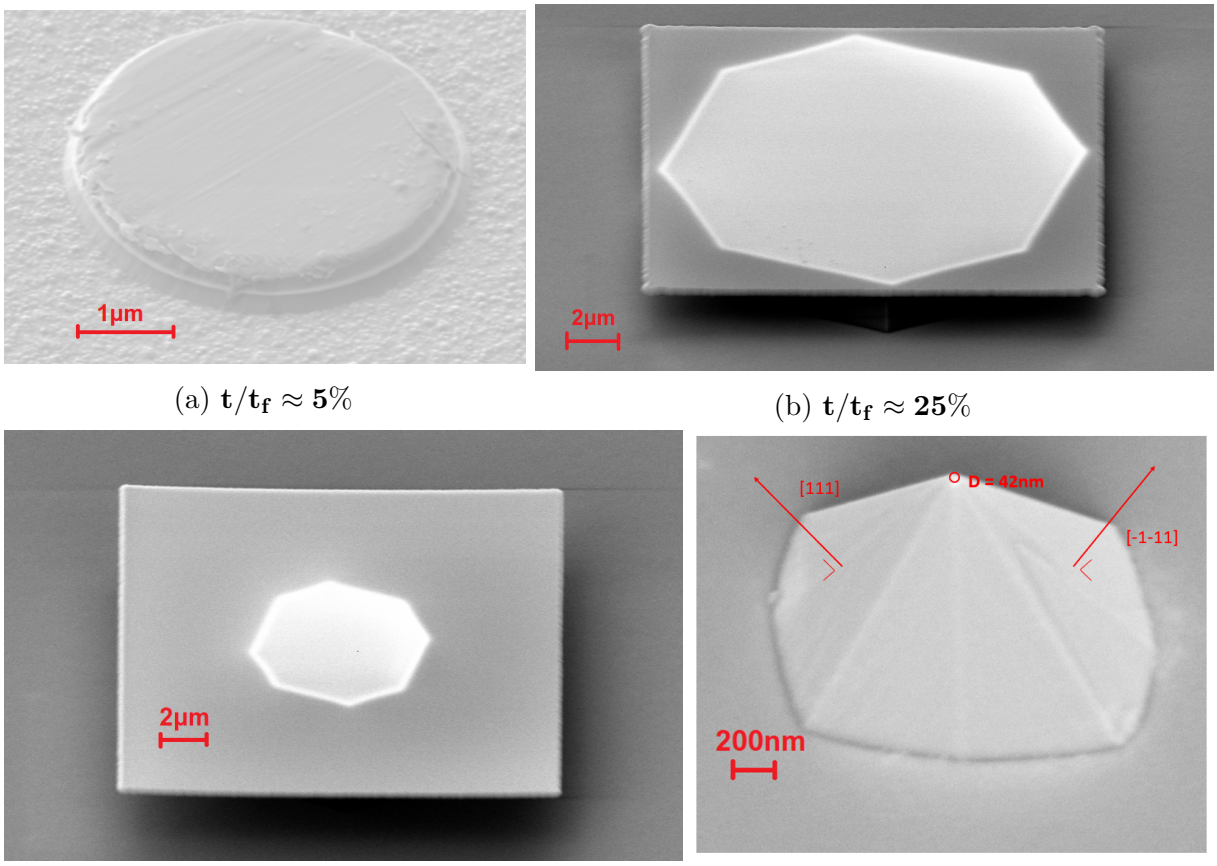

(a) $\mathbf{t/t_f \approx 5\%}$

(b) $\mathbf{t/t_f \approx 25\%}$

(c) $\mathbf{t/t_f \approx 60\%}$

(d) $\mathbf{t/t_f \approx 100\%}$

Figure 4.5.4: SEM image of a SiO_2 pattern over a Si surface after a TMAH attack at 25%, 83°C. The subfigures correspond to different etching times and illustrate the whole TMAH etching process. As they correspond to pattern of different sizes, these times are indicated relatively to the full etching time estimated with the data presented in Figure 4.5.3. The clearer regions correspond to the reflection of electrons at the oxide-silicon interface and thus illustrate the shape of the underlying structure.

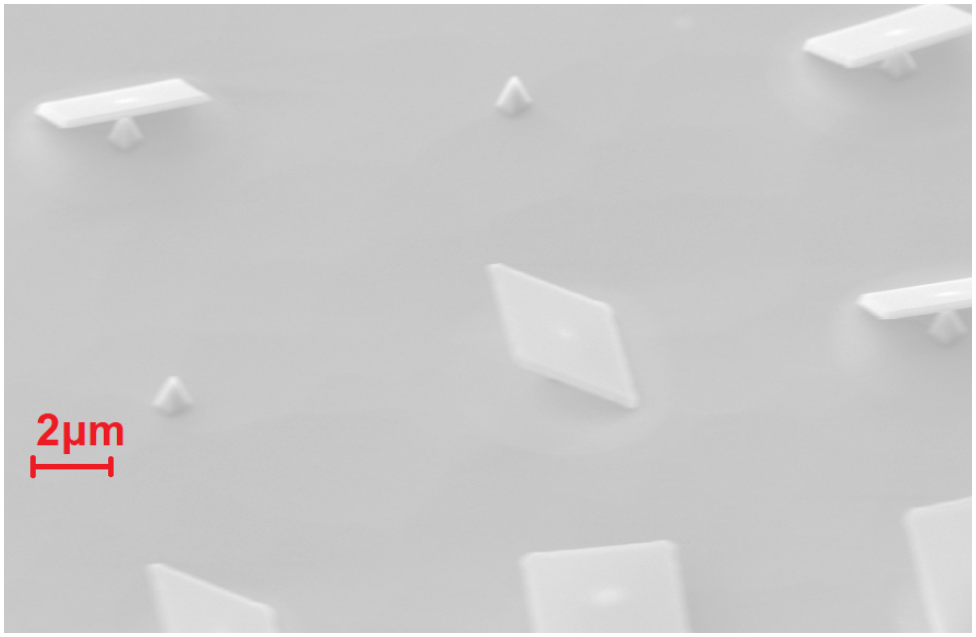

Figure 4.5.5: SEM image of an AFM tips defined in TMAH at the etching time when their oxide cap falls off. Some already lost it, it collapsed on others.

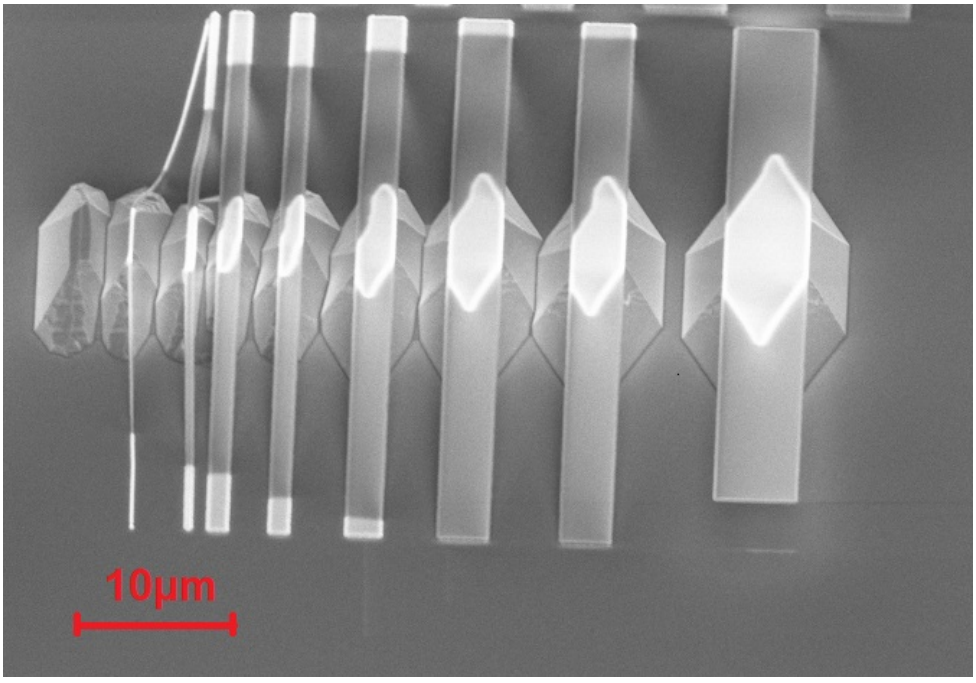

Figure 4.5.6: SEM images of an alignment mark with SiO_2 square patterns of different thicknesses. It illustrates the progressive etching of Si by TMAH, including the collapse and release of the oxide mask.

Homogeneity and bubbling limitations As illustrated in Figure 4.5.7, the etching speed of TMAH is highly dependent on the temperature. The set-up used for the etching, presented in Figure 4.5.8, does not allow for stirring. This induces an important temperature gradient in the beaker and thus a gradient in the etching speed. This gradient was investigated using a series of diced SOI wafers after different times of thinning in the TMAH solution. As the thickness gradient was easily seen with bare eyes, ellipsometry could be performed at regions of different thicknesses, as illustrated at the inset image Figure 4.5.9.

One solution to avoid this gradient is to place the wafers horizontally using a specific flat PTFE holder as illustrated in Figure 4.5.8. As illustrated in Figure A.0.9, the RMSE of these high thicknesses of Si with ellipsometry are significantly greater than the one associated thinner films of photoresists, one example is provided in Figure A.0.6. There thus exists a margin of error for the measurement[1]. Using this set-up, no pattern was seen on the wafer after the TMAH etching and the thicknesses measured at different points on the surface were equal within this margin of error of approximately $\pm 0.5\mu$m.

During the TMAH etching reaction H_2 is released as a side product. The full reaction, reported in [76], can be found at Equation 4.5.1. However, when they are placed in a horizontal position, the bubbles tend to stay at the same place on the surface. It is suspected that this phenomenon creates cavities larger than the expected roughness. This expected RMS roughness was measured to be decreasing from 64Å to 8.8Å going from 5 to 20% concentration at 80°C in [76]. The surface was imaged by optical microscopy and AFM, the results are presented respectively in Figure A.0.5 and 4.5.11. Holes can be clearly distinguished from the roughness of the rest of the surface. These holes are unequally distributed on the surface and their depth lies around $140nm$. In certain regions, these cavities tend to aggregate and form deeper regions, as shown in Figure 4.5.12. Since the gold layer that is used at section 4.6 is only 100nm thick, these holes could cut the electrical contacts.

$$\begin{aligned} (CH_3)_4\,NOH &\Longrightarrow (CH_3)_4\ N^+ + OH^- \\ Si + 2OH^- &\Longrightarrow Si(OH)_2^{2+} + 4e^- \\ Si(OH)_2^{2+} + 4H_2O + 4e^- &\Longrightarrow Si(OH)_6^{2-} + 2H_2 \end{aligned} \tag{4.5.1}$$

The choice of the orientation in the beaker must thus be made based on what is the most critical criterion. In this work, the vertical etching position was used for AFM tip definition. At this step, the relative tilting induced by the gradient of etching speed does

[1]This margin of error corresponds to the difficulty to find the right periodicity for the absorption peaks of Figure A.0.9. As the spectra associated with different thicknesses get closer as the layer gets thicker, the fitting of the experimental curve only finds local minima for the RMSE and the corresponding periodicity thus must be find "by hand".

not impact the following steps while the cavities may eliminate some devices. Oppositely, the horizontal position was chosen for the SOI active layer thinning as sub-micrometer scale defects do not, in first approximation, impact the performance of the silicon as a structural material.

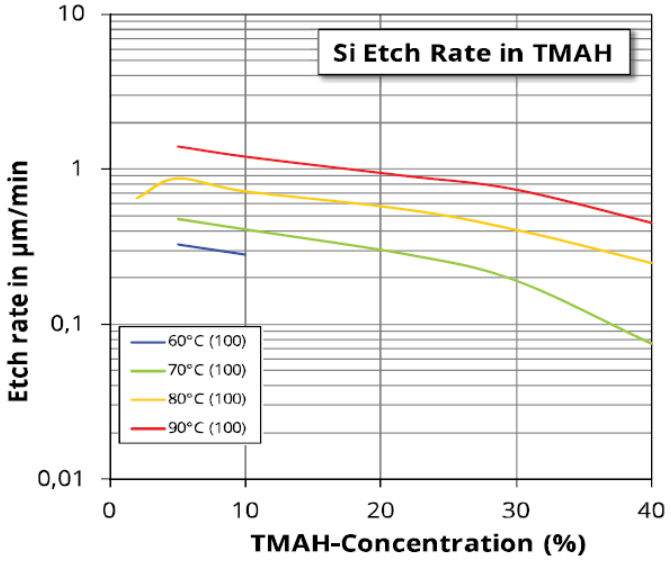

Figure 4.5.7: TMAH ecthing speed of Si at different temperatures and concentrations, extracted from [76].

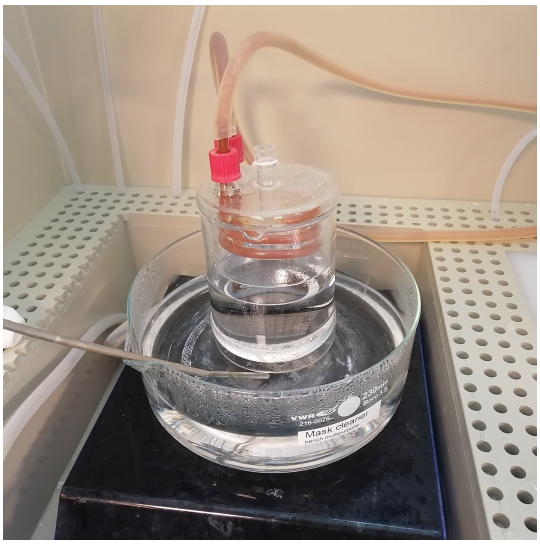

Figure 4.5.8: Experimental set-up for the TMAH etching of silicon. The small beaker contains the TMAH and lies in a *bain-marie*. The wafer is placed on a PTFE holder, here in an horizontal position. A cooling system is used to condensate the TMAH vapours.

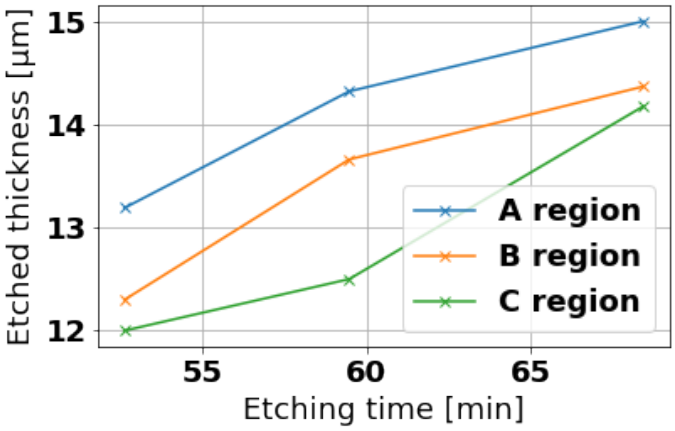

Figure 4.5.9: Different etched thicknesses of samples in horizontal positions. The letters refer to different positions on the dices as denoted on the schematic map on the inset image. The alternating colours on this image refers to the thin film optical effect that can be seen on Figure 4.5.10.

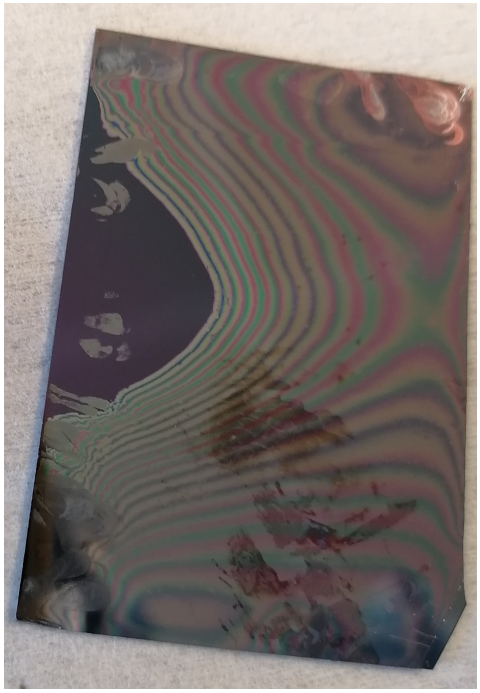

Figure 4.5.10: Visual state of a dice of SOI wafer that underwent a TMAH etching with an important temperature gradient. The colour lines are thin film effect. The dark region is apparent buried oxide layer (BOX).

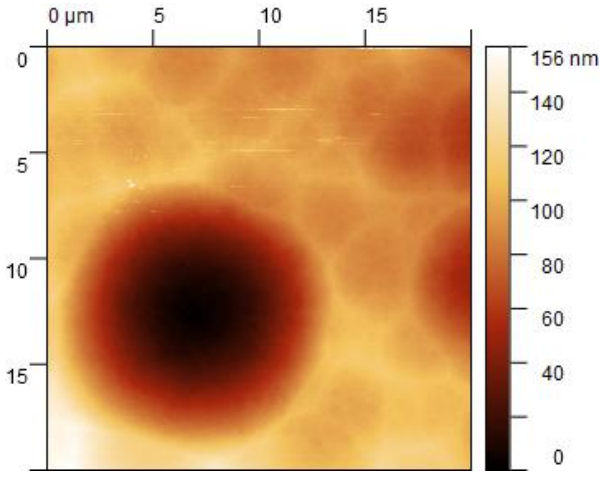

Figure 4.5.11: Isolated crater left by bubbling after 20 minutes in TMAH at 25%, 83°C.

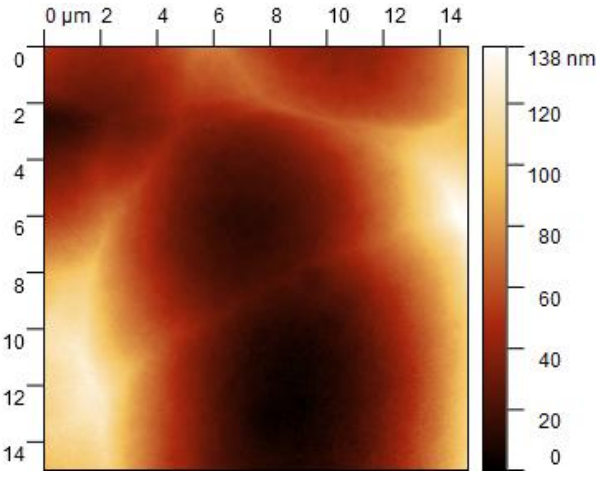

Figure 4.5.12: Aggregate of craters formed by bubbling after 20 minutes in TMAH at 25%, 83°C.

Improved tip aspect ratio The TMAH approach comes with a fundamental limitation, the angle of the pyramid is fixed by the intrinsic structure of the crystal. A high aspect-ratio and sharp tip is important to avoid the widening of high aspect ratio features during a scan. In this work, progresses have been made towards an improvement of this method. A slight oxidation of a few nanometers seems to modify the mechanism of etching. It appears the oxide layer acts as an etching barrier but also modifies the resulting roughness and the slopes of the AFM tips.

The reproducibility of the phenomenon was assessed by using two samples with identical treatments and storage times. Just before the tip definition step, the control wafer was put in a BHF solution for 10s to remove the native oxide layer while not damaging too much the oxide mask. Its integrity was checked afterwards with the optical microscope. They were etched simultaneously in TMAH. The control sample showed pyramidal tips, comparable to Figure 4.5.4d, while the second sample showed this array of tips Figure 4.5.5, a close-up view is provided in Figure 4.5.13.

To improve further these AFM tips, a two-step etching approach was chosen. The oxide masks are defined, the samples are left in storage for two weeks to let the native oxide layer reach its final thickness. The samples are then etched a first time in TMAH. Before the second etching, the native oxide layer is removed and a sturdier base is defined, following the 54.7° angle due to the crystalline structure of Si. This approach allows to define AFM tips with sturdy bases that support a higher aspect ratio upper region, as illustrated in Figure 4.5.14.

These first results need to be explained and further optimised but they rise hope for the development of a cheap, simple technique to obtain sharp tips that could latter be tuned for particular needs. The possibility to define higher tips with this method should be checked to represent a real application potential since commercial tips have height in the tens of micrometers range. In addition, since a high control over the oxide thickness is required, further experiments which aim at optimising the thermal oxide by plasma need to be performed.

Sharpness results Estimations of the sharpness were performed o the two types of tips obtained in this work : the regular 54.7° tips and the ones presenting an improved aspect ratio. The estimation of sharpness for these can be found respectively in Figure 4.5.4d and Figure 4.5.13 and yields diameters of respectively 42 and 31nm. A value of 30nm was also obtained on two stages AFM tips, as in Figure 4.5.14. These are only rough estimations and higher quality images of the apex should be produced for a real measure of the sharpness although the improved aspect ratio tip seems to also present a sharper apex.

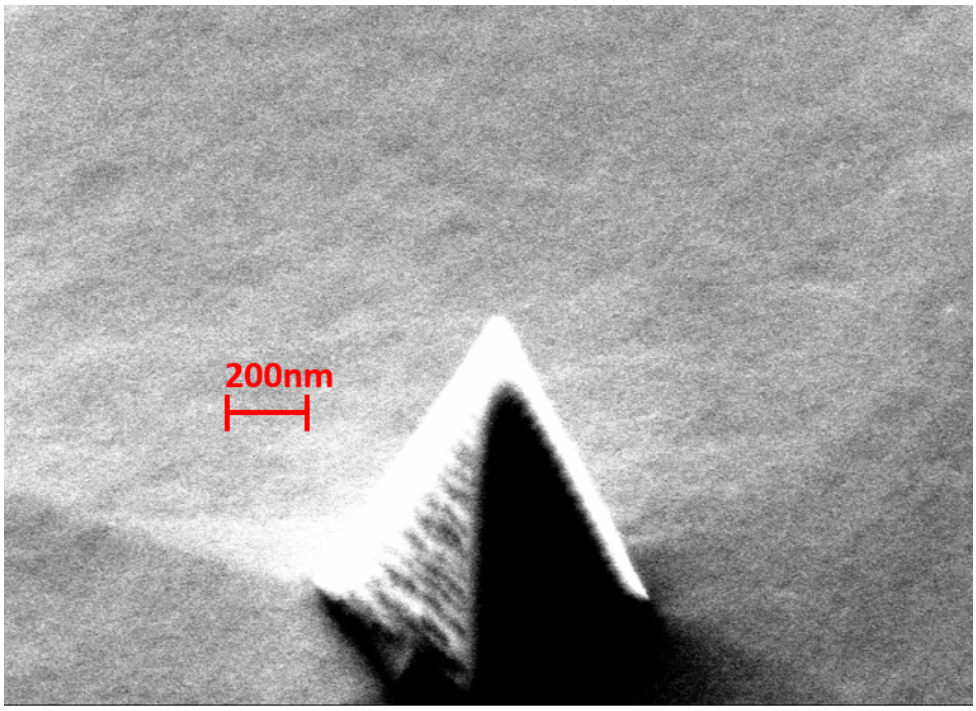

Figure 4.5.13: SEM image of an AFM tip obtained with a single TMAH etching at 83°C, 25% concentration.

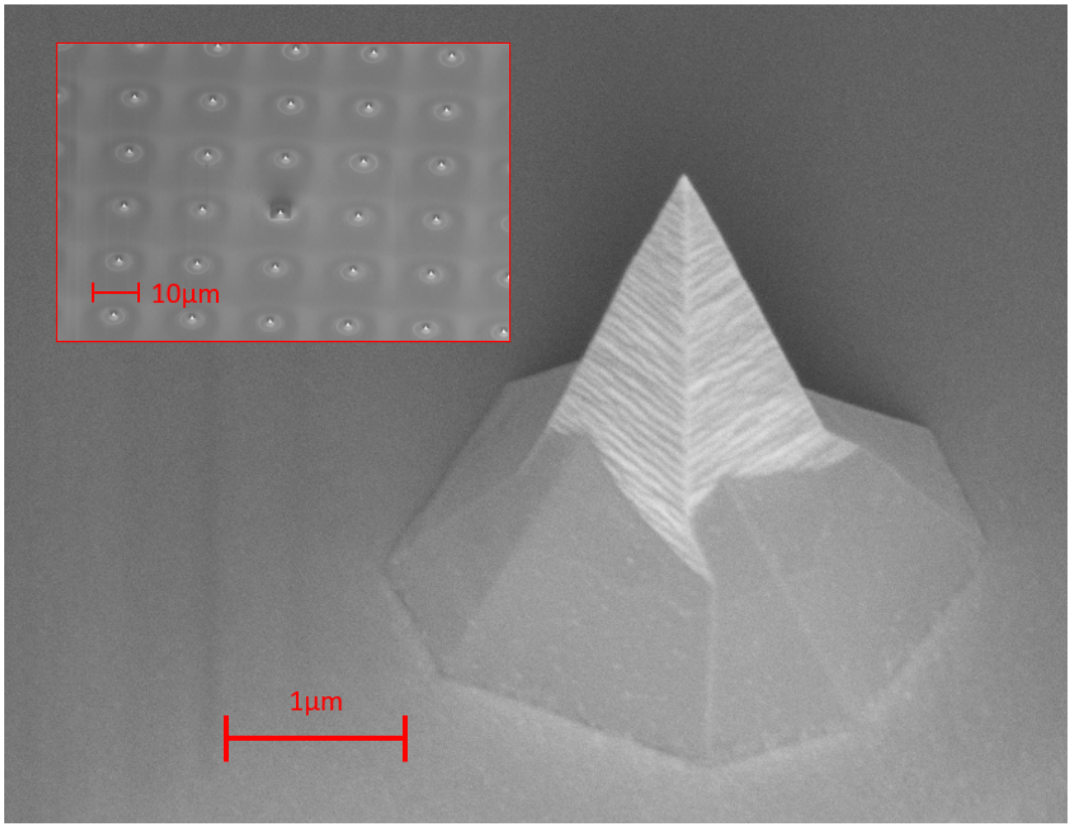

Figure 4.5.14: SEM image of an AFM tip that underwent a two-step etching at 25%, 83°C. The inset image illustrates the neighbouring rows of tips.

4.6 Gold contact definition

4.6.1 Spin-coating over a patterned surface

Usually, spin-coating is realised over surfaces that present features in the hundred of nanometers range. These features sometimes induce shadowing effects and/or inhomogeneities in the film thicknesses. They are generally overlooked as they still allow the proper realisation of the process. Since the AFM tips obtained on these wafers were about 2.0μm high, a lower spin-coating speed was chosen to increase the thickness of the layer. *AZ2020* was chosen as a negative photoresist was required, see section 4.2. It was spin-coated for 1 minute at 2000rpm. The thickness was measured to be around 1.8μm using ellipsometry. The dose applied was 74mJ/cm^2. The patterns were successfully reproduced and no residual film was present. This was verified with an optical microscope and profilometry by removing the resist locally with a scratch, both are presented in Figure A.0.8.

The patterns were defined on two different samples. The first one was a wafer that had undergone the full process with the final mask. Thus alignment was required to place the gold contact on a pre-existing tip. The second wafer had arrays of AFM tips defined with the prototype mask. The patterns were thus directly aligned on a tip array.

4.6.2 Gold evaporation and lift-off

Working principle An ultra high vacuum $p < 10^{-7} mbar$ is applied inside a chamber. One or multiple crucible of materials are placed below a sample holder on which the wafer are placed upside down. Electron guns are aimed at a crucible. The impacts of electrons on the surface heat up the surface and lead to the evaporation of controllable quantities of the material. As the pressure is extremely low, the gas is in the free molecular regime thus the collisions between different molecules of the gas can be neglected. The species thus fly in straight trajectories towards the substrates and deposit there. This set-up allows directional deposition.

Trenches were previously defined by photolithography on the surface of the polymer. These trenches will allow the species to adhere on the surface. During the lift-off, process, vibrations and hot acetone are used to remove the resist. Afterwards, only the material deposited in the trenches will be left on the surface, thus defining the contacts.

Experimental results The gold evaporation was performed in the *E-gun Vacotec*. An adhesion layer of 10nm Cr was first deposited. The working pressure was 8 10^{-7}mbar. A power of 35% was used for the gold evaporation. The deposition rate was measured to be

$0.6Å/s$.

The lift-off of the resin was performed in a sonicator at 37kHz, 30% power and 50°C. This lift-off was successful on the AFM tips region. No AFM tip was observed below the gold film with the final mask, likely due to a problem of alignment since the alignment marks were placed to far away from the patterns. The gold pads were successfully defined on the array of tips defined with the prototyping mask. An optical image can be found in Figure 4.6.1.

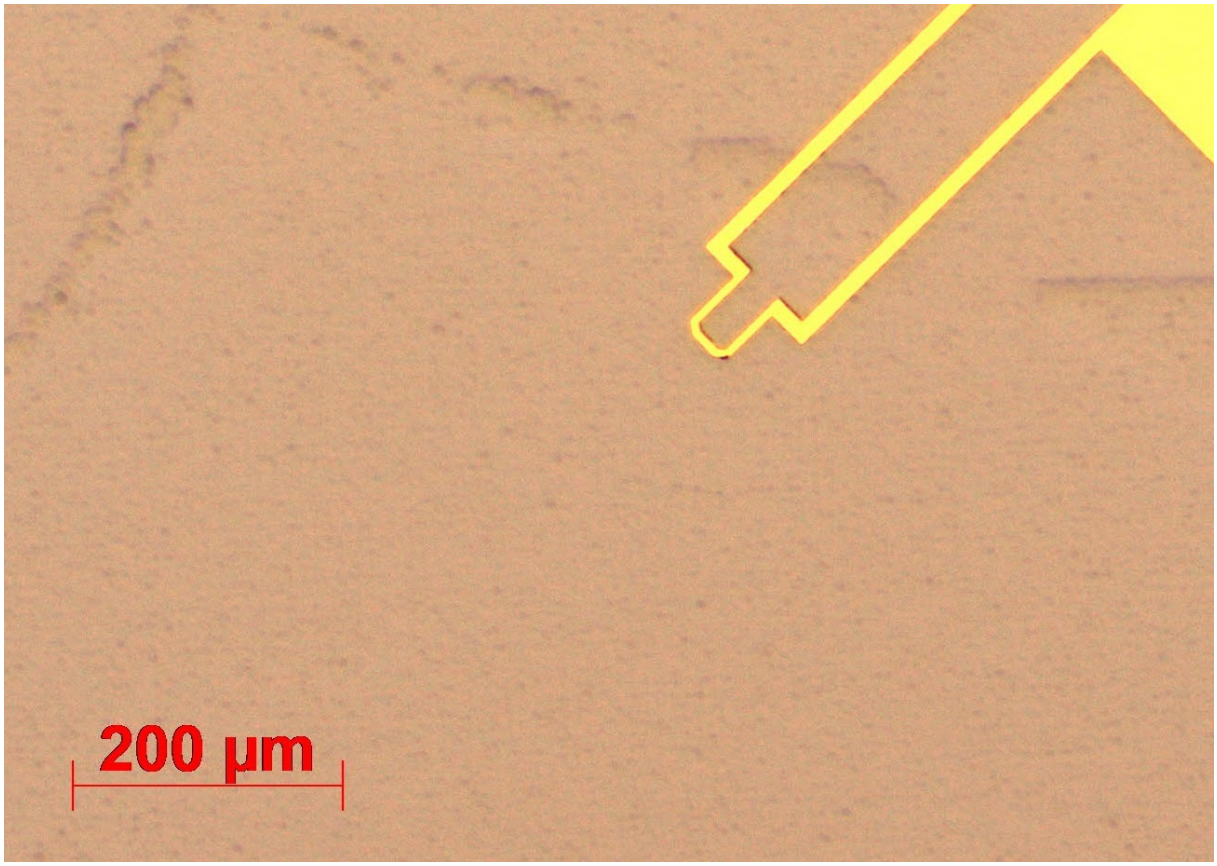

Figure 4.6.1: Gold electrical contacts defined on arrays of AFM tips produced with the prototyping mask.

4.7 Thermistor deposition

In this work, three materials suited for cryogenic thermometry below 100K were investigated : zirconium nitride ZrN_x, platinum and carbon. All were implemented in cryogenic thermometers [57, 59, 60, 62, 90].

4.7.1 First approach : Reactive magnetron RF sputtering of ZrN_y

Reactive sputtering : working principle During a sputtering process, a target made of the material to be deposited is placed in a plasma chamber. The substrate is placed at the other end of the chamber. The pressure inside the chamber must be low enough to avoid electrical breakdown while high enough to allow the plasma to appear. A variety of gases can be used for that purpose but generally Ar is used. Once the plasma is established in the chamber, ions start impacting the target's surface with important kinetic energies, in the order of 500eV. These impacts eject neutral atoms of the target material that will thus deposit on the substrate's surface on the other end of the chamber and form the thin-film. This process is depicted in Figure 4.7.1.

In DC sputtering, the charging effect associated with the ion bombardment can be damaging for the sample as well as disruptive for the process in itself. It is thus only used for electrically conductive substrates. To overcome this limitation, RF sputtering is used, an alternating voltage is applied on the electrode which compensate the charge accumulation by the alternating bombardment of positively charge ions and electrons.

Another evolution of the process is to add a magnet below the target surface. The electrons thus adopt cyclotron-like trajectories that will ease maintaining the plasma. This induces typical circular wear on the targets. In addition, the magnetic field confines the electrons near the target and avoids potential damage on the substrate's surface.

Finally, in a reactive sputtering process, a reactive gas is injected in the chamber in addition to the Ar flux. The energy of the species will induce reactions with the reactive gas at the substrate's surface. This is a complex phenomenon on which many parameters may interplay, as stressed in [91].

Experimental results : Partial covering of AFM tips with spin-coating To selectively deposit a material on the tip, the poor covering of high aspect structures during spin-coating will be used. This partial covering will leave the tip uncovered and when the material is deposited, this region will stay on the tip. This is similar to a lift-off process but with no mask or exposure. It is illustrated in Figure 4.1.1, inset image **(e)**. In this work, this partial spin-coating was performed on the two-stages AFM tips fabricated at section 4.5 with the prototype mask. These probes are about 3μm high.

The first spin-coating results, presented in Figure 4.7.2, suggest that AFM tips can be successfully partially coated thanks to their thin shapes. The two step etching AFM tips, developed at section 4.5 and presented in Figure 4.5.14, were spin-coated with *AZ701* photoresist at 5000rpm to obtain a 791nm thick film. This thickness was obtained with ellipsometry. The related spectrum can be found in Figure A.0.6. The baking steps were

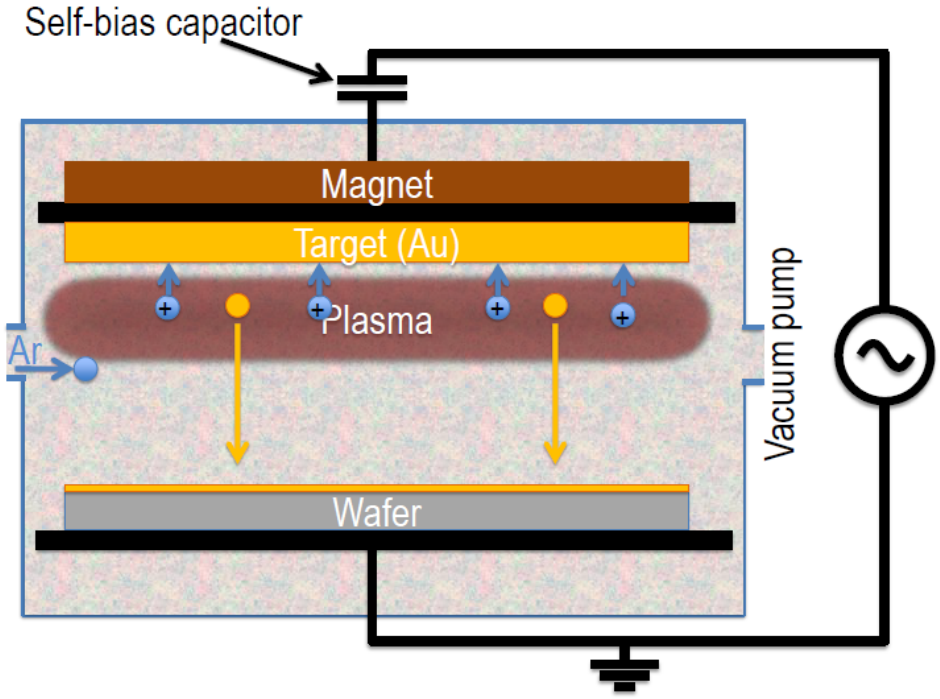

Figure 4.7.1: Schematic representation of the magnetron reactive RF sputtering process.

identical to the process presented at section 4.4.

These samples were observed with an optical microscope and a profilometer scan over the tips were performed. As suggested by the $2.5\mu m$ peaks in the profilometer scan of Figure 4.7.2, the geometry of the tips was clearly distinguishable.

It can be seen that the inhomogeneities in the film's thickness are limited to their direct neighbourhood of tips. No radial drag of the photoresist, or "flying star" effect, was observed. The thickness of the film in the tip's regions could not be differentiated from the one of plane regions. This holds true for patterns that are sufficiently far from one another. As illustrated in Figure A.0.7, denser patterns will induce concentric waves in the resist.

Experimental results : Al deposition over partially covered AFM tips A 50nm thin film of aluminium was deposited the two stages pyramids, defined at section 4.5 and that were previously spin-coated with *AZ701* as explained at the beginning of this Subsection.

SEM images of the AFM tips after the evaporation can be found in Figure 4.7.3. The AFM tips present an aluminium layer over their upper regions. As already suggested by the profilometer scan in Figure 4.7.2 and the SEM image before the lift-off, the AFM tips were sticking out of the photoresin film, as planned. A layer of aluminium can be seen at the top of the AFM tips. Over the 12 tips that were imaged, only one did not show

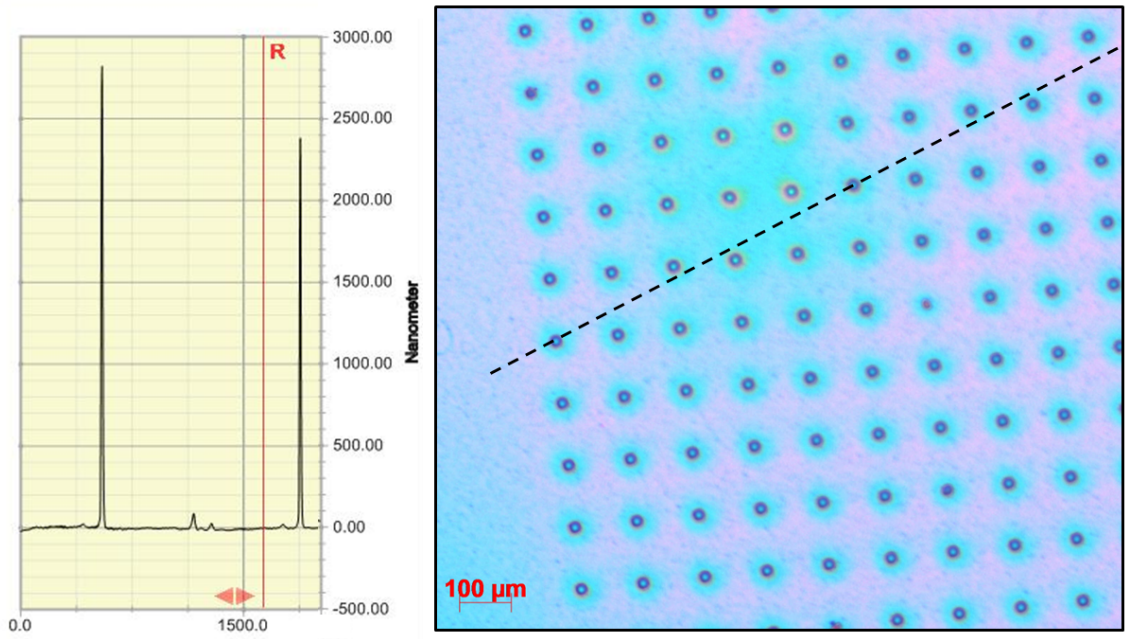

Figure 4.7.2: **Left :** Profilometer scan obtained along the dashed line on the left image. **Right :** Optical image of the AFM tips, presented in Figure 4.5.14, partially covered with *AZ701* photoresist spin-coated at 5000rpm, for a measured thickness of 791nm.

a similar layer. Its apex was broken, as can be seen in Figure A.0.15. This might have happen during the lift-off or prior to it.

The metallisation of AFM tips using a simple spin-coating step was thus demonstrated. This is the first step towards the deposition of a thermistor on an AFM probe. Due to time limitations, the reactive sputtering of ZrN_x spin-coated tips could not be performed. Further investigations will be required to deposit a ZrN_x resistance on AFM tips using this approach.

Experimental results : Properties of ZrN_x thin films Thin films of ZrN_x were deposited on plain Si wafers for characterisation by Yubin Huang (NAPS). A series of samples with different N_2 pressures were fabricated. The deposition parameters can be found at Table 4.1. The thicknesses indicated were obtained by Pr. Merckling (IMEC) using XRR, the associated spectra can be found in Figure A.0.14. The substrate temperature is considered to be ambient. The deposited films were analysed by Pierre Eloy (BSMA) using X-ray photoelectron spectroscopy to determine their composition.

As demonstrated in [57], the resistivity of ZrN depends heavily on its stoechiometry. It was shown that only disordered ZrN_x films showed the negative temperature resistance coefficient that is desired for cryogenic thermometry.

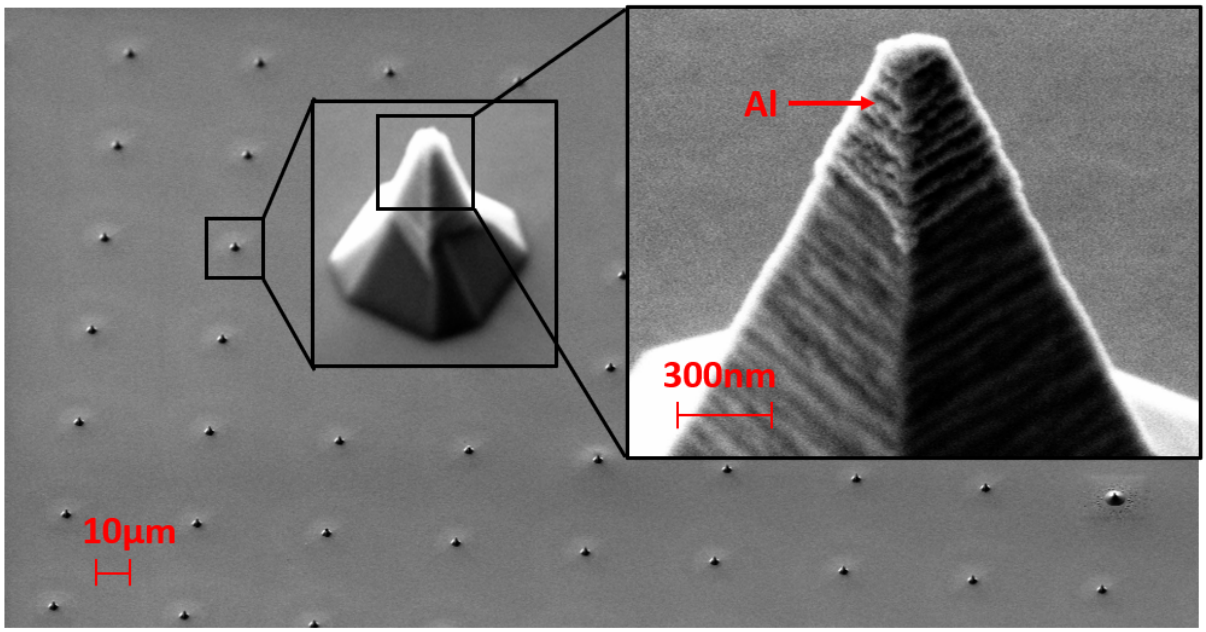

Figure 4.7.3: SEM images of two stages AFM tips, defined in Figure 4.5.14. The aluminium thin film was deposited using a lift-off process.

	Power [W]	Pressure [mTorr]	Ar [sccm]	N_2 [sccm]	Thickness [nm]
A	100	3	25	0	190
B	100	3	21	4	85
C	100	3	19	8	54

Table 4.1: Experimental parameters used for the reactive rf sputtering of different sets of ZrN samples. The thicknesses were determined afterwards using the X-ray reflectivity data presented at Figure A

X-ray photoelectron spectroscopy (XPS) : Composition The XPS technique relies on the analysis of the photoelectron extracted from a surface under a X-ray radiation. The energy balance of the phenomenon is written as follows :

$$\hbar\omega = K_{el} + \phi \tag{4.7.1}$$

where K_{el} is the kinetic energy of the electrons extracted, ω is the frequency of the incident light. ϕ is called the extraction potential. It is the energy required to extract the electron from its orbital. It depends primarily on the atom's structure but also on its chemical environment and bonds. K_{el} is measured with an energy analyser. Knowing the wavelength of the incoming light allows to estimate ϕ and thus deduce the nature of the atom as well as its chemical bonds.

In practice, X-rays are generated by the bombardment of Al or Mg targets by electrons. The *Bremsstrahlung*, induced by the deceleration of a charged particle in a material, emits X-ray spectrum. After going through a monochromator, the beam is focused on a region of

the sample. The electrons emitted by the photoelectric effect are extracted and accelerated before entering an energy analyser. Thus, the lower the kinetic energy of the extracted electron, the higher its binding energy which can be linked to the atom's species. In addition to this analysis set-up, in modern installations an ion beam is also focused on the surface to allow in-depth profiling, as was done here.

Two graphs are presented for each sample. First, the atomic concentration of the different kinds of atoms in the thin films are presented with respect to the depth in Figure 4.7.5. The chemical state of the Zr in the thin films is then presented, again as an in-depth profile, in Figure 4.7.6. The data were normalised to 100%.

As can be seen on Figure 4.7.5, a carbonaceous contamination is present at the top surface. In addition, the concentration in O rises at the surface. In fact, this results from the partial oxidation of Zr at the surface as can be seen in the curve of ZrO_2 in Figure 4.7.6. It is also possible that this signal is associated to the presence of oxinitride. Apart from these surface contaminant, the sample A is made mostly of metallic Zr. It is interesting to note that, even though the flux of N_2 is double for the sample C with respect to sample B, they share a very comparable spectrum with a majority of stoechiometric ZrN.

The difference between sample B and C is the atomic concentration of N which is slightlyhigher in the latter. This is illustrated in Figure 4.7.4. The ratio of atomic concentrations of ZrN/N is overall greater in the sample C but still around 1 which indicates that the N is mostly present in ZrN. The regions where this ratio goes over 1 indicates regions where more complicated species such as oxinitride or organic contamination are present.

In conclusion, the thin films deposited were made of metallic Zr for the sample A and mostly metallic ZrN for the samples B and C. The partial pressures of the gases cannot be directly related to the stoechiometry of the deposited films. The amorphous ZrN_x thin films highlighted in [57] were thus not obtained and further investigations will be required to deposit them.

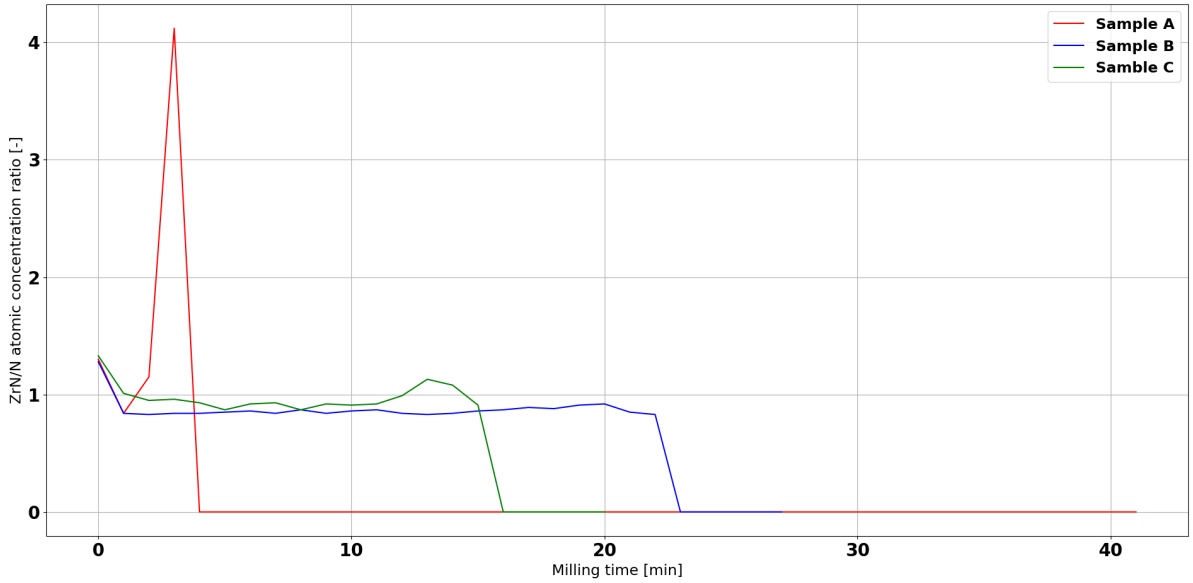

Figure 4.7.4: Relative atomic concentrations of three chemical states of Zr in reactively sputtered ZrN thin films. The data were obtained by XPS and normalised to 100%.

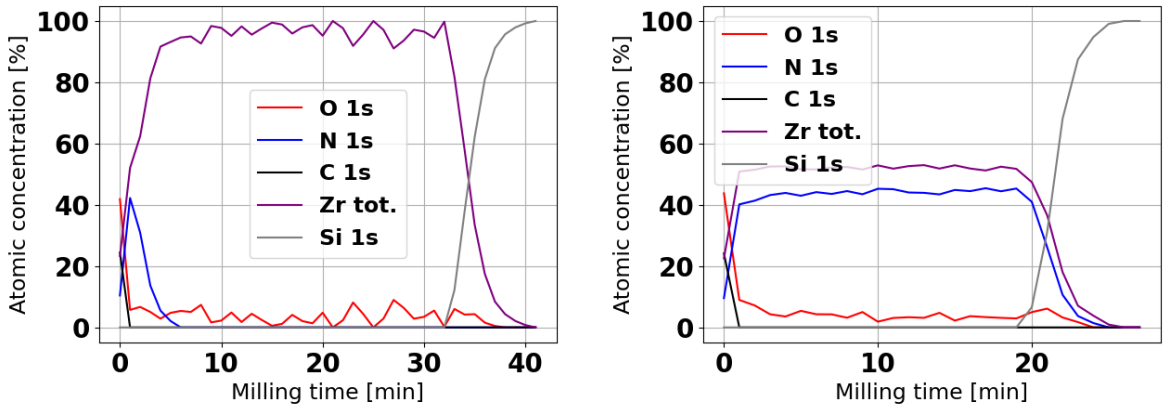

(a) Sample A

(b) Sample B

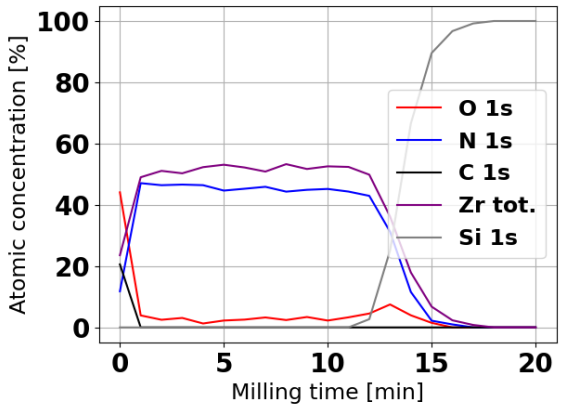

(c) Sample C

Figure 4.7.5: Relative atomic concentrations, obtained by XPS, of three different ZrN reactively sputtered thin films. The deposition parameters can be found at Table 4.1.

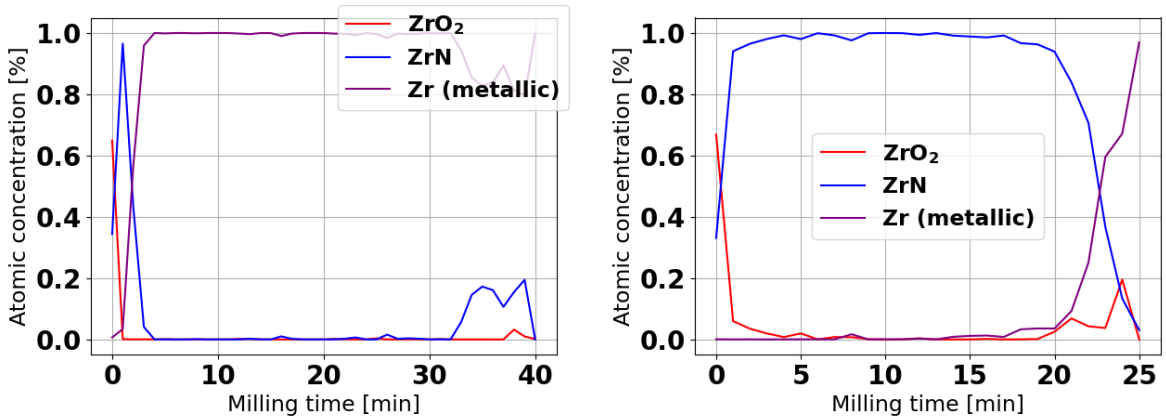

(a) Sample A

(b) Sample B

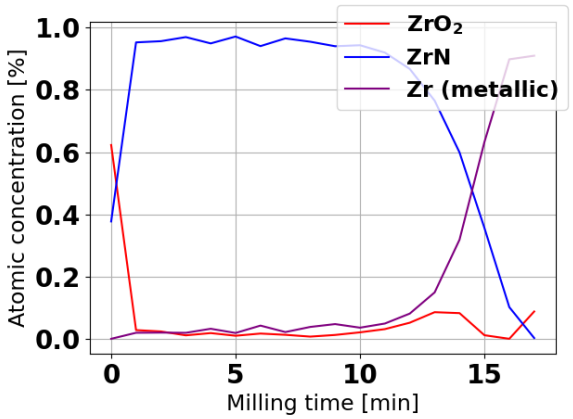

(c) Sample C

Figure 4.7.6: Relative atomic concentrations, obtained by XPS, of three different chemical state of Zr in three ZrN reactively sputtered thin films. The deposition parameters can be found at Table 4.1.

4.7.2 Second approach : Focused ion beam induced deposition (FIBID)

Working principle During a focused ion beam induced deposition (FIBID), a local micro-needle injects a precursor gas that decomposes under the ion beam and deposits a film of a given material. In this work, FIBID was used with a gallium ion beam to deposit C and Pt with phenantrene $C_{14}H_{10}$ and $(CH_3)_3Pt(CpCH_3)$) respectively. Cp stands for cyclopentadienyl complex which is a coordination complex. [92, 93]

FIBID presents advantages compared to other deposition methods such as electron beam lithography (EBL). FIBID has a high current density, allows a very fine focusing of the beam due to the higher mass of ions, has a higher energy density and a shorter penetration depth in solids. It also offers a maskless process oppositely to other processes relying on EBL [94]. Since it does not rely on a mask, FIBID is especially useful to deposit thin films on non-planar surfaces as they cannot be well spin-coated. This property could be used to deposit thin films directly on AFM tips.

Temperature dependent resistivity in C and Pt films First, C and Pt films were deposited on available two-terminals devices with pairs of gold fingers, with the help of Sébastien Faniel (Winfab). The lateral and vertical dimensions of the deposited films were determined with a commercial AFM set-up (*Bruker Icon Dimension*, available through the MICA platform) and confirmed by SEM images. The resulting scans of the commercial AFM are available Figure A.0.16, A.0.17, A.0.18 and A.0.19.

The substrate used for the FIB induced depositions was fixated on a chip and the gold pads were wirebonded on its different pins. This chip was placed on a chuck. This holder is thermally anchored to the cold head of a *Montana Instrument Cryostation*, through a specifically designed basis. The whole structure is placed inside a vacuum chamber made of three steel pieces hermetically sealed by joints. The holder is electrically connected to the outside by thermally anchored cables. The inside of this chamber is represented in Figure A.0.13. The cold head is cooled through the adiabatic expansion of a He gas. This type of set-up can go down to 3K according to the manufacturer. [95]

To monitor the temperature of the chamber, a *PT1000* platinum resistance was thermally anchored and connected to the sample holder's chuck. This kind of thermometer is suited for measurements down to 200K only. The resistance measurements are performed through a series of thermally anchored cables by two *MFLI* lock-in amplifiers from *Zürich Instruments*.

Using the dimensions mentioned at Table 4.2, the resistivity curve is obtained and is is presented in Figure 4.7.7. The order of magnitude is coherent for an amorphous carbon

film. The value of 1mΩ m at ambient temperature can be found in [96]. However, the variation of resistivity with the temperature is drastically lower compared to the $T^{-1/4}$ law suggested in [96,97]. In addition, the apparent saturation at lower temperatures is not coherent with the resistivity evolution of a ceramic.

The full discussion about this measurement can be found at Figure A. The sample was probably burnt through the measuring process and thus the resistivity curve obtained in Figure 4.7.7 is not exploitable. The contact was very likely only capacitive. This could explain the very low resistivity variation over the range as well as the unexpected saturation at low temperatures. Optical and SEM images of the film after measurement can be found in Figure A.0.20.

		Pt 1	**Pt 2**	**C 1**	**C 2**
Deposition parameters					
Deposition method		FIB	FEB	FIB	FIB
Acceleration voltage [kV]		30	20	30	30
Deposition current [pA]		240	120	120	120
Deposition time [min]		2	6	3	3
Dimensions					
Thickness [nm]	C	120	32	51	42
L_x ($\parallel \vec{E}$) [μm]	C	2.0	5.0	7.5	10.0
	SEM				
L_y ($\perp \vec{E}$) [μm]	C	10.4	8.0	14.8	7.6
	SEM				

Table 4.2: Dimensions and deposition parameters of C and Pt thin films deposited using FIBID and FEBID. H corresponds to the homebuilt AFM set-up, C to the commercial one and SEM to the SEM images. L_x and L_y make reference to the dimensions perpendicular and parallel to the current, respectively. In particular L_x refers to the distance between the electrodes and not the film's dimension. The corresponding AFM images can be found at Figure A

4.8 Definition of the cantilevers and anchors

4.8.1 Cantilever definition by photolithography

Due to the plasma required for the Bosch process, it yields a poor selectively for photoresists, below 10 usually, thus using a thick photoresist as *AZ9260* is the common procedure.

Due to the high viscosity of *AZ9260*, this positive photoresist is first spin-coated, slowly, around 300rpm, to ensure that the resist covers the all surface. Without this step, the

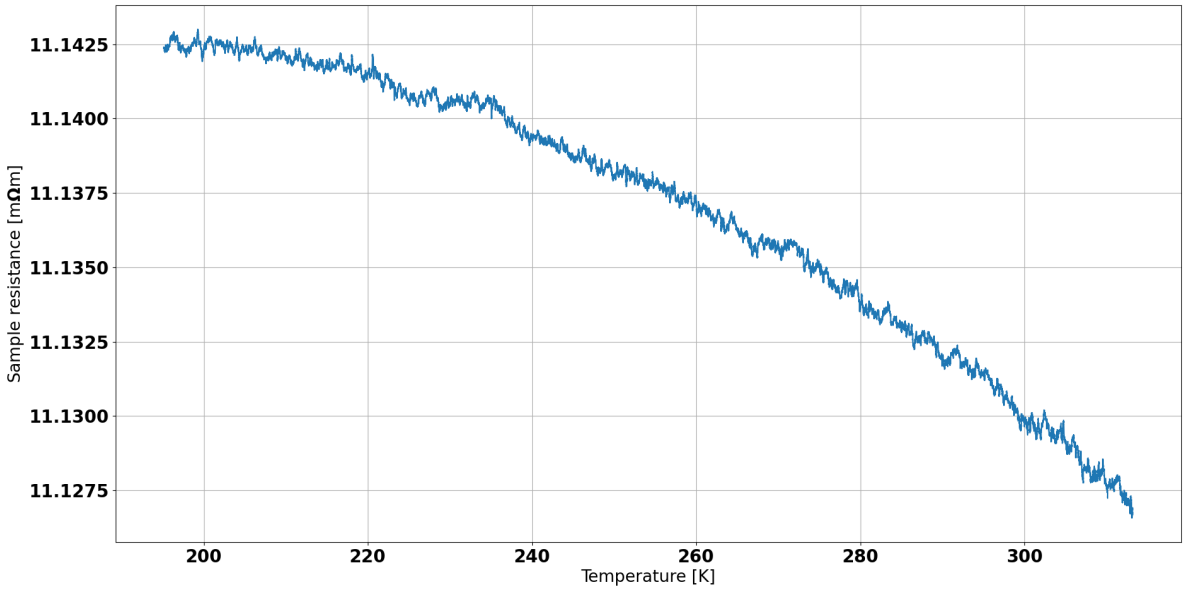

Figure 4.7.7: Resistivity temperature dependence of an amorphous carbon thin film deposited using FIBID.

photoresist forms radial flows and leaves the substrate, as illustrated in Figure A.0.11. This first step depends on the surface to cover, the adhesion to the surface and the quantity of resin used. The second spin-coating, at 1500rpm, supposedly defines the final thickness but it was observed that the latter also depends on the first spin-coating process.

Once spin-coated, the wafers undergo 2 consecutive baking, one at 105°C for 2 minutes and at 125°C for 15 minutes. Once it has been baked, the wafers are placed in a wet atmosphere overnight to allow the resin to rehydrate, as illustrated in Figure A.0.10. This step is very quick for thin resists. For thick resists, a split exposure is used. Exposure periods of 5 seconds are alternated with rest periods to let the gases formed outgas of the film. A total exposition time of 41.7s is used for a total dose of $200mJ/cm^2$. No PEB is required with this resin.

Since the control of the thickness was not properly achieved and that no thickness measurement could be performed on freshly spin-coated samples, the dose of the exposure could not be adapted to the film's thickness. This resulted in an underdevelopment. A residual film was still present in the trenches. It was measured to be 2.3μm thick while the thicker regions yielded 5μm. This was confirmed by optical microscopy and profilometry as can be seen in Figure 4.8.1.

This underdevelopment could also have been due to an insufficient time in the developer. This is usually not a problem for thin resists where development times lie around 1 minute but for *AZ9620*, it is comprised between 15 and 30 minutes. The precise time depends on the pattern size, according to a pre-existing recipe in the host laboratory.

Resin stripping effects were observed for development times over 30 minutes, as illustrated in Figure A.0.12. Further experimentation with different spin-coating programs and UV doses will be required to fully master this process.

Small bubbles can also be seen on the surfaces, as can be seen in Figure 4.8.1. They could be due to soft bake with a too high temperature or have been caused by the UV dose during the exposure. This could be improved by increasing the soft bake duration or increasing the time between exposure periods. Overall they do not jeopardise the next steps and their relative rarity proves that this aspect of the process is overall mastered.

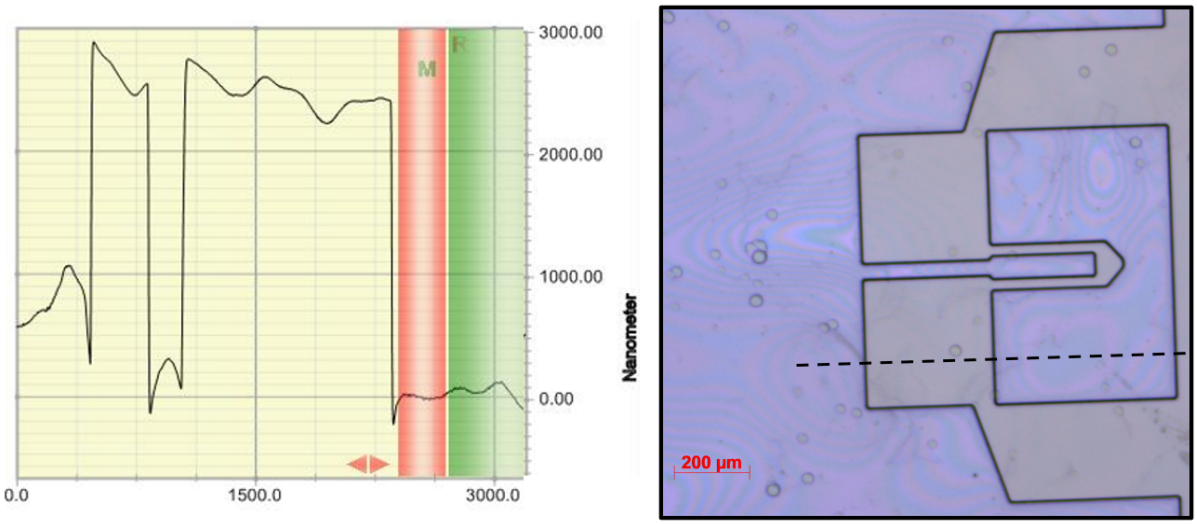

Figure 4.8.1: Profilometer scan through cantilever's patterns defined in *AZ9260*. the line along which the scan was made is presented with dotted line on the optical image on the right.

4.8.2 Deep reactive etching (DRIE) using the Bosch process

Working principle The Bosch process is a sequential process that alternates between isotropic etching and passivation phases to obtain vertical sidewalls in Si. Both phases use plasma to activate species that will react on the surface. In the etching phase, SF_6 is fed in the chamber and, when activated, it is able to etch isotropically and fast the Si. The passivation phase uses C_4F_8 that will form a layer of polytetrafluoroethylene (PTFE) on every surfaces. Since this layer is best removed with the mechanical impact of species on the surface and since these impacts happen mostly perpendicularly to the surface due to the plasma, the vertical sidewalls are protected against etching. This etching approach allows to form extremely high aspect ration structures in silicon. This process will be used to define the cantilevers on the active face of the SOI wafer.

Aluminium is commonly used as mask for the Bosch process but, the thick positive

photoresist *AZ9260* was chosen as a mask for its reduced number of deposition steps.

Experimental results As the only SOI wafers available had a $15\mu m$ thick active Si layer, a prior thinning step was required to get closer to the aimed thickness of 3μm that was computed in section 3.5. Although, it was decided to use a thicker silicon film for the first experiments with the Bosch process since it could attack quickly the silicon if the photoresist was removed faster than expected.

The thinning was performed using a 25% concentrated TMAH solution at 83°C. The horizontal position was used to limit inhomogeneities, as explained in details at section 4.5. The resulting thickness was measured to lie around 5.2μm with an ellipsometer. The corresponding Δ and Ψ spectra are presented in Figure A.0.9. The local error and RMSE are significantly greater than what is obtained for common ellipsometry fitting, such as the one presented in Figure A.0.6 in subsection 4.7.1. 5μm is close to the maximum thickness that can be observed with this instrument. It is estimated that an error margin of $\pm 0.5\mu$m is reasonable.

In this work, a *Oxford Plasmalab ICP-RIE* was used to define the patterns of the cantilevers in the thinned SOI wafer using the Bosch process. Cycles of 13 and 10s were used for etching and PTFE coating respectively. A flux of 120sccm of SF_6 was used for etching and 150sccm of C_4F_8 for the deposition. At first a 10 sccm oxygen flux was added to the etching cycles as it increases the anisotropy and etching speed of photoresist thus improving the removal of the residual films. The progression of the etching was measured regularly with an ellipsometer. Once the *AZ9260* residual film on the bottom of the trenches was removed, the same parameters were kept with no O_2 flux. Overall, 40 cycles with O_2 and 25 without were applied.

The final etched thickness were assessed using profilometry, SEM imaging and ellipsometry. For profilometry and SEM, the corresponding results are both presented in Figure 4.8.2. The difference of height that can be seen on the profilometer scan are compatible with the thickness of the silicon layer measured after thinning. The ellipsometer spectrum could not be fitted with a RMSE below 15 and a fitting respecting the spectrum's periodicity. The roughness of the surface, that can be seen in Figure 4.8.2, requires a more complicated treatment of the spectrum, as stressed in [98].

The release and the measurement of the resonance frequency of the cantilevers would be required to assess if the important roughness induced by the Bosch process modifies the resonance frequency predicted by the finite element simulations presented at section 3.5.

To avoid residual layers, further experiments to control the thickness and the development of *AZ9260* will be required to properly defined Akiyama cantilevers on a SOI

wafer. Two alternatives are envisioned to overcome the difficulties associated with the use of thick resists. *AZ701* could be used as it has a selectivity around 10, according to other works performed in the host laboratory. This resist could thus be used for thinner depths to be etched. Otherwise, aluminium masks are also used and offer an excellent selectivity although they require more time-consuming deposition means than spin-coating.

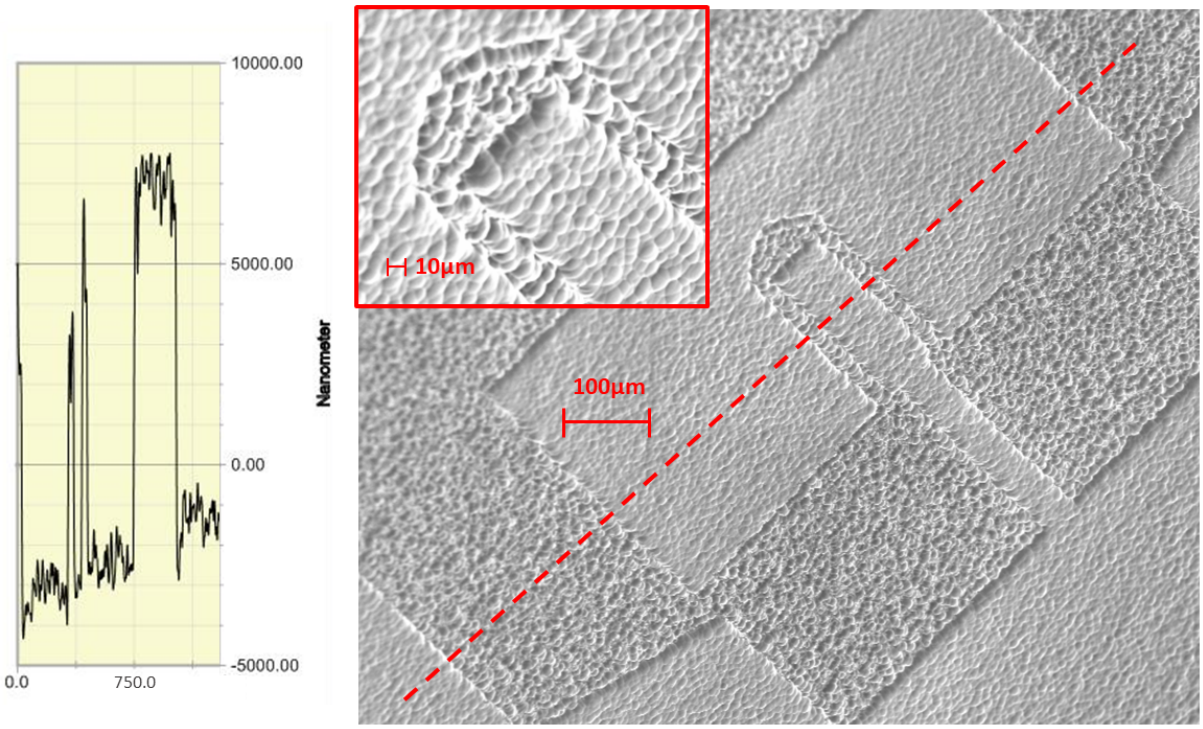

Figure 4.8.2: **Left :** Profilometer scan along the dashed line presented **Right :** SEM image of cantilevers and pads defined with the Bosch process using an *AZ9260* mask. The image was taken after the removal of the photoresist. A zoom on the tip's holder (with no tip) is presented as an inset image.

Chapter 5

Setting up a homebuilt tabletop atomic force microscope

5.1 Overview presentation

The designed and built AFM set-up for an Akiyama probe self-sensing scheme is schematically presented at Figure 5.1.1. The set-up comprises two independent electrical circuits. The first is constituted of a manually controlled *ANC300 Piezocontroller* from *Attocube*. It allows to generate a "sawtooth" signal and to choose its amplitude to control the progressive vertical elongation of the *ANPz51* piezomotor. This motor allows incremental movement of $200nm$ in a range of $2.5mm$. This motor is controlled manually so far, as illustrated by the switch on Figure 5.1.1.

The second electrical circuit implements the feedback loop based on the amplitude of vibration as well as the scanning through the lateral bending of the piezotube. The signal from the tuning fork is amplified with a current amplifier, fed into the lock-in amplifier that extracts its phase and amplitude. These values are transferred to the *GXSM3* software that manages the feedback loop. The amplitude is then compared to the setpoint. This setpoint is chosen below the free oscillation amplitude to ensure that the tip stays in close proximity with the surface, as explained at subsection 2.1.1. The feedback loop determines the response to apply on the piezotube to minimise the error signal. Finally, the corresponding voltage passes through the voltage amplifier before being fed to the piezoelectric element. The piezotube thus expands or retracts and the vertical position z is corrected. The piezotube used is a *TB3507* from *Piezodrive*, it can be seen in Figure 5.2.1. It has a vertical range of $7.4\mu m$ and a scan range of $39\mu m$.

The whole set-up is mounted on a stage with 3 micrometric screws for coarse positioning in three dimensions, as illustrated at Figure A.0.22. They allow to perform the horizontal positioning as well as a rough vertical approach using an optical microscope focused on the tip from the side. In short, the approach is made in two steps, first with a micrometric screw, then with the piezomotor by monitoring the feedback response. The approach is

manually performed by choosing a setpoint below the free oscillating value. This results in the full extension of the piezoelectric tube. The coarse approach is performed by manually controlling the piezomotor. Once the surface is reached, the tube will retract progressively.

Topography reading As explained in section 2.3, the capacitance associated with the tuning fork is dynamically measured through a lock-in amplifier incorporated in the *Soft dB controller*. The amplitude of vibration is proportional to this value which allows to use an amplitude based feedback.

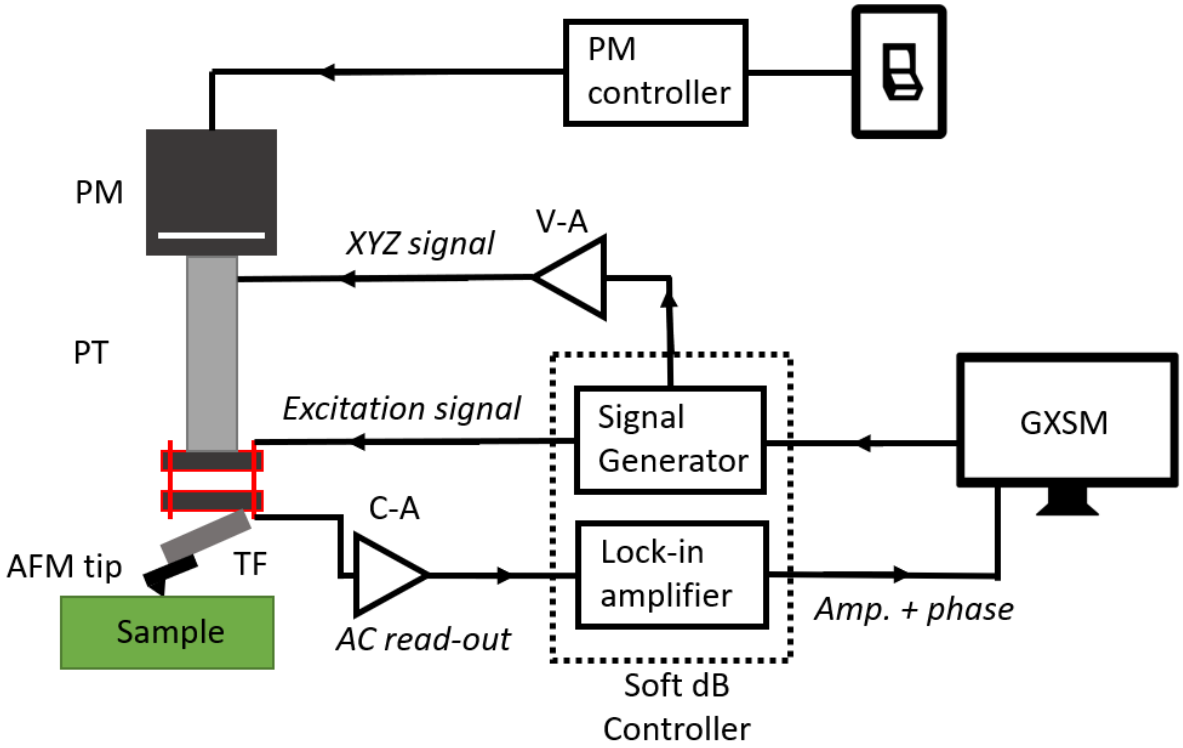

Figure 5.1.1: Schematic drawing of the AFM set-up designed and built. PM stands for piezomotor, V-A for voltage amplifier. PT denotes the piezotube, C-A the current amplifier. TF stands for tuning fork. The description of the different signal are written in italic. The dashed lines indicate that both the signal generator and the lock-in amplifier are included in a single device.

5.2 Mounting a tip in the system

Commercial tuning forks are usually sold in a vacuum environment to increase their quality factor. Their vacuum shell can be removed using a manual milling machine. The fork is then soldered with an approximate angle of 30° to a PCB holder and its two legs are contacted to their respective pins, see the central image of Figure 5.2.1.

Since the microfabrication process did not reach its term, no Akiyama probe was available to be mounted in the system. Thus a single cantilever probe was used. Commercial tips consist of a cantilever that is attached to a large contact pad. For this homebuilt set-up, a special procedure is required to break and mount the cantilever on a tuning fork.

The cantilever is broken from its pad by approaching the tuning fork from behind after precise alignment with x,y and z micrometer screws. The cantilever is glued on one prong of the tuning fork using silver epoxy. Finally, the whole device is placed in a furnace at 140°C for one hour to cure the silver epoxy. The result is illustrated at Figure 5.2.1.

Finally, the PCB holder can be attached to the scanning piezoelectric tube, shown on the left picture of Figure 5.2.1. The tuning fork is tuned to obtain its resonance frequency and its quality factor. Due to the extra mass, the quality factor is lowered. The resonance frequency is also lowered for the same reason but is still suitable for scanning. Once that the TF is mounted and tuned, the set-up is ready for AFM imaging.

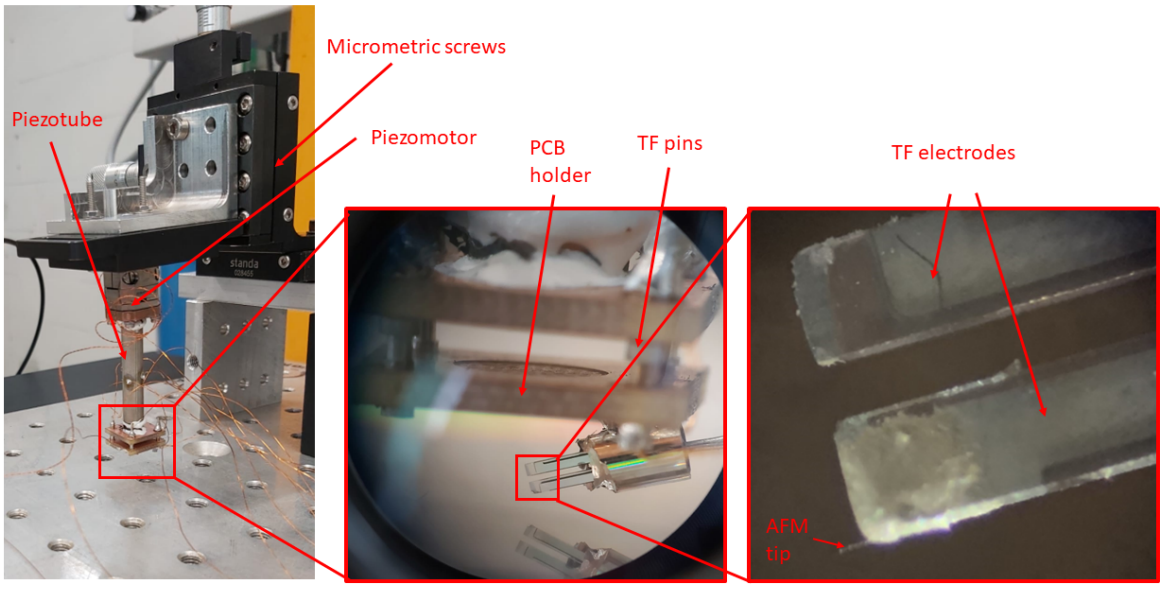

Figure 5.2.1: From left to right, the first photo illustrates the whole active part of the set-up, a red square indicates a zoom on the tuning fork's region. A second zoom on the tuning fork is presented to see the AFM tip. The two last images were obtained with the optical microscope that is also used for the coarse approach.

5.3 Images obtained with the set-up

This AFM set-up was used to successfully image samples. In particular, the set-up was used to image one of the FIBID thin films deposited in subsection 4.7.2. Although, since it

does not have a camera mounted vertically over the tip, the *Bruker Icon* was preferred to do the systematic measurements. This scan is presented in Figure 5.3.1. A line scan was chosen along the line to extract the thickness. For the homebuilt AFM, important levelling issues exist, as further discussed at section 5.4. They were corrected by subtracting a baseline based on a linear regression a serie of points far from the deposited film. This line as well as the resulting profile are presented at Figure 5.3.3.

Another scan, made by J. Spiece, is presented at Figure 5.3.2. A CoFeB/Pt nanowire is connected to 4 electrodes for a 4-points resistance measurement.

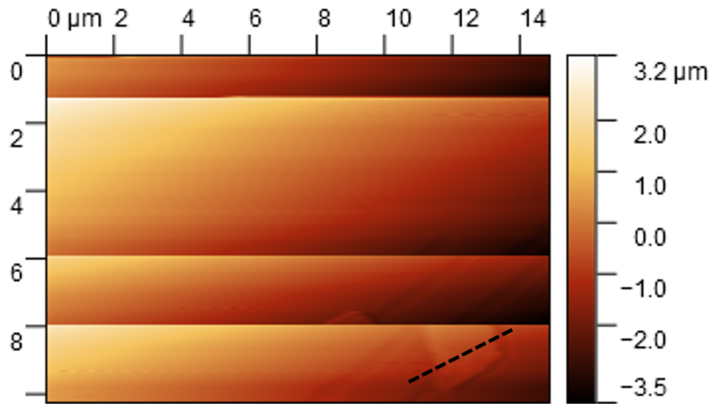

Figure 5.3.1: AFM image of a thin film of C over gold electrodes as described in subsection 4.7.2. the image shows abrupt transitions due to the tilting effect requiring piezomotor movement.

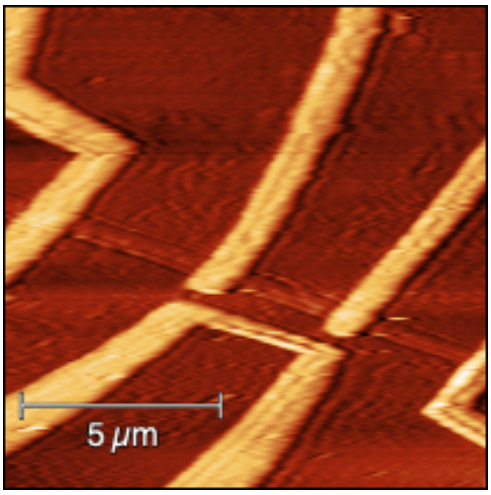

Figure 5.3.2: AFM image obtained with the homebuilt set-up of a 4-point resistance measurement. this image was obtained by J. Spiece.

5.4 Issues and future developments

Range limitations The maximum size of the image from this homebuilt set-up is limited. The angle between the sample and the scan tube induces a tilting while scanning. If this tilting overcomes the vertical range of the piezotube, the AFM tip will break. The tilt angle can be easily estimated with trigonometry with the base signal removed from any profile such as the one of Figure 5.3.3. It lies around 10° with respect to the horizontal axis.

This angle, associated with the limited vertical range of the piezotube, $7.4\mu m$, limits the horizontal range since one has to periodically drive the piezomotor up to avoid crashing the tip. This results in abrupt transition in the measurement, as shown on images Figure 5.3.1.

The tilting problem on the set-up must be tackled to allow a day-to-day use of the set-up. Another solution for the gluing must be found. For the remaining angle, a tilting

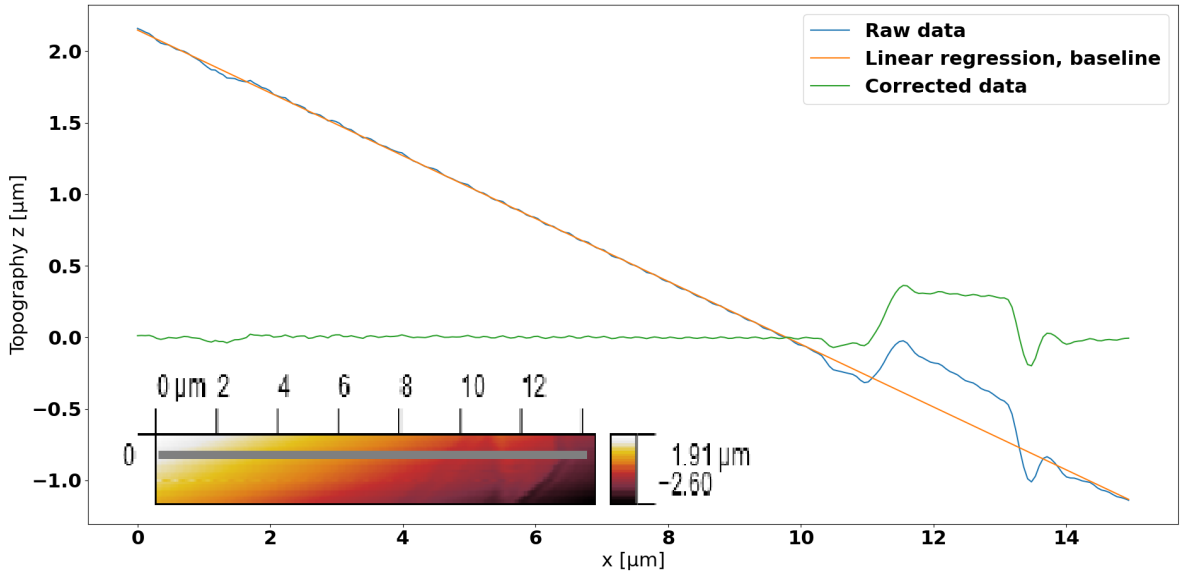

Figure 5.3.3: Raw data, linear regression and corrected data for a line scan with the homebuilt AFM set-up. The profile is presented at Figure 5.3.1. The inset image shows the full scan with in grey the line scan considered.

base with micrometric screws will be implemented for further corrections.

Low-temperature and vacuum compatibility The piezomotor and piezotube are compatible with vacuum as they do not contain any outgassing material. Both are also compatible with cryogenic temperatures but their displacement sensitivities decrease. Fortunately, their tolerances to high voltage increase as well [99]. This allows to use them at these temperatures, given that a correction factor is applied to the voltage used.

Their dimensions were also chosen to fit in the tight space of a ^{3}He cryostat that will be installed in the host lab.

In addition, the measurement circuitry will have to be compatible with these low temperatures. In particular, a pre-amplifier could be placed on and thermally anchored to the 1K pot to limit Joule losses in the lowest temperature chamber while limiting the electrical thermal noise. The cables used should also be properly thermally anchored and compatible with these temperatures.

These modifications will be implemented in future works to achieve SThM measurements below 20K.

Chapter 6

Conclusion and perspectives

In this work, major progress towards the implementation of a cryogenic SThM set-up at UCLouvain was achieved. The completion of the objectives that were defined in the introduction can be summarised as follows :

- The mechanical and thermal behaviour of an Akiyama SThM probe were successfully simulated and allowed to define dimensions for the probe. The results were coherent with analytical models and data provided by probe's manufacturers.
- The following calibration parameters of a SThM probe were estimated: the thermal resistances of the cantilevers R_{ca} and the tip R_t. The effective air conduction coefficient h was also estimated.
- The impact of the following parameters on the performances of a SThM probe were assessed : pressure of the experimental chamber, position of the heater on the tip and thermal conductivity of the sample. They allowed to draw guidelines for experiments with SThM.
- A fabrication process was proposed and investigated for the microfabrication of an Akiyama SThM probe. The fabrication by TMAH etching of two-stages atomic force microscopy (AFM) probes, with apex radii of 30nm, was demonstrated. The apex of these probes were successfully metallised thanks to the partial covering of a spin-coated resin.
- Thin films of amorphous carbon, platinum and zirconium nitride were deposited on silicon wafers. An experiment to measure their electrical conductivity at low temperature could be performed but the data were not exploitable since the sample had burnt during the measurement. Their deposition on AFM tips was prevented by a breakdown of the FIB-SEM equipment.
- Akiyama cantilevers and pads were successfully defined on a SOI wafer. The impact of the resulting rough surface on mechanical properties remains to be assessed.

- Electrical contacts were successfully deposited on a dense array of AFM tips but their alignment on a single tip could not be achieved. A new mask with alignment marks closer to the patterns should be designed.
- An AFM set-up using a self-sensing tuning fork for its feedback was successfully used to image samples from this work and others. The tilting problem that was identified still limits its applications and further works

These results pave the way towards the study of thermal exchanges at the nanometer scale and at cryogenic temperatures at UCLouvain. Building on the acquired knowledge, future works should put together all these steps to achieve a functioning Akiyama SThM probe. Further works should also focus on the characterisation at low temperatures of the heating resistance material using the procedure that is proposed in this work. The implementation of the developed AFM set-up in a ^{3}He cryostat remains to be done. Important milestones were achieved that will allow the realisation of this goal. When successfully accomplished, this setup will be the world first low temperature SThM enabling cutting edge research and opening new scientific endeavour.

Acknowledgements

I would like to acknowledge the contributions to this works of several people who supported me and helped me throughout the year.This works owes a lot to each of you.

First I would like to express my gratitude to my supervisors, PR. Pascal Gehring and Pr. Benoît Hackens. Their dedication and availability for this project were impressing. They left me a lot of freedom to experiment different paths and always provided me excellent guidance whenever needed. Thank you for mentoring me all year long and introducing me to this fascinating research field.

I would like to thank Jean Spiece for the fruitful discussions about the simulations of this work and for teaching me how to use an AFM. His insights were always very helpful. His enthusiasm for the project and his patience were precious and deeply appreciated.

Sébastien Faniel, Nicolas André and Michaël Coulombier deserve my deepest gratitude for teaching me how to use all the machines required in this project. They spent a lot of time working with me on my process and the results presented in this work could never have been achieved without their experience and suggestions.

During this master thesis, I had the pleasure to be immersed in Pr. Gehring's research group. It was always a pleasure to attend the journal clubs and group meetings. I learned a lot from these passionate researchers about a variety about a variety of subjects. I would like to thank all of them for these exciting discussions. A special thanks to Alessandra Canetta for always supporting me and for drawing excellent doodles in my thesis !

I would also like to thank Pr. Pierre Eloy (BSMA) for realising the XPS measurement and its analysis, Yubin Huang (NAPS) for the ZrN deposition and Pr. Merckling (IMEC) for its XRR measurement, Roseline Vercauteren and Diego Calderon for helping me with the Bosch process and the *Vacotec* respectively.

Last but not least I would like to thank warmly my family and friends for their support throughout the year. Special thanks to the Fyki gang with whom we made it through the years and difficulties with an incredible amount of laughs along the way. Finally I would like to thank my girlfriend for believing in me and for her unwavering support especially

when I was writing my thesis.

Appendix A

Appendices

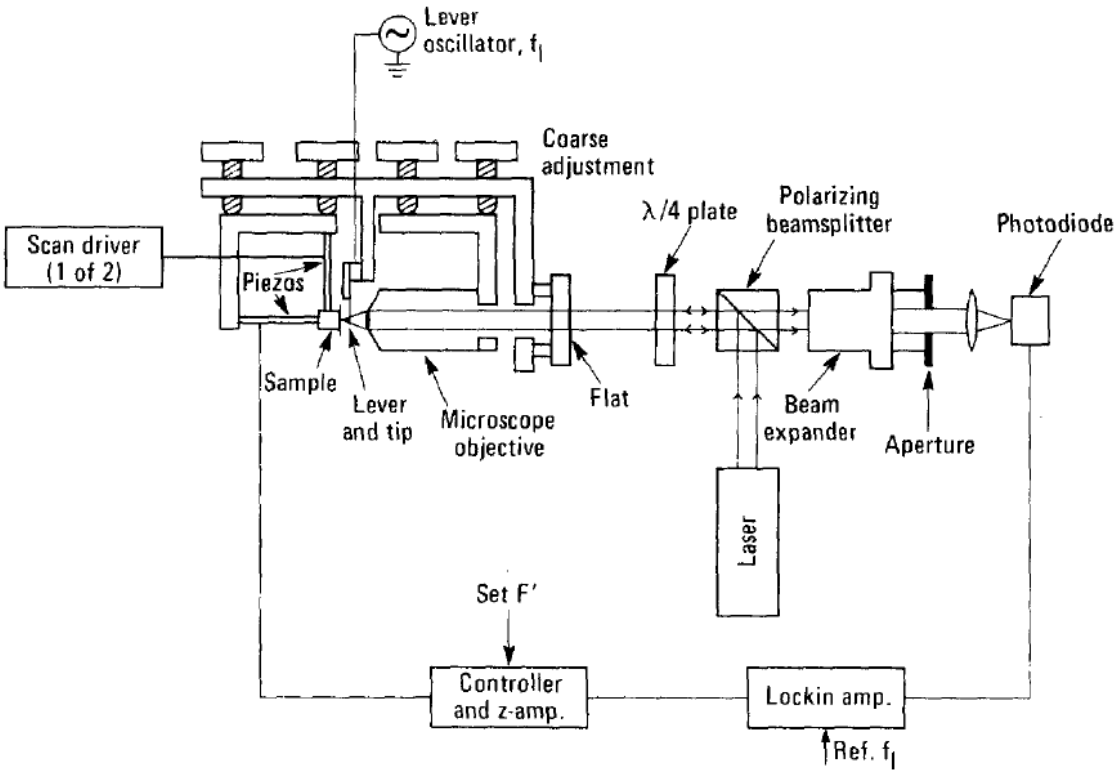

Figure A.0.1: Schematic drawing of an AFM set-up based on interferometry feedback. In this example an optical microscope's objective is also placed on the trajectory of light but this is not a prerequisite for the technique. This figure illustrates subsection 2.1.2. [21]

State of the art : Additional images

Figure A.0.2: SEM image of a Wollaston probe with its different constituting elements labelled, excerpted from [77].

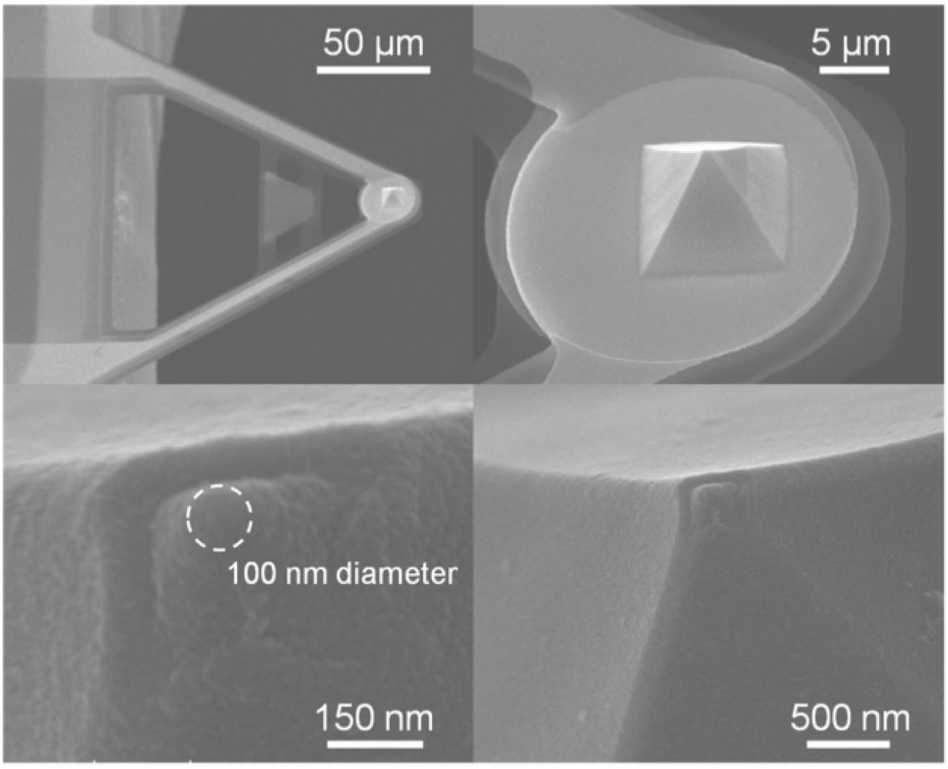

Figure A.0.3: SEM images of a thermovoltage based SThM probe based on a Cr/Au junction, from [34]. The thermocouple junction is visible on the lower left image.

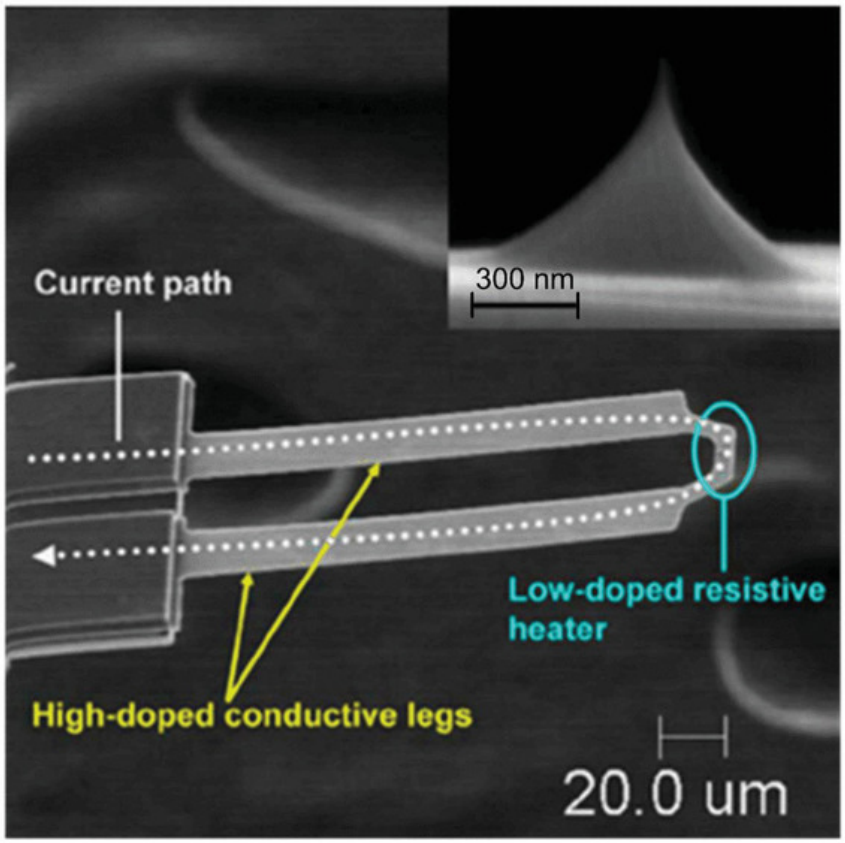

Figure A.0.4: SEM image of a doped Si SThM probe, from [77].

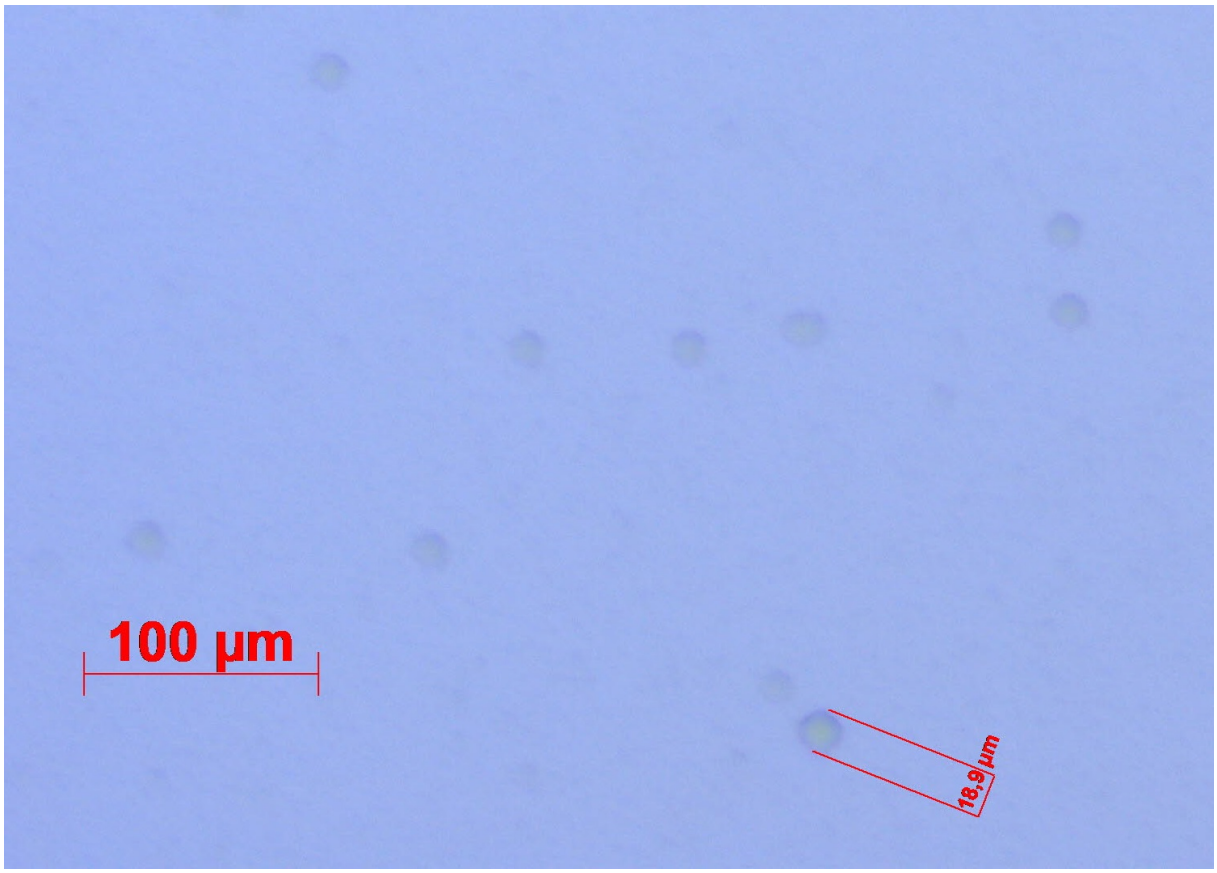

Figure A.0.5: General surface state of a Si substrate after 20min in 25% TMAH at 83°C in an horizontal position. Craters caused by bubbling can clearly be distinguished from the general roughness.

Images and schematics of fabrication steps

$$e_i = \frac{|\Psi_{\text{exp},i} - \Psi_{\text{theo},i}|}{\Psi_{\text{exp},i}} + \frac{|\Delta_{\text{exp},i} - \Delta_{\text{theo},i}|}{\Delta_{\text{exp},i}} \tag{A.0.1}$$

$$RMSE = \sqrt{\frac{\sum_i^N \Psi_{\text{exp},i} - \Psi_{\text{theo},i}}{N}} + \sqrt{\frac{\sum_i^N \Delta_{\text{exp},i} - \Delta_{\text{theo},i}}{N}} \tag{A.0.2}$$

X-ray reflectivity (XRR) of ZrN_x thin films deposited using reactive sputtering. The XRR measurement aims at analysing the X-ray reflectivity of a surface at nearly vertical angles, up to $2\omega = 4°$ commonly. This technique can give different information about a thin-film or a multilayer structure such as its thickness, local electron density or buried interfaces. Unfortunately, it is not directly sensitive to the crystallinity of the film. More complex analyses, along with simulations and fitting, can help to determine crystal structure but this kind of resources were not available at the time of writing.

The XRR results are presented at Figure A.0.14 along with an illustration excerpted from [100]. The thicknesses were determined through curve fitting with a dedicated

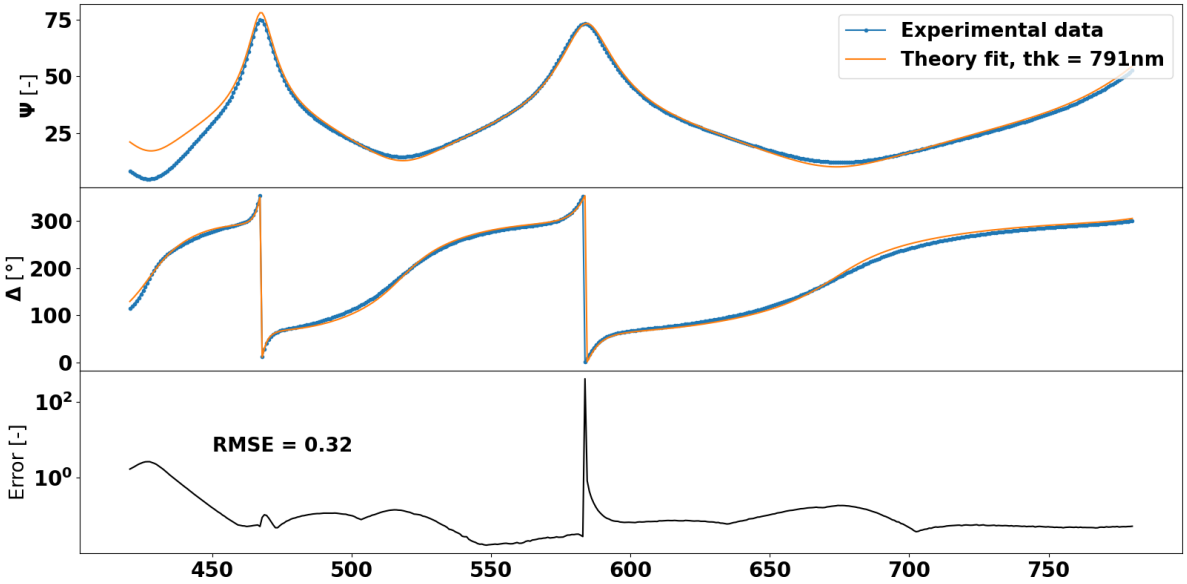

Figure A.0.6: Ψ, Δ and error spectra obtained by ellipsometry on a thin film of *AZ701* spin-coated at 5000rpm for 1 minute on a patterned surface. The local error and RMSE were computed using Equation A.0.1 and Equation A.0.2 respectively.

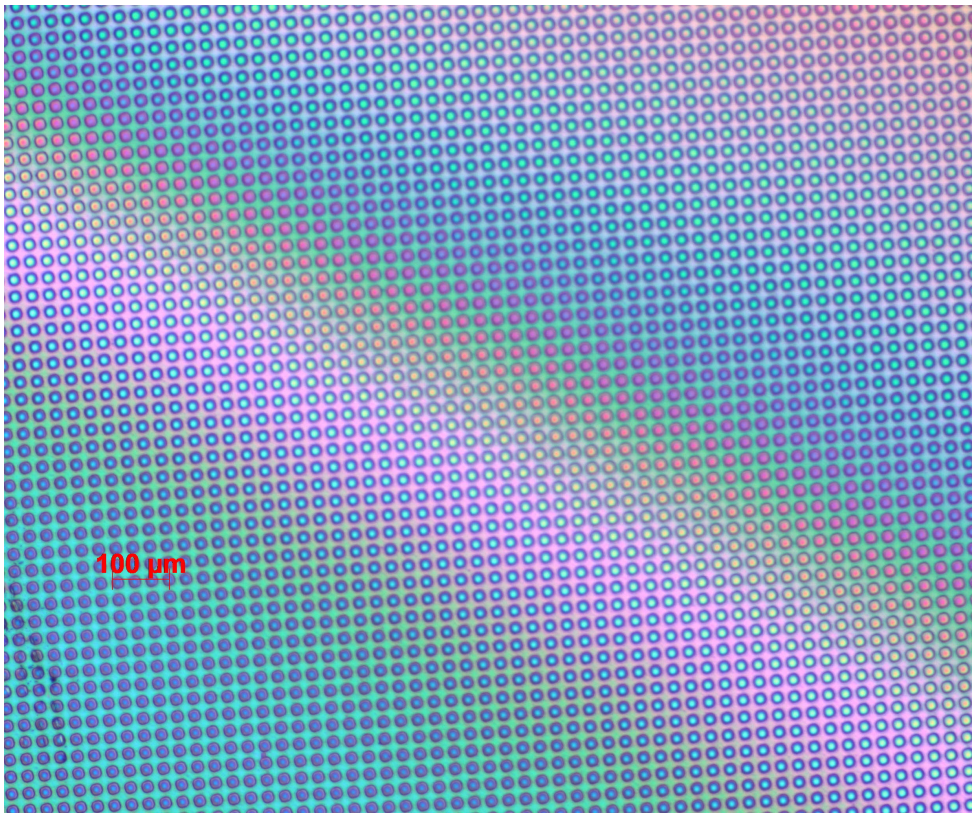

Figure A.0.7: Thickness's waves in *AZ701* that was spin-coated at 5000rpm on a dense pattern.

software and are listed in Table 4.1. The experimental parameters that were used for the

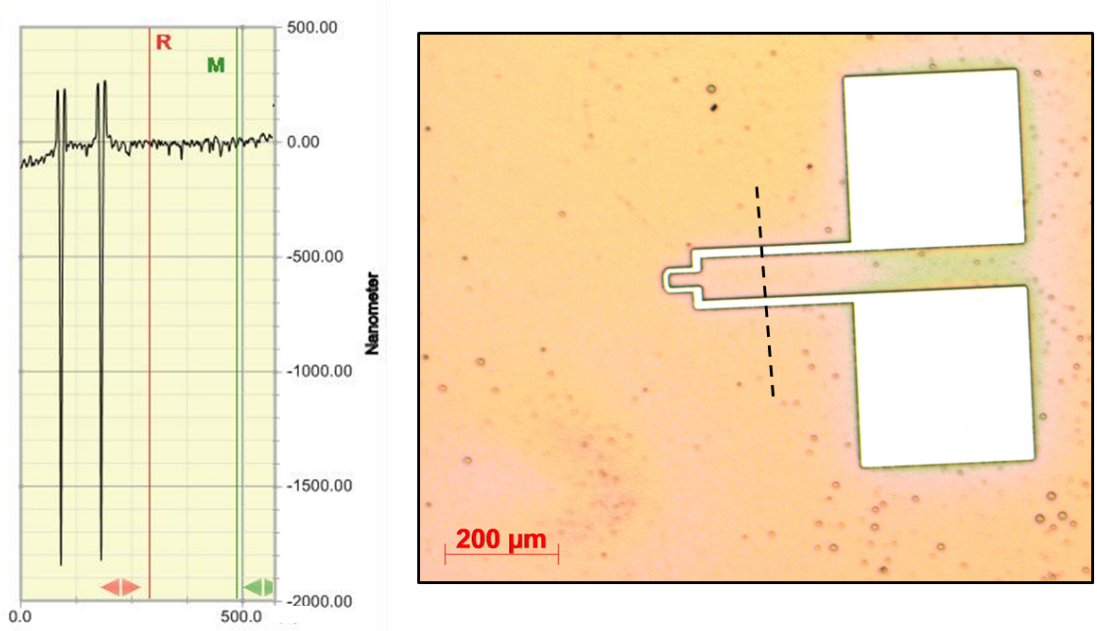

Figure A.0.8: Profilometer scan through an electrical contact's pattern defined negatively in *AZ2020*. The line along which the scan was made is presented by a dashed line on the optical image on the right.

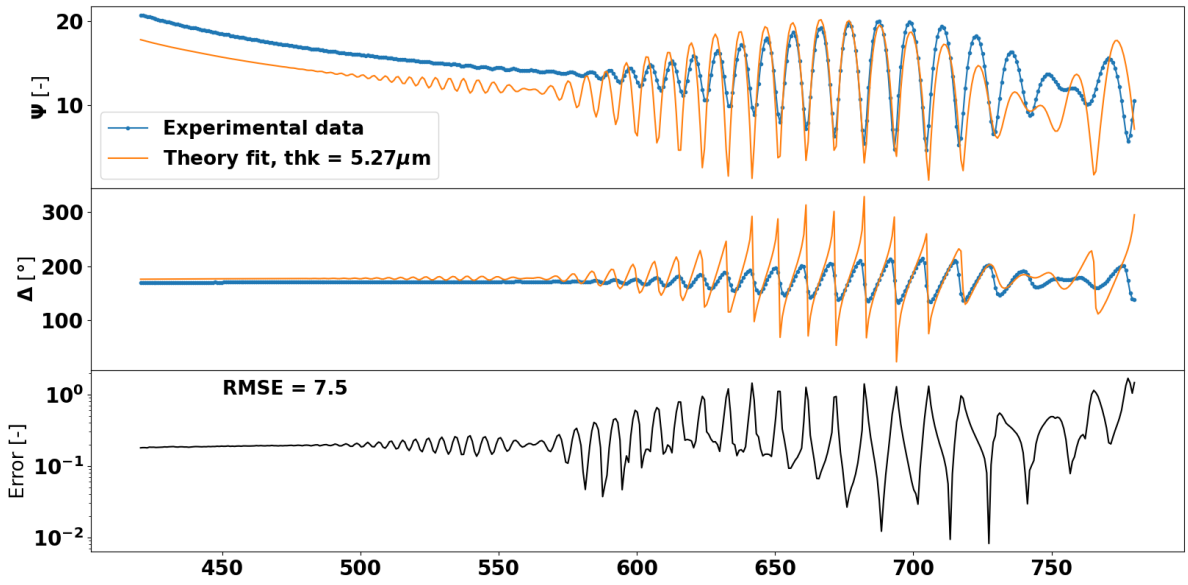

Figure A.0.9: Ψ, Δ and error spectra obtained by ellipsometry on a SOI wafer that was thinned in a TMAH solution.

three samples can be found at Table 4.1.

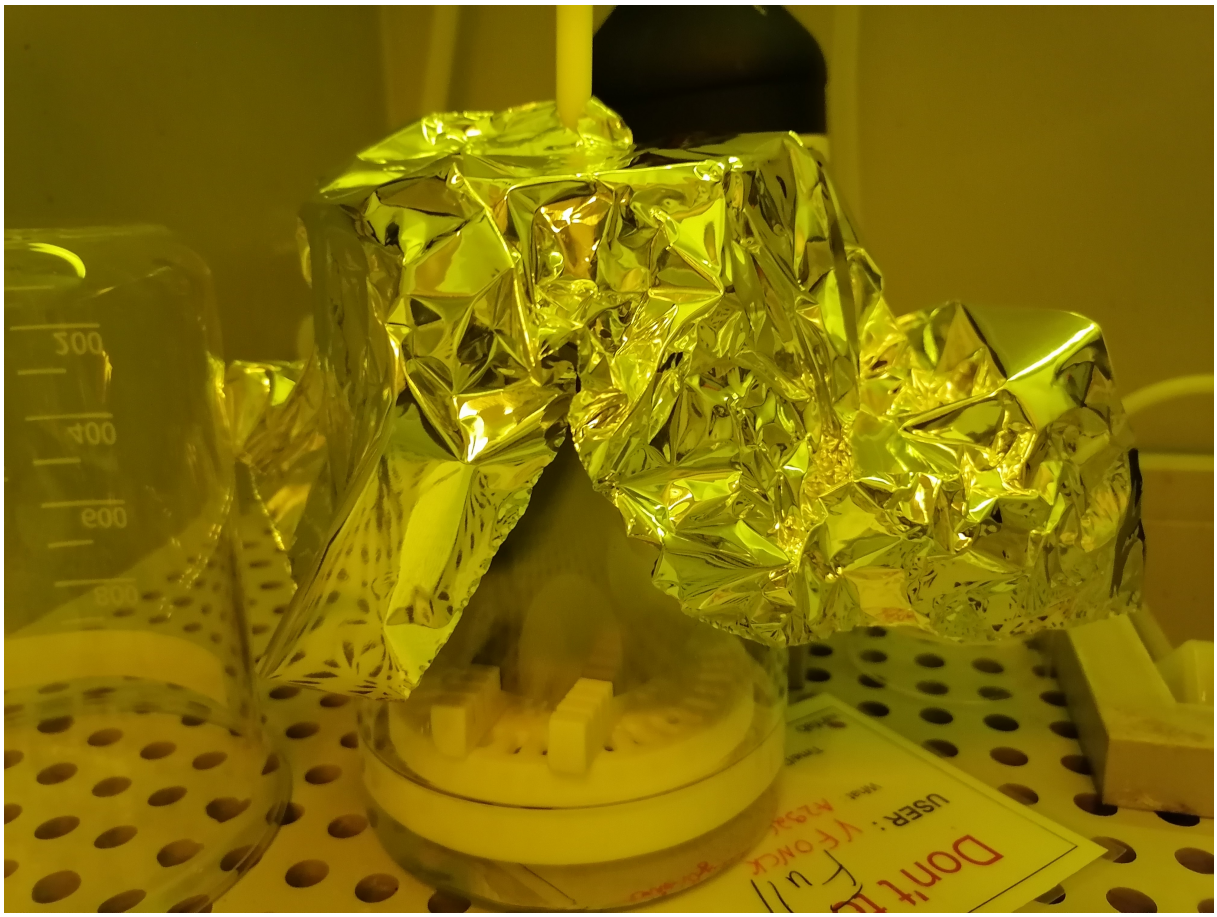

Figure A.0.10: Images of the set-up used for rehydrating the photoresin *AZ9260* after spin-coating and soft baking.

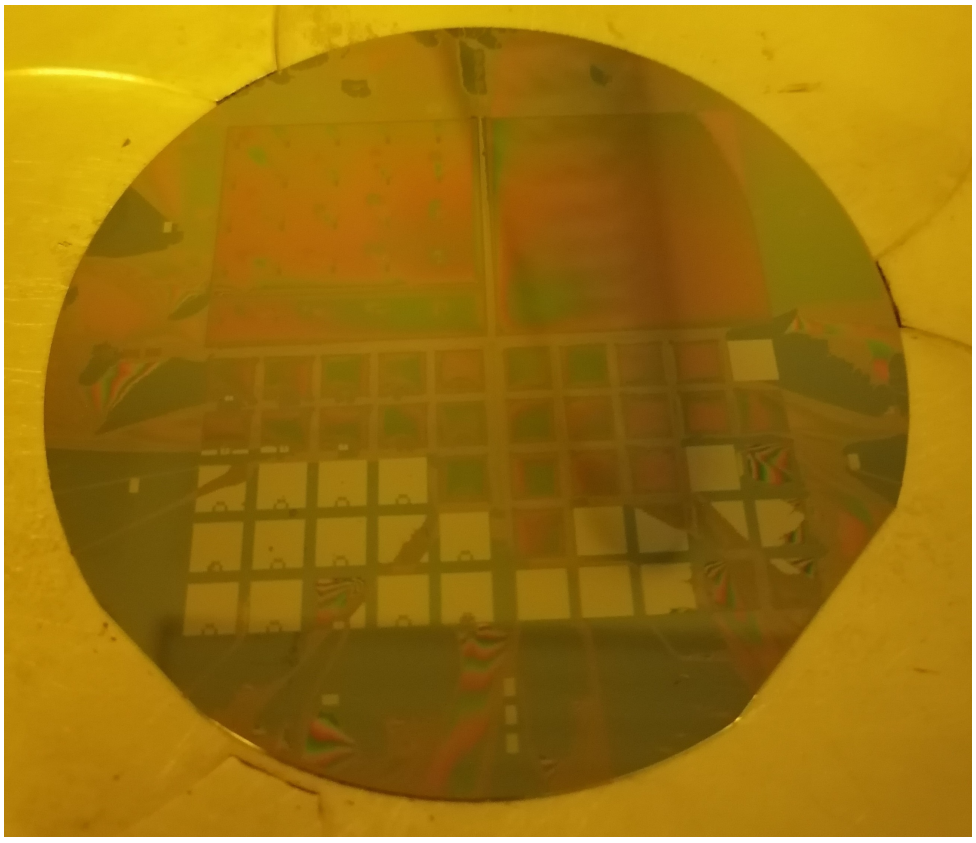

Figure A.0.11: Spin-coating inhomogeneities on a wafer with high aspect ratio structures. The photoresin used was *AZ9260*.

Figure A.0.12: Illustration of stripping marks due to the overdevelopment of *AZ9260*. The sample was placed for 30 minutes in *AZ700MIF*, a developer.

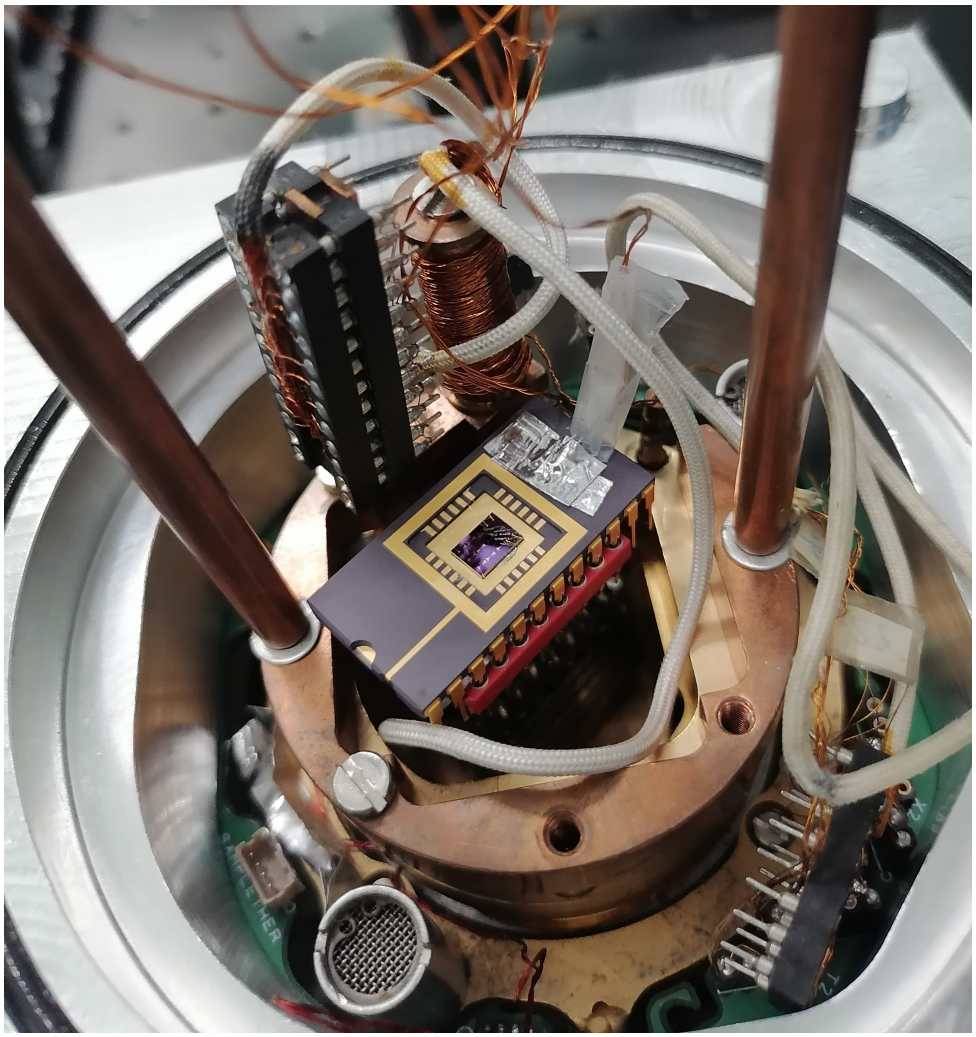

Figure A.0.13: Image of the chamber used for the low-temperature resistivity measurement described at Figure A and subsection 4.7.2. The radiation shield was removed. The added Pt1000 thermometer can be seen thermally anchored on the sample holder by metallic tape.

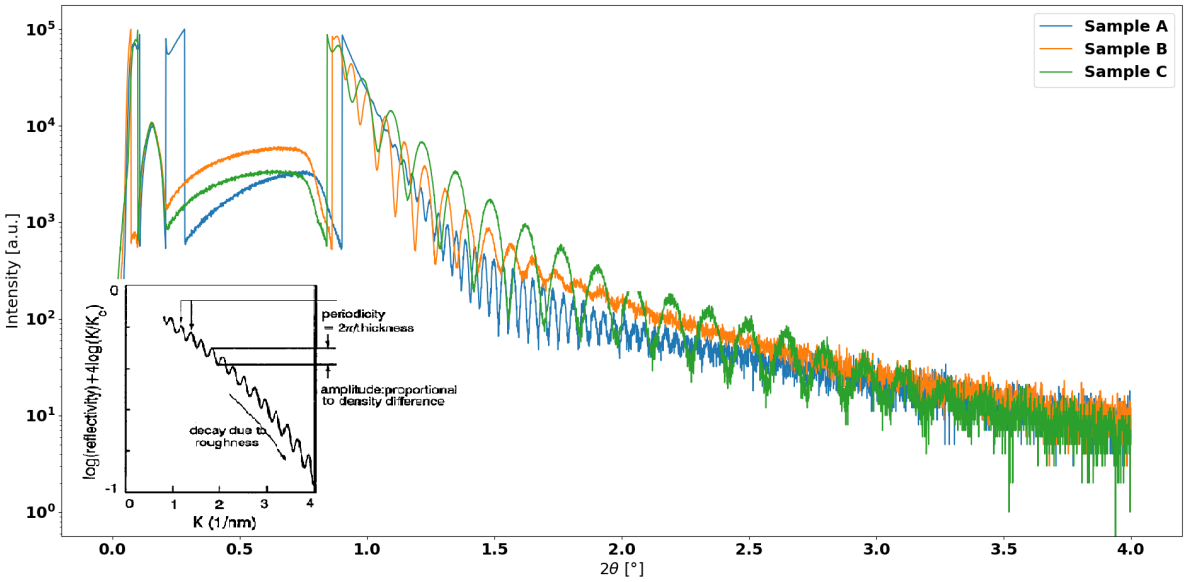

Figure A.0.14: XRR data obtained on Cernox samples obtained with different deposition parameters, listed at Table 4.1. The inset image, adapted from [100], indicates different characteristics that can be extracted from a XRR measurement. In particular, the periodicity of the peaks indicates the thickness of the film.

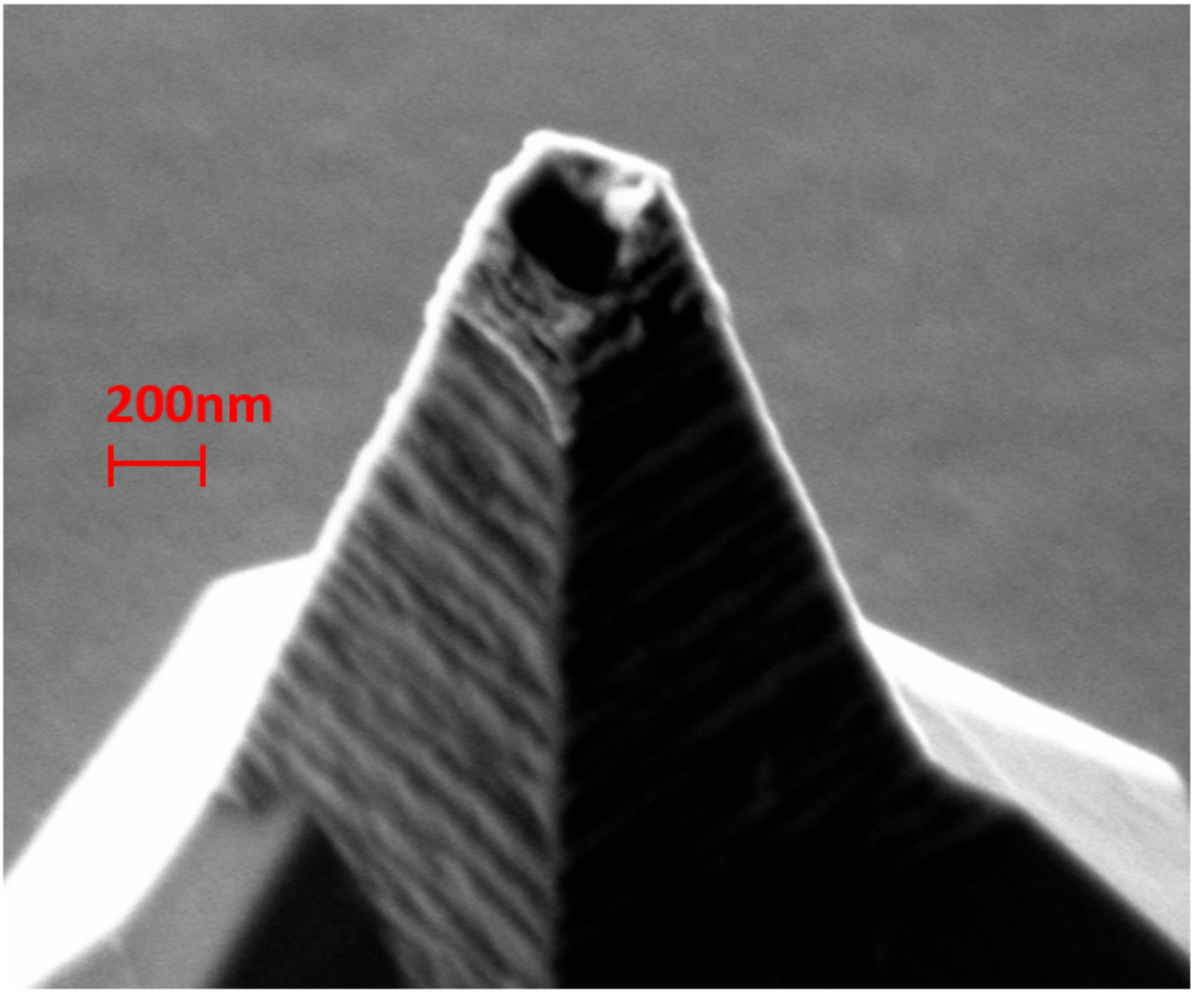

Figure A.0.15: SEM image of two stages AFM tips, defined at Figure 4.5.14. The aluminium thin film was deposited using a lift-off process. Its apex was broken, possibly during the lift-off.

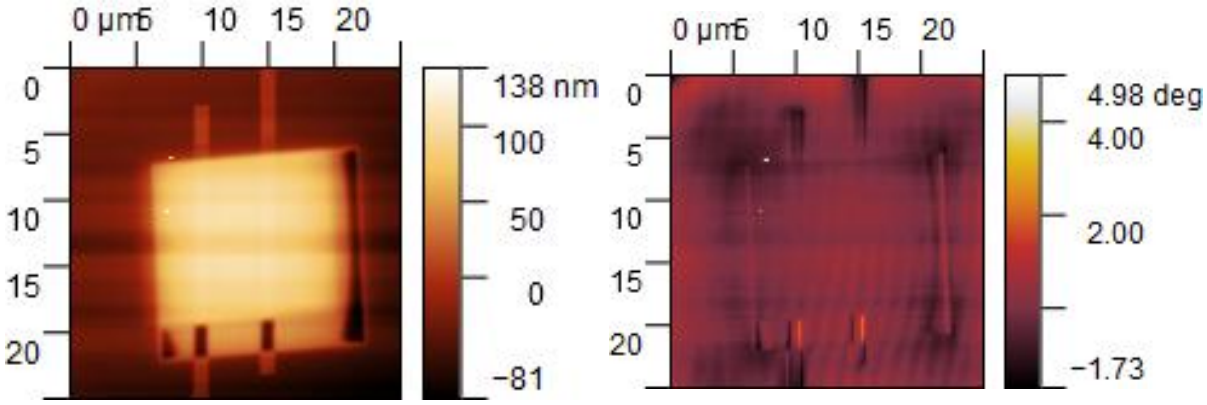

(a) Topography (b) Phase image

Figure A.0.16: AFM images of an amorphous graphene thin film deposited using FIBID on two gold contacts. It is labelled Pt1 at Table 4.2.

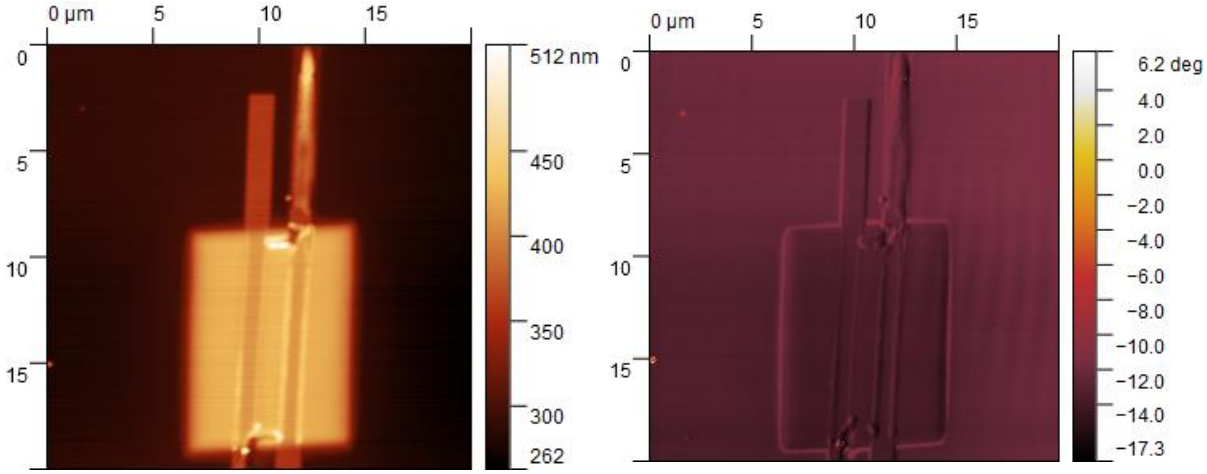

(a) Topography (b) Phase image

Figure A.0.17: AFM images of a platinum thin film deposited using FIBID on two gold contacts. It is labelled Pt2 at Table 4.2.

AFM images of FIB induced deposited C Pt samples

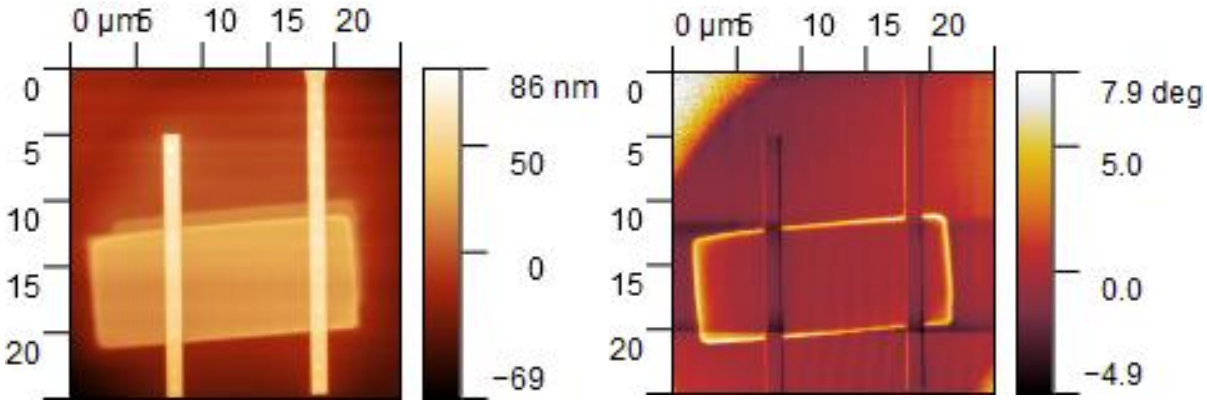

(a) Topography (b) Phase image

Figure A.0.18: AFM images of an amorphous graphene thin film deposited using FIBID on two gold contacts. It is labelled C1 at Table 4.2.

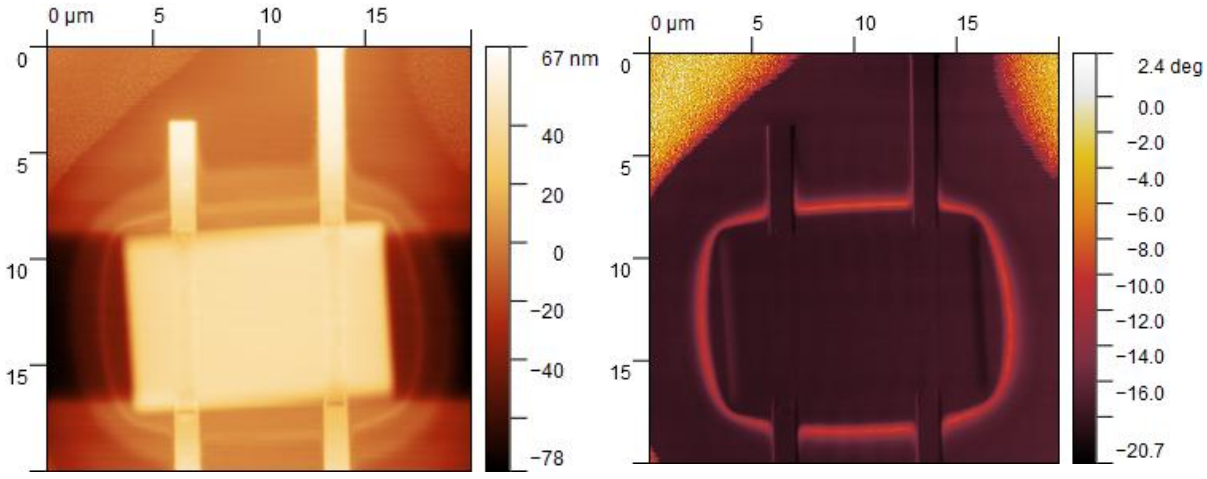

(a) Topography (b) Phase image

Figure A.0.19: AFM images of a platinum thin film deposited using focused electron beam induced deposition on two gold contacts. It is labelled C2 at Table 4.2.

Low temperature resistivity of amorphous carbon and metallic Pt thin films Unfortunately, after connection, a resistance could only be measured on one of the sample. The FIB induced deposition is an equilibrium between the milling by the ion beam and the deposition. it is possible that this milling damaged the gold contact. Thus, the sample will be the only one investigated in this work.

During the measurement, the chamber was first brought to its lowest achievable temperature using a dedicated feature of the software. Then, the chamber was heated using resistances near the cold head. Both resistance measurement were started synchronously and the signals were recorded along time. The thermometer resistance was measured directly by applying a known voltage at 17Hz and measuring the associated current. For the sample, a pseudo 4 points measurement was used with a resistance of 100MΩ in series with the thin film to avoid important current. A frequency of 17Hz was also used.

By assuming a good thermalisation, the time axis can be transformed into a temperature using the calibration curve provided by the thermometer's manufacturer. Although the set-up can in theory reach 3K, the curve is only plotted down to 200K as this is the lowest temperature achievable by a Pt1000 thermometer. The resistivity was extracted using the dimensions provided at Table 4.2 using the Pouillet's law. The resulting graph is presented at Figure 4.7.7.

Since, as already stressed at subsection 4.7.2, the curve did not match the expectation for a ceramic, further investigations were conducted. In particular, the frequency dependence of the contact was assessed at ambient temperature. In particular, a DC measurement gave a null I-V curve that showed that the contact was not Ohmic. Optical and SEM images confirmed that the thin film was burnt during the measurement as shown on Figure A.0.20a and Figure A.0.20b. An AFM image of the thin film before measurement can be found at Figure A.0.18.

The temperature of the sample is thus extracted from the resistance measurement of the Pt resistance. The table presented at Table A.1 is used and a linear interpolation is used between these points.

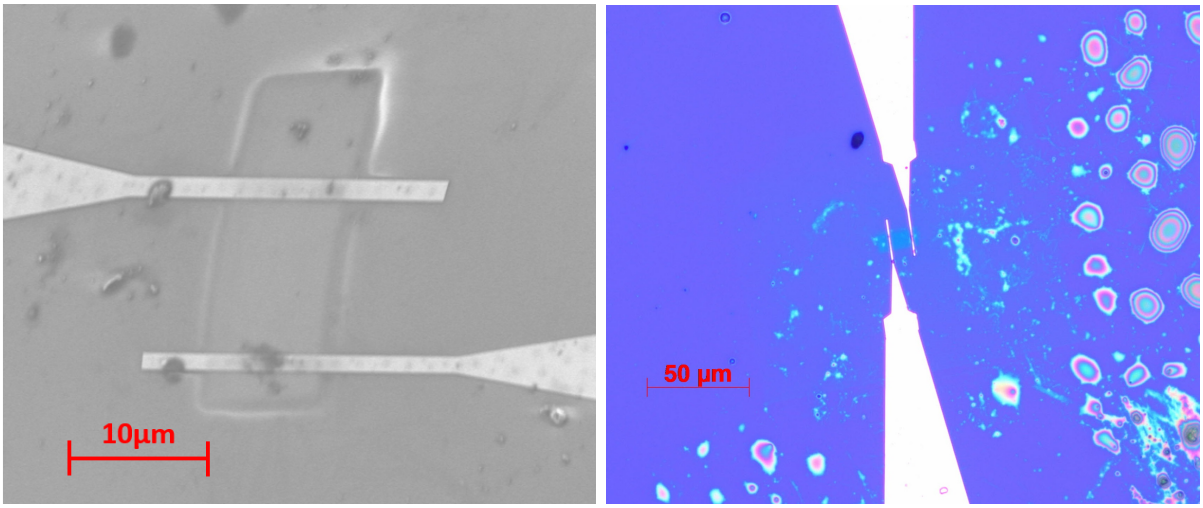

(a) SEM image (b) Optical image

Figure A.0.20: Images of a burnt amorphous carbon thin film deposited using FIBID. The images were taken after the resistivity measurement described at Figure A.

	0	1	2	3	4	5	6	7	8	9
-70	723.3	719.3	715.3	711.3	707.3	703.3	699.3	695.3	691.3	687.3
-60	763.3	759.3	755.3	751.3	747.3	743.3	739.3	735.3	731.3	727.3
-50	803.1	799.1	795.1	791.1	787.2	783.2	779.2	775.2	771.2	767.3
-40	842.7	838.7	834.8	830.8	826.9	822.9	818.9	815.0	811.0	807.0
-30	882.2	878.3	874.3	870.4	866.4	862.5	858.5	854.6	850.6	846.7
-20	921.6	917.7	913.7	909.8	905.9	901.9	898.0	894.0	890.1	886.2
-10	960.9	956.9	953.0	949.1	945.2	941.2	937.3	933.4	929.5	925.5
0	1000.0	996.1	992.2	988.3	984.4	980.4	976.5	972.6	968.7	964.8
0	1000.0	1003.9	1007.8	1011.7	1015.6	1019.5	1023.4	1027.3	1031.2	1035.1
10	1039.0	1042.9	1046.8	1050.7	1054.6	1058.5	1062.4	1066.3	1070.2	1074.0
20	1077.9	1081.8	1085.7	1089.6	1093.5	1097.3	1101.2	1105.1	1109.0	1112.9
30	1116.7	1120.6	1124.5	1128.3	1132.2	1136.1	1140.0	1143.8	1147.7	1151.5

Table A.1: Calibration data for a Pt1000 thermometer from *Sterling Sensors* [101]

Figure A.0.21: Homebuilt AFM set-up, the piezotube, piezomotor, tuning fork and sample are placed on a damping table. A close-up view of these elemnts is provided at Figure A.0.22. The control units are connected to a computer not shown.

AFM set-up images

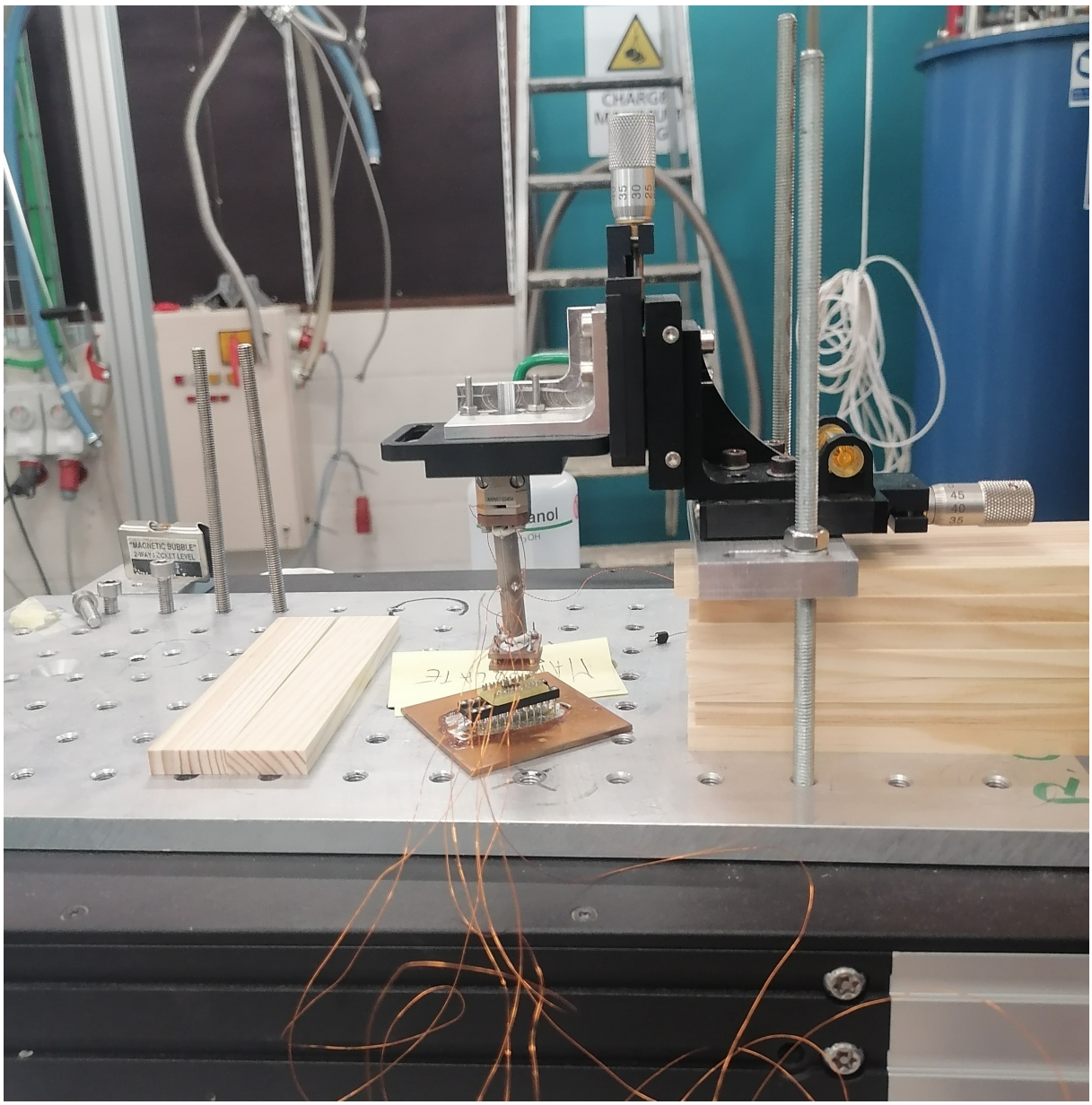

Figure A.0.22: Close-up view on the scanning part of the AFM set-up presented at section 5.1.

Thermistor reading This section presents the first step towards the design of an electronic interface to read the temperature signal. Due to a lack of time, this was not experimentally realised but will be needed for further development of a functional active SThM probe. The following discussion is highly inspired from different arguments and design examples found in [19].

The active mode SThM, as explained at section 2.2, is based on the measurement the change in resistivity with temperature of the heating element. The most reliable and practical way to measure this change of resistance would be the use of a Wheatstone bridge. Unfortunately, this approach would imply considerably more fabrication steps and it was not considered viable in this project. Thus, the easiest solution is the voltage divider shown in Figure A.0.23. R_{ref} is a second resistance which is considered known and to stay at constant temperature T_0. So the transfer function is:

$$\frac{V_{out}}{V_{in}} = \frac{R_s}{R_{ref} + R_s} \tag{A.0.3}$$

We define α_T as the coefficient describing the change of resistivity with temperature. In this naive approach, this variation is considered as linear. This approximation is valid if the measurement is limited to a small range of temperatures. In practice, the curve of $\alpha_T(T)$ is measured using a calibrated thermometer. This coefficient thus depends on the material as well as the temperature range considered.

$$\frac{R_S(T)}{R_S(T_0)} = 1 - \alpha(T_0)(T - T_0) \tag{A.0.4}$$

$$\frac{V_{out}}{V_{in}} = \frac{R_s(T_0) \times (1 - \alpha(T_0)(T - T_0))}{R_{ref} + R_s(T_0) \times (1 - \alpha(T_0)(T - T_0))} \tag{A.0.5}$$

The sensitivity of this interface with respect to the sensing resistance is presented at Equation A.0.6. It is clear that the sensing resistance has to be minimised and the change of temperature maximised to increase the sensitivity. The thermal noise generated by the resistances is $\frac{\overline{v_n^2}}{\Delta f} = 4kT_0(R_{ref} + R_s)$. Since the SNR is the ratio of the signal power over noise power, to increase the SNR the noise power has to be reduced by minimising the value of the resistances. So the SNR can be written as Equation A.0.7. Δf is the bandwidth of the measurement. By equalling R_{ref} to $R_s(T_0)$, the SNR and the sensitivity are both increased. In addition, it appears clearly that increasing the temperature change for a given power increases the sensitivity and the SNR as expected. This justifies the minimisation of the tip's thermal resistance that was pursued at chapter 3.

$$\frac{\partial V_{out}}{\partial R_s} = \frac{R_{ref}}{(R_{ref} + R_s)^2} \tag{A.0.6}$$

$$\text{SNR} = \frac{v_{s,rms}^2}{v_{n,rms}^2} = \frac{(\frac{R_s V_{in}}{2(R_{ref}+R_s)})^2}{4kT(R_{ref}+R_s)\Delta f} \tag{A.0.7}$$

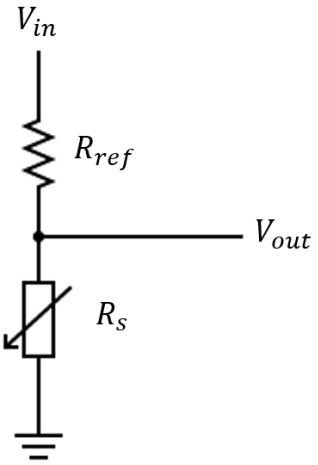

Figure A.0.23: Electrical circuit for a voltage divided. R_S denotes the sensing resistance that varies with temperature, R_{ref} a reference resistance that mus be calibrated.

Bibliography

[1] Aharon-Steinberg, A., Oreg, Y. & Stern, A. Phenomenological theory of heat transport in the fractional quantum Hall effect. *Physical Review B* **99**, 041302 (2019).

[2] Kim, M. *et al.* Micromagnetometry of two-dimensional ferromagnets. *Nature Electronics* **2**, 1–7 (2019).

[3] Fiege, G. B. M., Niedernostheide, F. J., Schulze, H. J., Barthelmeß, R. & Balk, L. J. Thermal characterization of power devices by scanning thermal microscopy techniques. *Microelectronics Reliability* **39**, 1149–1152 (1999).

[4] Lee, T. *et al.* Characterization of MOS Devices by Scanning Thermal Microscopy (SThM). *Conference Proceedings from the International Symposium for Testing and Failure Analysis* 191–197 (2001).

[5] Sachat, A. E. *et al.* Crossover from ballistic to diffusive thermal transport in suspended graphene membranes. *2D Materials* **6**, 025034 (2019).

[6] Srivastav, S. K. *et al.* Universal quantized thermal conductance in graphene. *Science Advances* **5**, eaaw5798 (2019). URL `https://www.science.org/doi/full/10.1126/sciadv.aaw5798`. Publisher: American Association for the Advancement of Science.

[7] Buccheri, F., Nava, A., Egger, R., Sodano, P. & Giuliano, D. Violation of the Wiedemann-Franz law in the topological Kondo model. *Physical Review B* **105**, L081403 (2022).

[8] Nakata, K., Ohnuma, Y. & Kim, S. K. Violation of the magnonic Wiedemann-Franz law in the strong nonlinear regime. *Physical Review B* **105**, 184409 (2022).

[9] Tanwar, P. K., Alam, M. S., Ahmad, M., Kaczorowski, D. & Matusiak, M. Severe violation of the Wiedemann-Franz law in quantum oscillations of NbP. arXiv:2205.12088 (2022).

[10] Kubala, B., König, J. & Pekola, J. P. Violation of the Wiedemann-Franz Law in a Single-Electron Transistor. *Physical Review Letters* **100**, 066801 (2008).

[11] Akiyama, T., Staufer, U., de Rooij, N. F., Frederix, P. & Engel, A. Symmetrically arranged quartz tuning fork with soft cantilever for intermittent contact mode atomic force microscopy. *Review of Scientific Instruments* **74**, 112–117 (2003).

[12] Binnig, G., Quate, C. F. & Gerber, C. Atomic Force Microscope. *Physical Review Letters* **56**, 930–933 (1986).

[13] Yang, C.-W., Hwang, I.-S., Chen, Y. F., Chang, C. S. & Tsai, D. P. Imaging of soft matter with tapping-mode atomic force microscopy and non-contact-mode atomic force microscopy. *Nanotechnology* **18**, 084009 (2007).

[14] Sweetman, A. M. *et al.* Mapping the force field of a hydrogen-bonded assembly. *Nature Communications* **5**, 3931 (2014).

[15] Albrecht, T. R., Grütter, P., Horne, D. & Rugar, D. Frequency modulation detection using high Q cantilevers for enhanced force microscope sensitivity. *Journal of Applied Physics* **69**, 668–673 (1991).

[16] Nanosensors. *Akiyama probe : technical note* (2022).

[17] Morgan, M. Basic principles of afm advanced modes and applications. *ND-NDT Spectrum Instruments* (2014).

[18] Nysten, B. *LMAPR2631 - SPMs : Resonant modes and other modes* (UCLouvain, 2021).

[19] Kaajakari, V. *Practical MEMS* (Small Gear publishing, 2009).

[20] Azcona, F. J., Jha, A., Yáñez, C., Atashkhooei, R. & Royo, S. Microcantilever Displacement Measurement Using a Mechanically Modulated Optical Feedback Interferometer. *Sensors* **16**, 997 (2016).

[21] Erlandsson, R., McClelland, G. M., Mate, C. M. & Chiang, S. Atomic force microscopy using optical interferometry. *Journal of Vacuum Science & Technology A* **6**, 266–270 (1988).

[22] Marrese, M., Guarino, V. & Ambrosio, L. Atomic Force Microscopy: A Powerful Tool to Address Scaffold Design in Tissue Engineering. *Journal of Functional Biomaterials* **8**, 7 (2017).

[23] Compliant, R. *ECS-3X8X, 2X6X, 1X5X. 32.768 KHz Tuning Fork Crystal Datasheet.* RoHS Compliant (2017).

[24] Nano & GMBH, M. *High Quality factor, Tapping Mode AFM Probe, for UHV Conditions.* Nano and More GMBH.

[25] Yalon, E. *et al.* Temperature Dependent Thermal Boundary Conductance of Monolayer MoS2 by Raman Thermometry. *ACS Applied Materials & Interfaces* **9**, 43013–43020 (2017).

[26] Chávez-Ángel, E. *et al.* Reduction of the thermal conductivity in free-standing silicon nano-membranes investigated by non-invasive Raman thermometry. *APL Materials* **2**, 012113 (2014).

[27] Serrano, J. R., Phinney, L. M. & Kearney, S. P. Micro-Raman thermometry of thermal flexure actuators. *Journal of Micromechanics and Microengineering* **16**, 1128–1134 (2006).

[28] Yue, Y. & Wang, X. Nanoscale thermal probing. *Nano Reviews* **3**, 11586 (2012).

[29] Goodson, K. & Asheghi, M. Near-field optical thermometry. *Microscale Thermophysical Engineering - MICROSCALE THERMOPHYS ENG* **1**, 225–235 (1997).

[30] Kramer, A., Segura, J.-M., Hunkeler, A., Renn, A. & Hecht, B. A cryogenic scanning near-field optical microscope with shear-force gapwidth control. *The Review of scientific instruments* **73**, 2937 (2002).

[31] Yan, Z., Liu, G., Khan, J. M. & Balandin, A. A. Graphene quilts for thermal management of high-power GaN transistors. *Nature Communications* **3**, 827 (2012).

[32] Bae, M.-H. *et al.* Ballistic to diffusive crossover of heat flow in graphene ribbons. *Nature Communications* **4**, 1734 (2013).

[33] Qian, R. *et al.* Developments on Thermometric Techniques in Probing Micro- and Nano-heat. *ES Energy & Environment* (2019).

[34] Kim, K., Jeong, W., Lee, W. & Reddy, P. Ultra-high vacuum scanning thermal microscopy for nanometer resolution quantitative thermometry. *ACS nano* **6**, 4248–4257 (2012).

[35] Gomès, S., Assy, A. & Chapuis, P.-O. Scanning thermal microscopy: A review. *physica status solidi (a)* **212**, 477–494 (2015).

[36] Albisetti, E. *et al.* Nanopatterning reconfigurable magnetic landscapes via thermally assisted scanning probe lithography. *Nature Nanotechnology* **11**, 545–551 (2016).

[37] Pylkki, R. J., Moyer, P. J. M. P. J. & West, P. E. W. P. E. Scanning Near-Field Optical Microscopy and Scanning Thermal Microscopy. *Japanese Journal of Applied Physics* **33**, 3785 (1994).

[38] Tong., T. W. Thermal conductivity 22. *International Thermal Conductivity Conference (22nd : 1993 : Arizona State University)* (1994).

[39] Pollock, H. M. & Hammiche, A. Micro-thermal analysis: techniques and applications. *Journal of Physics D: Applied Physics* **34**, R23–R53 (2001).

[40] Florescu, D. I. *et al.* High spatial resolution thermal conductivity of bulk ZnO (0001). *Journal of Applied Physics* **91**, 890–892 (2002).

[41] Volz, S., Feng, X., Fuentes, C., Guérin, P. & Jaouen, M. Thermal Conductivity measurements of Thin Amorphous Silicon films by Scanning Thermal Microscopy. *International Journal of Thermophysics* **23**, 1645–1657 (2002).

[42] Gomes, S. *et al.* Temperature Study of Sub-Micrometric ICs by Scanning Thermal Microscopy. *IEEE Transactions on Components and Packaging Technologies* **30**, 424–431 (2007).

[43] Beechem, T. & Graham, S. Temperature Measurement of Microdevices using Thermoreflectance and Raman Thermometry. In Hesketh, P. J. (ed.) *BioNanoFluidic MEMS*, MEMS Reference Shelf, 153–174 (Springer US, Boston, MA, 2008).

[44] Altet, J., Claeys, W., Dilhaire, S. & Rubio, A. Dynamic Surface Temperature Measurements in ICs. *Proceedings of the IEEE* **94**, 1519–1533 (2006).

[45] Kim, K. *et al.* Quantitative scanning thermal microscopy using double scan technique. *Applied Physics Letters* **93** (2008).

[46] King, W. *et al.* Heated Atomic Force Microscope Cantilevers and their Applications. *Annual Review of Heat Transfer* **12**, 287–326 (2013).

[47] Bodzenta, J., Kaźmierczak-Bałata, A., Lorenc, M. & Juszczyk, J. Analysis of Possibilities of Application of Nanofabricated Thermal Probes to Quantitative Thermal Measurements. *International Journal of Thermophysics* **31**, 150–162 (2010).

[48] Assy, A. & Gomès, S. Temperature-dependent capillary forces at nano-contacts for estimating the heat conduction through a water meniscus. *Nanotechnology* **26**, 355401 (2015).

[49] Zhang, Y., Dobson, P. S. & Weaver, J. M. R. High temperature imaging using a thermally compensated cantilever resistive probe for scanning thermal microscopy. *Journal of Vacuum Science & Technology B* **30**, 010601 (2012).

[50] Evangeli, C. *et al.* Nanoscale Thermal Transport in 2D Nanostructures from Cryogenic to Room Temperature. *Advanced Electronic Materials* **5**, 1900331 (2019).

[51] Gehring, P. *et al.* Efficient heating of single-molecule junctions for thermoelectric studies at cryogenic temperatures. *Applied Physics Letters* **115**, 073103 (2019).

[52] Spièce, J. Thermoelectric Phenomena in Graphene Constrictions. In Spièce, J. (ed.) *Quantitative Mapping of Nanothermal Transport via Scanning Thermal Microscopy*, Springer Theses, 119–133 (Springer International Publishing, Cham, 2019).

[53] Wen, Q. *et al.* Enhanced thermoelectric performance of BiCuSeO via dual-doping in both Bi and Cu sites. *Journal of Alloys and Compounds* **711**, 434–439 (2017).

[54] Serrano, F. *et al.* Record Seebeck coefficient and extremely low thermal conductivity in nanostructured SnSe. *Applied Physics Letters* **106**, 083902 (2015).

[55] Çinar, E., Kocyigit, S., Aytimur, A., Uslu, I. & Akdemir, A. Synthesis, Characterization, and Thermoelectric Properties of Electrospun Boron-Doped Barium-Stabilized Bismuth-Cobalt Oxide Nanoceramics. *Metallurgical and Materials Transactions A* **45** (2014).

[56] Wen, Q. *et al.* Enhanced thermoelectric performance of BiCuSeO via dual-doping in both Bi and Cu sites. *Journal of Alloys and Compounds* **711**, 434–439 (2017).

[57] Yotsuya, T., Yoshitake, M. & Kodama, T. Low-temperature thermometer using sputtered ZrNx thin film. *Cryogenics* **37**, 817–822 (1997).

[58] Yotsuya, T., Yoshitake, M. & Yamamoto, J. New type cryogenic thermometer using sputtered zr-n films. *Applied Physics Letters* **51**, 235–237 (1987).

[59] Barber, C. R. Platinum Resistance Thermometers of Small Dimensions. *Journal of Scientific Instruments* **27**, 47–49 (1950).

[60] Clement, J. R. & Quinnell, E. H. The Low Temperature Characteristics of Carbon-Composition Thermometers. *Review of Scientific Instruments* **23**, 213–216 (1952).

[61] Kar, S. & Sharma, R. Cryogenic Temperature Sensors. *Defence Science Journal* **57**, 195–208 (2007).

[62] Blagg, K., Allen, P., Lu, T.-M., Lilly, M. P. & Singh, M. Focused ion beam deposited carbon-platinum nanowires for cryogenic resistive thermometry. *Carbon* **169**, 482–487 (2020).

[63] Belanger, B. C. The Behavior of Carbon Resistor Thermometers in Magnetic Fields up to 100 kOe in the Pumped Liquid Helium and Hydrogen Temperature Ranges. *Review of Scientific Instruments* **40**, 1082–1085 (1969).

[64] Dusen, M. S. V. PLATINUM-RESISTANCE THERMOMETRY AT LOW TEMPERATURES1. *Journal of the American Chemical Society* **47**, 326–332 (1925).

[65] Neuringer, L. J., Perlman, A. J., Rubin, L. G. & Shapira, Y. Low Temperature Thermometry in High Magnetic Fields. II. Germanium and Platinum Resistors. *Review of Scientific Instruments* **42**, 9–14 (1971).

[66] Akiyama, T., Staufer, U. & de Rooij, N. F. Self-sensing and self-actuating probe based on quartz tuning fork combined with microfabricated cantilever for dynamic mode atomic force microscopy. *Applied Surface Science* **210**, 18–21 (2003).

[67] Akiyama, T. *et al.* Implementation and characterization of a quartz tuning fork based probe consisted of discrete resonators for dynamic mode atomic force microscopy. *Review of Scientific Instruments* **81**, 063706 (2010).

[68] Swartz, E. T. & Pohl, R. O. Thermal boundary resistance. *Reviews of Modern Physics* **61**, 605–668 (1989).

[69] Park, M., Lee, I.-H. & Kim, Y.-S. Lattice thermal conductivity of crystalline and amorphous silicon with and without isotopic effects from the ballistic to diffusive thermal transport regime. *Journal of Applied Physics* **116**, 043514 (2014).

[70] Rohsenow *et al.* Chapter 3. Conduction and Thermal Contact Resistances. *Handbook of Heat Transfer* (1997).

[71] Lefèvre, S. & Volz, S. 3ω-scanning thermal microscope. *Review of Scientific Instruments* **76**, 033701 (2005).

[72] Nanosensors. *Akiyama-Probe (A-Probe) technical guide.* Nanosensors.

[73] Felts, J. R. & King, W. P. Mechanical design for tailoring the resonance harmonics of an atomic force microscope cantilever during tip–surface contact. *Journal of Micromechanics and Microengineering* **19**, 115008 (2009).

[74] Alsteens, D. *et al.* Atomic force microscopy-based characterization and design of biointerfaces. *Nature Reviews Materials* **2**, 1–16 (2017).

[75] Systems, P. Afm probe selection guide. *Park Systems technical litterature* (2011).

[76] Laconte, J., Flandre, D. & Raskin, J. P. Silicon bulk micromachining with TMAH. In *Micromachined Thin-Film Sensors for SOI-CMOS Co-Integration*, 17–45 (Springer US, Boston, MA, 2006).

[77] Zhang, Y. *et al.* A Review on Principles and Applications of Scanning Thermal Microscopy (SThM). *Advanced Functional Materials* **30** (2020).

[78] Wu, Z. *et al.* A Unique Self-Sensing, Self-Actuating AFM Probe at Higher Eigenmodes. *Sensors* **15**, 28764–28771 (2015).

[79] Hoffman, D., Singh, B. & III, J. H. T. *Handbook of Vacuum Science and Technology* (Elsevier, 1997).

[80] Bodzenta, J., Juszczyk, J. & Chirtoc, M. Quantitative scanning thermal microscopy based on determination of thermal probe dynamic resistance. *The Review of scientific instruments* **84**, 093702 (2013).

[81] Tovee, P., Pumarol, M., Zeze, D., Kjoller, K. & Kolosov, O. Nanoscale spatial resolution probes for scanning thermal microscopy of solid state materials. *Journal of Applied Physics* **112**, 114317 (2012).

[82] Kosky, P., Balmer, R., Keat, W. & Wise, G. Chapter 12 - Mechanical Engineering. In Kosky, P., Balmer, R., Keat, W. & Wise, G. (eds.) *Exploring Engineering (Third Edition)*, 259–281 (Academic Press, Boston, 2013).

[83] Li, J., Xie, J., Xue, W. & Wu, D.-m. Fabrication of cantilever with self-sharpening nano-silicon-tip for AFM applications. *Microsystem Technologies* **19**, 285–290 (2013).

[84] Lee, J. *et al.* Fabrication of Atomic Force Microscope Probe with Low Spring Constant Using SU-8 Photoresist. *Japanese Journal of Applied Physics* **42**, L1171 (2003).

[85] Tang, B., Sato, K., Tanaka, H. & Gosalvez, M. A. Fabrication of sharp tips with high aspect ratio by surfactant-modified wet etching for the AFM probe. In *2011 IEEE 24th International Conference on Micro Electro Mechanical Systems*, 328–331 (2011).

[86] Habuka, H., Otsuka, T. & Katayama, M. In situ cleaning method for silicon surface using hydrogen fluoride gas and hydrogen chloride gas in a hydrogen ambient. *Journal of Crystal Growth - J CRYST GROWTH* **186**, 104–112 (1998).

[87] Merck. *Technical datasheet : AZMIR 701 series* (2016).

[88] Suter, K. *et al.* Integration of a Fabrication Process for an Aluminum Single-Electron Transistor and a Scanning Force Probe for Tuning-Fork-Based Probe Microscopy. *Microelectromechanical Systems, Journal of* **19**, 1088–1097 (2010).

[89] Chae, H., Hwang, G. & Kwon, O. Fabrication of scanning thermal microscope probe with ultra-thin oxide tip and demonstration of its enhanced performance. *Ultramicroscopy* **171** (2016).

[90] Haruyama, T. & Yoshizaki, R. Thin-film platinum resistance thermometer for use at low temperatures and in high magnetic fields. *Cryogenics* **26**, 536–538 (1986).

[91] Berg, S. & Nyberg, T. Fundamental understanding and modeling of reactive sputtering processes. *Thin Solid Films* **476**, 215–230 (2005).

[92] Rius, G., Perez-Murano, F. & Yoshimura, M. Graphene crystal growth by thermal precipitation of focused ion beam induced deposition of carbon precursor via patterned-iron thin layers. *Nanofabrication* **1** (2014).

[93] Belianinov, A. *et al.* Direct Write of 3D Nanoscale Mesh Objects with Platinum Precursor via Focused Helium Ion Beam Induced Deposition. *Micromachines* **11**, 527 (2020).

[94] Kim, C.-S., Ahn, S.-H. & Jang, D.-Y. Review: Developments in micro/nanoscale fabrication by focused ion beams. *Vacuum* **86**, 1014–1035 (2012).

[95] Instruments, M. *System User Manual Cryostation s-series.* Montana Instruments.

[96] Morgan, M. Electrical conduction in amorphous carbon films. *Thin Solid Films* **7**, 313–323 (1971).

[97] Adkins, C. J., Freake, S. M. & Hamilton, E. M. Electrical conduction in amorphous carbon. *The Philosophical Magazine: A Journal of Theoretical Experimental and Applied Physics* **22**, 183–188 (1970).

[98] Vorburger, T. V. & Ludema, K. C. Ellipsometry of rough surfaces. *Applied Optics* **19**, 561–573 (1980).

[99] Raghunvanshi, D. S., Moore, S. I., Fleming, A. J. & Yong, Y. K. Electrode Configurations for Piezoelectric Tube Actuators With Improved Scan Range and Reduced Cross-Coupling. *IEEE/ASME Transactions on Mechatronics* **25**, 1479–1486 (2020).

[100] Chason, E. & Mayer, T. M. Thin film and surface characterization by specular X-ray reflectivity. *Critical Reviews in Solid State and Materials Sciences* **22**, 1–67 (1997).

[101] Sensors, S. *Sterling RTD Pt1000 temperature sensor* (2011).

UNIVERSITÉ CATHOLIQUE DE LOUVAIN
École polytechnique de Louvain
Rue Archimède, 1 bte L6.11.01, 1348 Louvain-la-Neuve, Belgique | **www.uclouvain.be/epl**